Doctoral College: TU-D
Unravelling advanced 2D materials

DISSERTATION

On the Charge Exchange Dynamics of Highly Charged Ions in atomically thin solids

ausgefürt zum Zwecke der Erlangung des akademischen Grades
einer Doktorin der technischen Wissenschaften
unter der Leitung von

Univ. Prof. Dr. Friedrich Aumayr
E134
Institut für Angewandte Physik

eingereicht an der Technischen Universität Wien
Fakultät für Physik

von

Dipl.-Ing. Janine Schwestka

Matrikelnummer:1025552
Anschützgasse 14/25
1150 Wien

Wien, 2020

Wien, 06. April 2020

_____
Janine Schwestka

Kurzfassung

In vielen Gebieten der Physik spielt die Wechselwirkung von Ionen mit Oberflächen eine große Rolle, etwa in der Kernfusion, wo der Aufprall energetischer Ionen aus dem Fusionsplasma zur Erosion der Wandmaterialien und somit zu einer Begrenzung der Lebensdauer dieser Komponenten führt. Bei technischen Anwendungen wiederum wird der Ionenbeschuss von Oberflächen zur Materialanalyse (Elementzusammensetzung, Ionenmikroskopie), zur Oberflächenreinigung oder -beschichtung, zur Materialbearbeitung (Strukturierung, Lithographie), zur gezielten Materialmodifikation (Implantation, Veränderung der Eigenschaften) oder zur medizinischen Behandlung (Ionenstrahltherapie) eingesetzt. Um auf diesen Gebieten weitere Fortschritte zu erzielen, müssen die zugrunde liegenden Wechselwirkungsmechanismen zwischen Ionen und Festkörpern und insbesondere deren Oberflächen im Detail untersucht werden. Mit der Entdeckung und Verfügbarkeit von 2D-Materialien wie z.B. Graphen wurden erstmals Experimente möglich, bei denen eine Ion nur mit einer einzigen Atomlage eines Festkörpers wechselwirkt. Dies erlaubt es, die beim Durchtritt eines Ions ablaufenden Prozesse wie Ladungsaustausch, elektronische Anregung oder Energiedeposition in bisher beispielloser Detailliertheit zu bestimmen.

Im Rahmen dieser Arbeit wurde dazu ein Transmissionsexperiment aufgebaut, welches es ermöglicht, den Ladungseinfang (und damit die Deposition potentieller Energie), die Emission von Elektronen (und Röntgenphotonen), den kinetischen Energieverlust und den Streuwinkel von hochgeladenen Ionen bei Transmission durch verschiedene 2D-Materialien experimentell zu bestimmen. Durch Verwendung verschiedener 2D Materialien (leitfähiges Graphen, halbleitendes Molybdändisulfid) ist ein vertiefter Einblick in die Abhängigkeit von der elektronischen Struktur des untersuchten Materials möglich. Die beobachtete ultraschnelle Abregung des bei der Annäherung an eine 2D-Oberfläche entstehenden hohlen Atoms (HA) ist durch einen Interatomaren Coulomb Zerfall (ICD), einem Zwei-Zentren Auger-Prozess, beschreibbar. In dieser Arbeit wird gezeigt, dass diese Erklärung auch auf 2D-Materialien mit anderen elektronischen Eigenschaften, wie z.B. das halbleitende Molybdändisulfid (MoS_2), ausgedehnt werden kann. Der Vergleich zwischen Monolagen Graphen (SLG) und Monolagen MoS_2 zeigt, dass die beobachtete Neutralisationsdynamik tendenziell unabhängig von der elektronischen Bandstruktur des Materials ist. Die primäre Deposition der potentiellen Energie eines hochgeladenen Ions über ICD führt zu einer elektronischen Anregung der Oberfläche. Beim Halbmetall Graphen kommt es dabei zur Emission einer großen Anzahl von niederenergetischen Elektronen. Im Gegensatz dazu ist die Anzahl der emittierten Elektronen beim 2D-Halbleiter MoS_2 eher gering. Dieses un-

terschiedliche Verhalten hängt mit den elektronischen Eigenschaften des Materials zusammen. Während im Graphen aufgrund der hohen Ladungsträgerbeweglichkeit Elektronen schnell ins Wechselwirkungsgebiet nachgeliefert werden können, bleibt die halbleitende MoS_2 Membran auf einer längeren Zeitskala positiv geladen und hindert die Elektronen daran, die Oberfläche zu verlassen.

Dies erklärt auch, warum es – wie kürzlich erst gezeigt - für freistehendes MoS_2 zur Bildung von Nanometer großen Poren an der Einschlagstelle des hochgeladenen Ions kommen kann, während an SLG keine Porenbildung beobachtbar ist. Aufgrund dieser Erkenntnisse werden in dieser Arbeit sogenannte Van-der-Waals-Heterostrukturen bestehend aus einer Monolage MoS_2 auf SLG mit hochgeladenen Ionen beschossen. Transmissions-elektronenmikroskopische (TEM) Aufnahmen zeigen, dass sich nur dann Poren bilden, wenn die MoS_2-Schicht dem Ionenstrahl zugewandt ist, während im anderen Fall sowohl die obere Graphenschicht als auch die darunter liegende MoS_2-Schicht intakt bleiben. Die Freisetzung der potentiellen Energie findet also im Wesentlichen bereits in der ersten Lage eines Festkörpers statt. Ein weiterer experimenteller Hinweis für diese Annahme findet sich im Vergleich von Mono-, Bi- und Tri-Lagen Graphen. Die experimentell bestimmte Elektronenausbeute ändert sich nicht signifikant mit der Anzahl der Lagen und ist daher ein weiteres Indiz dafür, dass der überwiegende Anteil der potentiellen Energie eines hochgeladenen Ions bereits in der ersten Lage eines Festkörpers deponiert wird.

Abstract

In many fields of physics, the interaction of ions with surfaces plays a major role, for example in nuclear fusion, where the impact of energetic ions from the fusion plasma leads to erosion of wall materials and thus to a limitation of the lifetime of these plasma facing components. In technical applications, in turn, ion bombardment of surfaces is used for material analysis (element composition, ion microscopy), for surface cleaning or coating, for material processing (structuring, lithography), for targeted material modification (implantation, changing properties) or for medical treatment (ion beam therapy). In order to achieve further progress in these fields, the underlying interaction mechanisms between ions and solids and especially their surfaces must be investigated in detail. With the discovery and availability of 2D materials such as graphene, experiments in which an ion interacts with only a single atomic layer of a solid became accessible for the first time. This makes it possible to determine the processes that take place when an ion passes a single atomic layer of a solid, such as charge exchange, electronic excitation or energy deposition with unprecedented detail.

Within the framework of this thesis, a transmission experiment has been constructed and built for this purpose, which makes it possible to determine experimentally the charge capture (and thus the deposition of potential energy), the emission of electrons (and X-ray photons), the kinetic energy loss and the scattering angle of highly charged ions (HCIs) during transmission through various 2D materials. By using different 2D materials (conductive single layer graphene (SLG), semiconducting molybdenum disulfide (MoS_2)) a deeper insight into the dependence on the electronic structure of the investigated material is possible. The observed ultrafast de-excitation of the hollow atom (HA) formed when approaching a 2D surface can be described by an Interatomic Coulombic Decay (ICD), a two-center Auger process. In this thesis it is shown that this explanation can be extended to 2D materials with other electronic properties, such as semiconducting MoS_2. The comparison between monolayer graphene and monolayer MoS_2 shows that the observed neutralization dynamics tends to be independent of the electronic band structure of the material. The primary deposition of the potential energy of a HCI via ICD leads to an electronic excitation of the surface. In the case of the semi-metal graphene, this results in the emission of a large number of low-energy electrons. In contrast, the number of emitted electrons is rather low in the 2D semiconductor MoS_2. This different behavior is related to the electronic properties of the material. While in graphene electrons can be quickly replenished to the interaction region due to the high charge carrier mobility, the semiconducting

MoS$_2$ membrane remains positively charged on a longer time scale and prevents the electrons from leaving the surface.

This also explains why - as recently shown - nanometer-sized pores can form at the impact site of the HCI for freestanding MoS$_2$, whereas no pore formation can be observed for SLG. Based on these findings, in this work so-called van-der-Waals heterostructures consisting of a monolayer MoS$_2$ on SLG are bombarded with HCIs. The transmission electron microscopy (TEM) image shows that pores are only formed when the MoS$_2$ layer faces the ion beam, while in the other case both the upper graphene layer and the MoS$_2$ layer underneath stay intact. The release of the potential energy therefore essentially takes place already in the first layer of a solid. A further experimental indication for this assumption can be found in the comparison of mono-, bi- and trilayer graphene. The experimentally determined electron yield does not change significantly with the number of layers which again supports the assumption that the majority of the potential energy of a HCI is already deposited in the first layer of a solid.

List of Publications

Parts of this thesis have already been published, are accepted for publication or are in preparation for publication. A list is given in the following.

Publications in Scientific Journals as first author

- **J. Schwestka**, A. Niggas, S. Creutzburg, R. Kozubek, R. Heller, M. Schleberger, R. A. Wilhelm, F. Aumayr
"Charge-exchange-driven low-energy electron splash induced by heavy ion impact on condensed matter"; Journal of Physical Chemistry Letters, **10** (2019), 4805 - 4811, doi:`10.1021/acs.jpclett.9b01774`

- **J. Schwestka**, D. Melinc, R. Heller, A. Niggas, L. Leonhartsberger, H. Winter, S. Facsko, F. Aumayr, R. A. Wilhelm
"A versatile ion beam spectrometer for studies of ion interaction with 2D materials"; Review of Scientific Instruments, **58** (2018), 0851011 - 0851018, doi: `10.1063/1.5037798`

- **J. Schwestka**, R. A. Wilhelm, E. Gruber, R. Heller, R. Kozubek, M. Schleberger, S. Facsko, F. Aumayr
"The role of radiative de-excitation in the neutralization process of highly charged ions interacting with a single layer of graphene"; Nuclear Instruments & Methods in Physics Research Section B, **422** (2018), 63 - 67, doi: `10.1016/j.nimb.2018.02.022`

Publications in Scientific Journals as co-author

- S. Creutzburg, **J. Schwestka**, A. Niggas, H. Inani, M.K. Tripathi, A. George, R. Heller, R. Kozubek, L. Madauß, S. Facsko, J. Kotakoski, M. Schleberger, A. Turchanin, P. L. Grande, F. Aumayr, R. A. Wilhelm
"Vanishing influence of the band gap on charge exchange of slow highly charged ions in freestanding single layer MoS_2"; Physical Review Letters, **submitted** (2020)

- R.A. Wilhelm, E. Gruber, **J. Schwestka**, R. Heller, S. Fascko, F. Aumayr
  "Neutralization dynamics of slow highly charged ions in 2D materials"; Applied Sciences, **8** (2018), 1050101 - 1050116, doi:`10.3390/app8071050`

- R.A. Wilhelm, E. Gruber, **J. Schwestka**, R. Kozubek, T. Madeira, J. Marques, J. Kobus, A. Krasheninnikov, M. Schleberger, F. Aumayr
  "Interatomic Coulombic Decay - the mechanism for rapid de-excitation of hollow atoms"; Physical Review Letters, **119** (2017), 103401, 1-6, doi:`10.1103/PhysRevLett.119.103401`

Conference and workshop contributions as first author

Invited talks

- **J. Schwestka**
  "Electronic response of 2D materials to high localized electric fields"; 3rd TU-D Retreat, Langenlois, Austria (19.09.2019).

- **J. Schwestka**
  "2D-materials irradiated with slow highly charged ions"; 1st Symposium on Electron, Photon and Ion Collisions on Molecular & Atomic Nanostructures (**1.EPIC-MAN**), Caen, France, (22.07.2019).

- **J. Schwestka**
  "Ion beam spectroscopy of 2D materials"; 2nd TU-D Retreat, Langenlois, Austria (26.09.2018).

- **J. Schwestka**
  "The interaction of highly charged ions with 2D materials"; 19th International Conference Physics of Highly Charged Ions (**HCI-2018**), Portugal, Lissbon (05.09.2018)

- **J. Schwestka**
  "Relaxation pathways of slow highly charged ions transmitted through 2D materials"; 10th International Symposium on Swift Heavy Ions in Matter & 28th International Conference on Atomic Collisions in Solids (**SHIM-ICACS 2018**), Caen, France (02.07.2018)

- **J. Schwestka**
  "Interaction of slow highly charged ions with single layer graphene"; 1st TU-D Retreat, Langenlois, Austria (26.09.2017)

- **J. Schwestka**
  "Interaction of slow highly charged ions with single layer graphene"; 23rd International Conference on Ion-Surface Interactions (**ISI-2017**), Moscow, Russia (24.08.2017)

Short oral presentations

- **J. Schwestka**
"Perforation of 2D heterostructures"; Symposium on Surface Science 2020 (**3S*20**), St. Christoph am Arlberg, Austria (03.03.2020)

- **J. Schwestka**
"Low-Energy Electron Splash from Graphene Driven by Charge Exchange of Highly Charged Ions"; 23rd Workshop on Inelastic Ion-Surface Collisions (**IISC-2019**), Matsue, Japan, (18.11.2019)

Poster Presentations

- **J. Schwestka**, A. Niggas, S. Creutzburg, R. Wilhelm, F. Aumayr
"Highly charged ion impact on graphene leading to the emission of low energy electrons"; 31st International Conference on Photonic, Electronic and Atomic Collisions (**XXXI IC-PEAC**), Deauville, France (25.07.2019)

- **J. Schwestka**, A. Niggas, R. Wilhelm, F. Aumayr et al.
"Ion-induced electron emission from 2D materials"; 10th Workshop "Towards Reality in Nanoscale Materials" (**TRNM X**), Levi, Finland (13.02.2019)

- **J. Schwestka**, R. Wilhelm, S. Creutzburg, R. Heller, R. Kouzubek, M. Schleberger, S. Facsko, F. Aumayr
"Interaction of highly charged ions with 2D materials"; Symposium on Surface Science 2018 (**3S*18**), St. Christoph am Arlberg, Austria (28.02.2018)

- **J. Schwestka**, R. Wilhelm, E. Gruber, R. Heller, R. Kozubek, M. Schleberger, S. Facsko, F. Aumayr
"Radiative vs. non-radiative de-excitation of initially slow highly charged ions transmitted through a freestanding single layer of graphene"; 22nd International Workshop on Inelastic Ion-Surface Collisions (**IISC-2017**), Dresden, Germany (20.09.2017)

- **J. Schwestka**, R. Wilhelm, D. Melinc, L. Leonhartsberger, F. Aumayr
"Experimental setup for studying collisions of highly charged ions with graphene and other 2D materials"; 18th International Conference on the Physics of Highly Charged Ions (**HCI-2016**), Kielce, Poland (15.09.2016)

- **J. Schwestka**, R. Wilhelm, E. Gruber, R. Kouzubek, A. Hierzenberger, R. Heller, M. Schleberger, S. Facsko, F. Aumayr
"Slow highly charged ion transmission through graphene - x-ray emission"; 27th International Conference Atomic Collisions in Solids (**ICACS 2016**), Lanzhou, China (25.07.2016)

- **J. Schwestka**, A. Fuchs-Fuchs, L. Rachbauer, F. Aumayr
  "Electron emission from single layer graphene induced by impact of highly charged ions";
  Symposium on Surface Science 2016 (**3S*16**), St. Christoph am Arlberg, Austria (24.02.2016)

Invited seminar talks

- **J. Schwestka**
  "Slow highly charged ions for probing two-dimensional materials"; Seminarvortrag within
  the Atomphysik-Seminar, GSI-Darmstadt, Germany (16.01.2019)

- **J. Schwestka**
  "Interaction of slow highly charged ions with 2D materials; seminartalk"; Seminarvortrag
  Universität Bielefeld, Bielefeld, Germany (08.06.2018)

Supervised Students

David Melinc
Master thesis: Experimental Setup NIELS for Energy Loss Measurement of Slow Highly Charged Ions based on Time-of-Flight (2017)

Lukas Leonhartsberger
Master thesis: Aufbau und Inbetriebnahme einer Koinzidenzmessapperatur für Ionen-induzierte Elektronenemission und Ionenspektroskopie mittels Flugzeitmessung (2017)

Maximilian Lengauer
Project thesis: Darstellung von Messdaten eines Streuexperiments mittels eines MATLAB-Programms (2017)

Anna Niggas
Bachelor thesis: Setup for measuring ion induced electron emission from single layer graphene (2017)
Project thesis: Transmission of medium energy ions through single layer graphene. A time of flight approach to measure electron energies. (2018)
Master thesis: The role of contaminations in the interaction of highly charged ions with 2D materials (2019)

Benjamin Wöckinger
Bachelor thesis: "Scattering of Highly Charged Ions on Single-, Double- and Triple layer Graphene" (2019)

Bernd Stechauner
Project thesis: "Detection of slow electrons emitted due to slow highly chraged ion impact on graphene" (2019)

Contents

1

Introduction

The present work was performed at the Institute of Applied Physics at TU Wien under the supervision of Prof. Friedrich Aumayr. Within a close collaboration, parts of the experiments were performed at the Ion Beam Center at the Helmholtz-Zentrum Dresden-Rossendorf (HZDR). Several bachelor, project and master students at the TU Wien contributed to the presented results as well as complementary studies were and are still performed within the PhD thesis of S. Creutzburg at the HZDR under the supervision of R.A. Wilhelm. In the framework of the doctoral college "TU-D Unravelling advanced 2D materials" funded by the TU Wien, results were discussed in several seminars and retreats on an interdisciplinary level.

1.1   The Bottleneck Problem

Studies on basic ion-solid interaction mechanism became a main field of research within the past decades since many technological applications rely on the underlying physical processes. Using ions for targeted surface modification or tailoring of electronic properties is indispensable in nowadays semiconductor industry, nano-lithography or various ion analytic methods such as e.g. Rutherford backscattering or secondary ion mass spectrometry along with many others. To implement the usage of ions into modern technologies, a significant number of studies on

fundamental basics in ion-solid interactions were performed in the past [1–3]. The ion's energy deposition and its further dissipation in the system manifests the key element for most technological applications. It depends on nuclear collisions with target atoms, the nuclear stopping of the ion, as well as energy transfer into the electronic system, hence its electronic stopping. As an initially charged particle reaches its equilibrium charge state already within the first few layers of a material, commonly a charge state independent stopping is assumed. However, for surface sensitive applications especially the energy deposition within the first few atomic layers becomes crucial. Ions in high charge states carry high amounts of potential energy initially stored in their production process and constitute therefore a very effective tool for addressing this pre-equilibrium regime. The consequent release of potential energy within a very shallow area around the ion's impact point gives rises to application relevant processes such as surface modification depending on the material's properties [4–8]. When slowing the ions down to below the Bohr's velocity ($v < 0.5\,v_0$, $v_0 = 2.19 \times 10^6$ m/s) the effect can even be enhanced since charge exchange with the target starts already above the surface. For unravelling the underlying concepts of charge exchange many studies on highly charged ion (HCI) interaction with solid surfaces have been performed. The resulting Auger electron [9–11] and x-ray emission [12–14] as well as number and statistics of ejected low-energy electrons [15–19] upon ion impact has been investigated in detail. Further, a very consistent model describing the above-surface charge transfer was evolved [20] concluding the formation of a neutral but highly excited atom above the surface, a so-called hollow atom (HA). Its further decay upon ion impact is discussed in [21] assuming a peel-off of other electrons and the formation of a second generation HA within the solid. Through a stepwise cascade of electrons filling inner-shells and corresponding energy release via the emission of Auger electrons and x-rays, the initially highly charged ion arrives in its equilibrium charge state within a certain penetration depth. This considerations might be reasonable as long as a thick solid target of mostly heavy atoms and medium charge states is assumed. However, the proposed neutralization and deexcitation channels therein were already in the past not in full agreement with all early studies.

Herrmann et al. [22] concluded from their transmission studies of medium charged 576 keV Ar^{q+} ions (q=8,12,16) through 31 nm thick carbon foils charge equilibrium within the first few layers. The involved fast charge exchange required for such an efficient ion neutralization could not be explained. When Hattass et al. [23] went for even thinner carbon foils and highly charged Xe and Au projectiles, they observed charge equilibrium after transmission through 10 nm but not through 5 nm thick targets. Hence, they could pinpoint the pre-equilibrium length to be something between 5-10 nm and by taking the ion velocities into account they derived a HA neutralization time of only 7 fs. In order to explain their findings they assumed multiple Auger cascades proceeding in parallel as a sequential filling of the inner-shell vacancies with typical Auger tran-

sition rates of $10^{15} - 10^{16} s^{-1}$ could not result in charge equilibrium within only femtoseconds. Additional to ion transmission studies through thin films, charge exchange was also studied via ion scattering from smooth surfaces such as highly oriented pyrolytic graphite (HOPG) under grazing incidence [24]. Even tough a possible side-feeding mechanism, in which electron from deep target levels are transferred resonantly into inner-shell vacancies of the ion, was claimed to be a matter of discussion, the authors could only explain the efficient Ar neutralization by including such a process. Further, Martin et al. [25] deliberately limited the maximum interaction time to less than 3.2 fs by bombarding a C_{60} cage with slow Xe^{30+} ions. Besides observing a minimum exit charge state of 12 due to the limited reservoir of electrons in a cluster, they also needed to assume enhanced Auger rates for explaining their results.

1.2 Motivation

The main motivation of the present work was to further address this bottleneck problem, existing since decades, through ion transmission experiments. The strategy included to keep the solid nature of the target but limit its size down to a surface-only. With the realization of the first two-dimensional material in 2004 [26] this vision became accessible since graphene in fact represents only a monolayer of carbon atoms. Further attempts to produce even suspended samples [27] made ion-transmission through a 2D layer possible. But not only for understanding the nature of HCI neutralization since then, monolayer materials itself present a highly interesting topic as it was commonly assumed before that truly 2D crystals cannot exist [28, 29].

Besides promising extraordinary properties in contrast to their 3D counterparts [30], 2D materials are nowadays considered as ideal candidates for various technologies [31–34]. Tailoring and modifying of their electronic, optical and mechanical properties is therefore today a hot-topic not only in basic research but also in development of future applications [35]. Especially their two-dimensional "thickness" and therefore a possible limited reservoir of electrons, as this was reported for a C_{60} fullerene, made it tempting to study their response to a high and very localized electric field as it is applied via slow HCI approach. It rises questions such as the possibility for nano-structuring of the membranes [36] and the time-scales for energy deposition in only one layer of a material [37]. Furthermore, the interaction time of an ion with only one atomic layer is so short, that the pre-equilibrium regime of an initially highly charged projectile and therefore the above discussed bottleneck problem can perfectly be addressed. Time scales for neutralization and equilibration times can be extracted and compared to earlier findings on 3D solids.

Therefore the present work aims to contribute to a better fundamental understanding in ion-surface interactions by applying monolayers as targets for ion transmission studies. Potential and kinetic energy deposition and consequent dissipation in only one layer as well as energy release via particle and x-ray emission will be discussed. Further the possible nano-structuring and damage creation in 2D materials having different electronic properties is investigated as those represent relevant parameters for future technological applications.

1.3   Structure of this Thesis

In the following an overview on the involved process of slow HCI interactions with solids is given, which includes the formation of a HA above the surface as well as its consequent decay upon ion impact. Various channels for energy deposition, dissipation and energy release are discussed. Charge exchange and energy loss of ions in monolayer graphene was already studied by Wilhelm [38] and Gruber [39], summarized in [40]. Using this as a starting point, the present work completes the study on semi-metallic graphene and deals with charge exchange processes in various other materials ranging from bi-and trilayer graphene, two-dimensional semiconducting MoS_2 to a van der Waals heterostructure in chapters 5 and 6. In those systems, a common HA deexcitation process, the Interatomic Coulombic Decay (ICD) is proposed, introduced in the next chapter and published in [41]. Further, the measurement apparatus and its performance, which was designed and tested within the scope of this thesis, is explained in detail in chapter 3 and large parts therein were published in [42]. Results on x-ray emission and low-energy electron emission from graphene induced by slow HCI impact were published in [43] and [44] and are discussed in chapter 4. Complementary studies on this topic is analyzed within the PhD thesis of S. Creutzburg and results therein on the charge exchange dynamics in molybdenum disulfide (MoS_2) are discussed in a recent publication [45].

2

Basics in Ion-Solid Interactions

Phenomena arising from particle impact on a surface are usually associated with energy transfer from the projectile into the target system. Depending on the kinetic energy, a projectile can travel long distances within a solid until it is completely stopped.

0.01 keV/u Xe^{q+} 0.1 keV/u Xe^{+} 1 MeV/u Xe^{+}

typ. 10nm
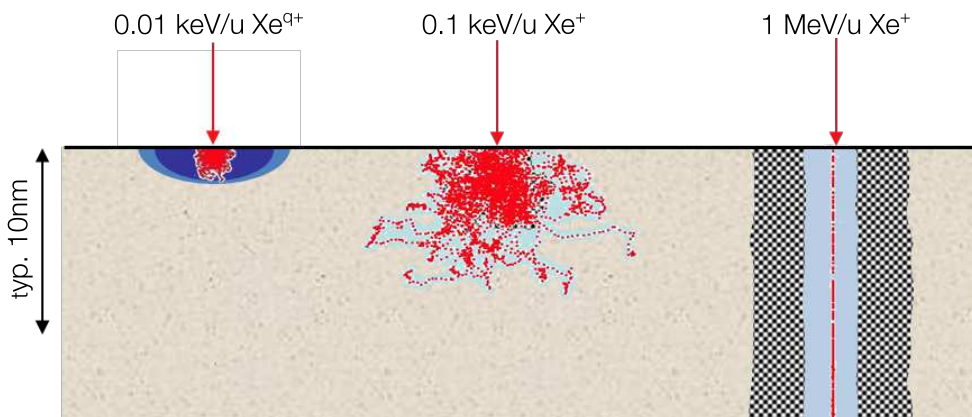
Figure 2.1: Energy deposition in a solid for very slow ions in high charge states (left), slow but singly charged ions (middle) and swift singly charged projectiles (right). Adapted from [46]

5

For swift atoms and ions, ionization and excitation of the target along its trajectory dominates, i.e. electronic stopping, which leads to high-energy electron emission enlarging the interaction area and forming an ion-track, as this is depict in the figure 2.1 for 1 MeV/u Xe ions. As an example figure 2.2b highlights the two distinct stopping regimes for Xe ions $SrTiO_3$ calculated with the computer program SRIM (Stopping and Range of Ion in Matter) [47].

Once low to moderate energies are chosen (~ 0.1 keV/u), compare figure 2.1, the stopping of the projectile is dominated by collisions with target nuclei. A prominent part of the energy is deposited close to the surface and therefore phenomena such as intermixing and sputtering of atoms from the surface occur.

As the ion's velocity is kept low but its charge state is increased an additional channel of energy deposition close to the surface can be addressed. HCIs carry high potential energy determined by the ionization energy initially spent in their production process and internally stored. Especially for high charge states, the potential energy can easily exceed their kinetic energy as this is depicted for Xe ions in figure 2.2a. Via charge-exchange, already starting above the surface, this high amount of energy can be released within a very shallow area, sketched for very slow Xe^{q+} ions in figure 2.1.

(a)

(b)
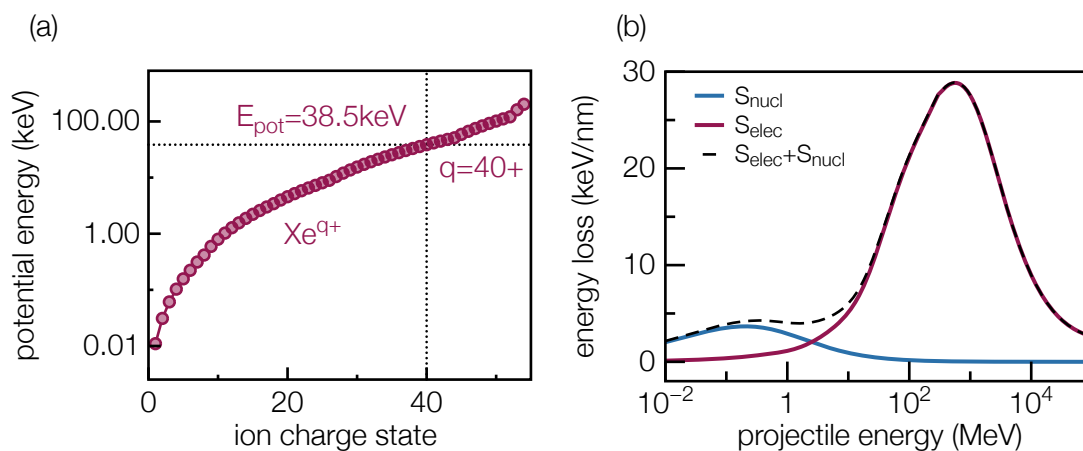
Figure 2.2: (a) Potential energy stored in a Xe ion increasing with its charge state. (b) Nuclear and electronic stopping for Xe ions in $SrTiO_3$. Adapted from [39]

2.1 Hollow Atom Formation

When a slow HCI, i.e. with ion velocity below the Bohr velocity v_0=2.19×10^{6}m/s, is approaching a solid surface in vacuum, charge exchange with the target starts already above the surface. Electrons are resonantly transferred into high-n Rydberg states and a short-lived highly excited atom, a HA, is formed [48]. The classical over-the-barrier (COB) model, first applied to HCI interaction with metallic surfaces in 1991 [20], forms the theoretical basis of above-surface neutralization for slow ions. Within the model, a critical distance for the onset of electron transfer processes is described, which depends on the work function W and the ion's charge state q (both in atomic units):

$$R_C = \frac{\sqrt{8 \cdot q + 2}}{2W}, \qquad (2.1)$$

This so formed neutral projectile with inner empty shells is rather unstable and its decay starts already during its formation is completed. However, the complexity of the involved multi-electron transfer processes makes an exact description of the different neutralization pathways rather difficult [20].

2.2 Deexcitation Channels

Commonly, a sequential decay of the HA via intra-atomic Auger emission is assumed. However, this model faces a bottleneck problem since typical Auger rates are too slow to find an agreement with experimental observation [22, 23, 25]. Therefore, either enhanced Auger rates have to be assumed or the coexistence of a number of other deexcitation channels.

Non-Radiative

Based on earlier studies on resonant and Auger electron transfer between singly charged ions and metals, Hagstrum adopted one-and two-electron transitions in order to explain HA decay via electron emission [49]. An overview is given by Arnau et al. [21] and re-pictured in figure 2.3. Within an adiabatic model assuming no correlation between electron and nuclear motion, energy levels of the approaching projectile are shifted upwards with decreasing distance to the surface. This enables resonant transitions in which electrons are transferred within ionic and target energy levels without any energy release (compare figure 2.3a). Such one-electron

transitions also include quasi-resonant neutralization (QRN) in which an electron from a deep lying energy level in the target is transported into a core state of the projectile. It only occurs for small impact parameters when the overlapping of involved inner electronic orbitals gets sufficient enough. Resonant neutralization (RN), however, becomes likely once an unoccupied state in the surface approaching projectile demotes and matches with an occupied target valence level. The inverse process, resonant ionization (RI), takes place only if the binding energy of an occupied projectile state shifts above the Fermi energy E_F unoccupied states in the conduction band of the target become available.
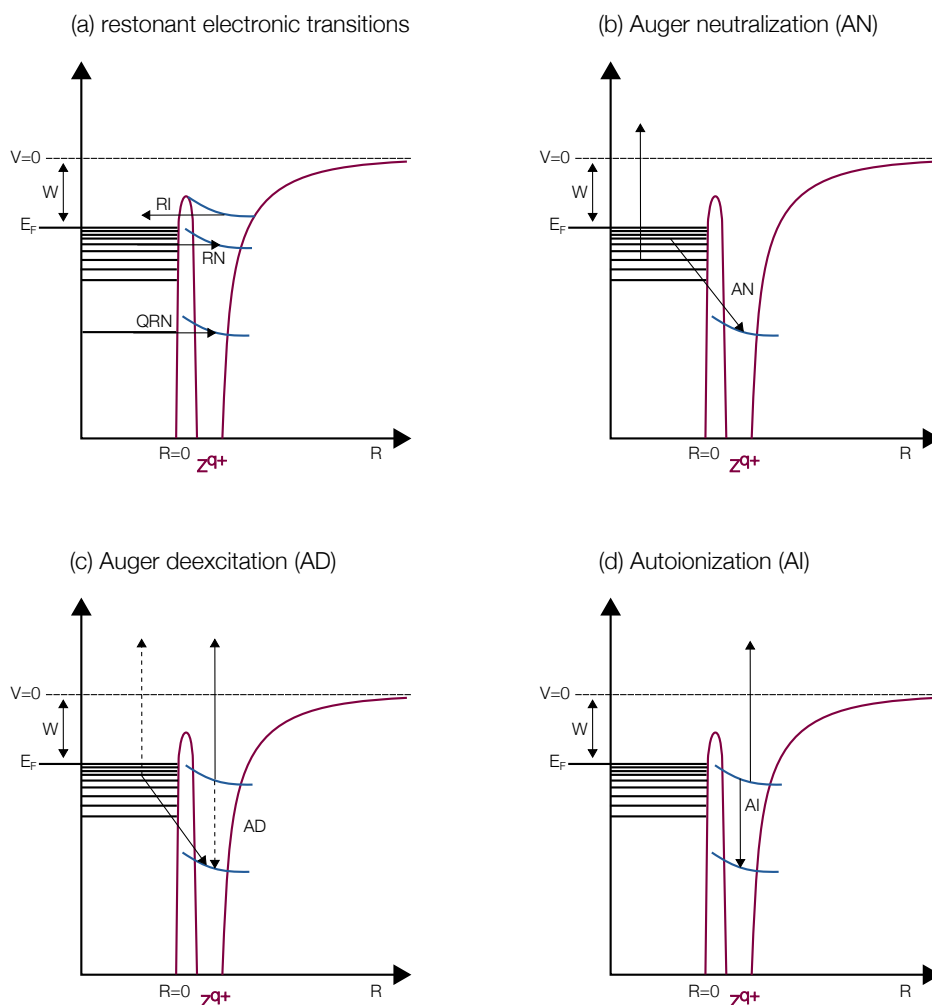
Figure 2.3: Possible electronic transitions for HA approach towards a metal surface. Resonant charge exchange (a) often acts as a precursor for electron emission into continuum via energy release channels shown in (c)-(d). Auger neutralization (AN) forms an additional charge transfer process in which two electrons are involved (b). Schematics adapted from [50].

Resonant charge transfer often acts as precursor for following electron ejection above the vacuum level. Transitions leading to such electron emission as two electrons are involved in the exchange process are depict in figure 2.3 b-d. In the case of AN a target electron is transferred into a lower projectile state while the additional energy is released via emission of another target electron. The involved neutralization energy E_N has to be at least twice the surface work function and the electron is ejected with an energy:

$$E_e \leq E_N - 2 \times W. \tag{2.2}$$

Auger deexcitation (AD) describes a process in which an electron in an excited projectile state having the energy E_{ex} interacts with a surface electrons and is emitted with an energy

$$E_e = E_{ex} - W \tag{2.3}$$

while the target electron is captured into a lower projectile state. This process is almost projectile-surface distance independent since involved initial and final charge states are very similar and therefore also the energy level shift [21]. Further, electrons from exited projectile states can also be captured into lower states releasing the energy via the emission of a target electron into vacuum.

All those processes involve ion-surface interaction. However, a possible decay channel in which only the projectile is involved is via autoionization (AI) of the ion. In this case an electron from an excited state in the projectile is demoted into a lower state resulting in the emission of a second electron occupying another excited state within the projectile.

Radiative

Due to comparable small radiative transition rates in the order of $10^8 - 10^9 \text{s}^{-1}$ in contrast to typical Auger rates, photon emission is a rather unlikely decay process. However, for highly charged projectiles transition rates increase with the forth power of charge and this deexcitation channel may become competitive. Especially for the filling of inner-shell vacancies the involved rates reach values of $10^{14} - 10^{15} \text{s}^{-1}$ [21, 51, 52]. Figure 2.4 sketches the deexcitation of an excited projectile state followed via x-ray emission.
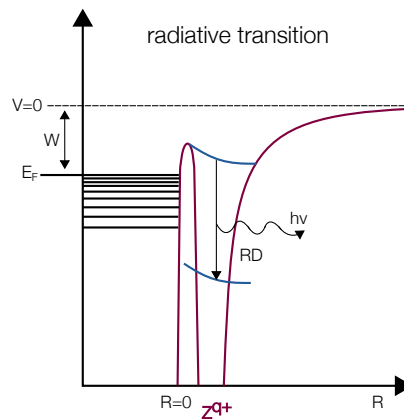
Figure 2.4: Electron transition filling an inner-shell vacancy resulting in the emission of a x-ray photon. Schematic adapted from [50].

Interatomic Coulombic Decay (ICD)

However, the model of a sequential decay via Auger transitions and competitive radiative filling of inner-shell vacancies in the projectile, still faces a bottleneck problem for some projectile-target systems. Experiments showed [23, 25, 40], that projectile neutralization and following HA deexcitation proceeds so fast, that it can only be explained if multiple electron transfer processes take place at the same time. The peeling-off of outer electrons and the formation of a second generation HA was concluded. However, in 2017 a refined model was presented which explained the rapid deexcitation of a HA in front of graphene surface via ICD. In general, ICD is a deexcitaion channel in which a core vacancy is filled by an electron from the valence band leading to the ejection of an electron from a neighboring atom into the continuum [53]. This process, also termed as two-center Auger deexcitation and related to the process shown in figure 2.3(c), is schematically depict in figure 2.5.

Originally ICD was proposed in 1997 by Cederbaum et al. [54] for weakly bound systems. The first experimental proofs were reported only a few years later by different groups using Neon clusters and dimers [55–57]. Since then more than 200 publications have shown that ICD is prominent also in other systems such as solutions and water clusters [58, 59] and particularly important in the atomic environment of many neighboring atoms. The energy transfer within the two center system is described via the exchange of a virtual photon [60, 61]. In an embedded environment, not only the exchange between two species have to be taken into account, also
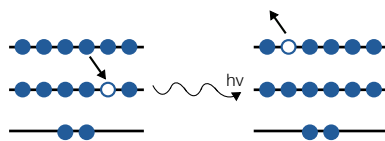
Figure 2.5: Filling of a vacancy in one atom with energy transfer via a virtual photon to a neighboring atom. The neighbor gets ionized via electron emission, a process termed as ICD (direct contribution).

nearest and next-nearest neighbor atoms can in principle contribute to the ICD process. With a distance dependence of $1/R^6$, as shown in figure 2.6, it was found that ICD is particularly important for small impact parameters and ICD rates can become quiet strong [62]. In collisions of slow HCIs with graphene, as such experiments were performed within the scope of this thesis, very small impact parameters have to be considered. For a HCI with kinetic energies in the keV range and electrons occupying high-n Rydberg states (n>20), the distance of closest approach (0.2-1.4Å) when transmitting through graphene is much smaller than equilibrium distances in van der Waals systems ($\gtrsim$ 3Å). Therefore ICD line widths reported in a various number of experimental and theoretical work were extrapolated towards small impact parameters to mimic interatomic distances present in HCI interaction with graphene. The extrapolation reveals strong ICD rates which are able to explain the deexcitation of HCI within a few femtoseconds [63].

The scenario of ICD occurring for HCI transmission through target systems like graphene, is depict in figure 2.7. With electrons in highly excited states and a distance of only a few Angstrom from the surface, the extension of the electron's wave functions in a HA can get large enough to overlap with graphene electron orbitals and therefore triggers ICD. With a carbon-to-carbon atom distance of 1.4 Å not only one carbon atom contributes to the process but also its nearest and next-nearest neighbors. Within this model, the rapid charge exchange found for highly charged xenon ions and freestanding single layer graphene (SLG) can be explained [40, 41]. Electrons in Rydberg states are quenched into empty inner-shells while the energy is transferred via virtual photons and released through electron emission from weakly bound graphene electrons.

However, so far it is not clear whether the ICD process directly populates the ground states or just low lying excited states. Therefore, in the very last steps inner-shell vacancies might still be filled via the above described Auger and radiative transitions.
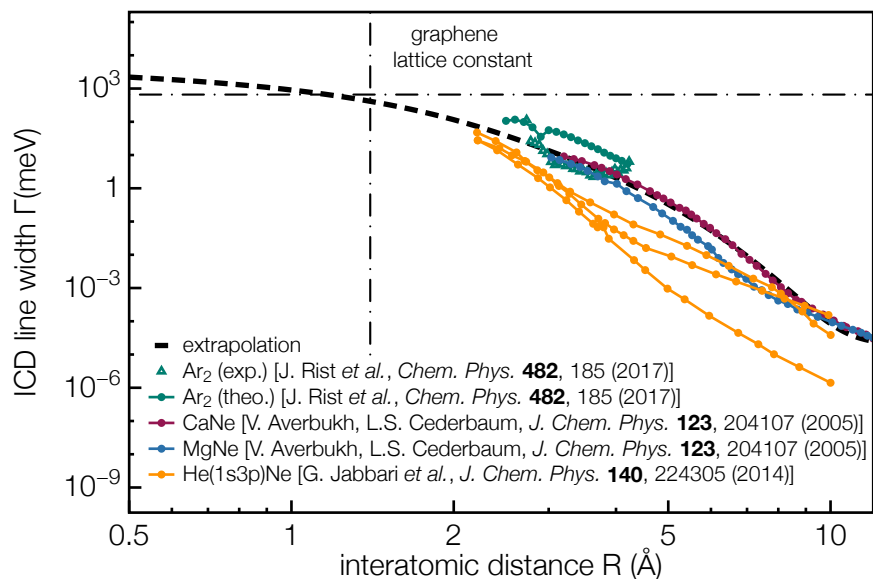
Figure 2.6: ICD rate vs. interatomic distance derived from various experiments [64–66]. All data were fitted with a universal fit and extrapolated towards small distances (dashed line) as these are possible impact parameters for HA transmission through a graphene layer. Adapted from [63].
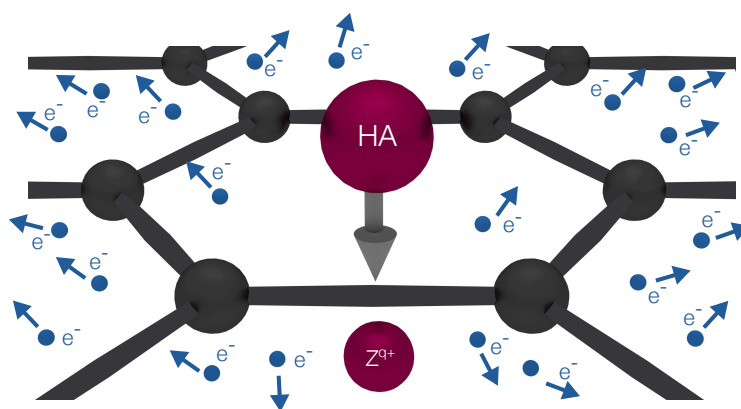
Figure 2.7: Schematics for HA decay via ICD involving many carbon atoms in graphene. Deexcitation proceeds through the emission of a large number of low-energy electrons.

2.3 Energy Release

There are various ways of energy dissipation and energy release in a solid once large amounts of (mainly potential) energy are introduced via HCl neutralization and the consequent penetra-

tion of a slow ion into the solid (mainly nuclear stopping). While the transfer of kinetic energy mainly results in sputtering of surface atoms and electrons [67, 68], the very localized release of potential energy can lead to permanent surface modifications such as hillock formation and melting [4], potential-sputtering [69] as well as to the emission of large amounts of electrons [17]. Considering the time evolution of the involved processes kinetic electron emission (KE) as well as potential electron emission (PE) sets in immediatley upon ion impact (and even above the surface) in contrast to mechanism like nano-structuring and pore formation which require a certain time for energy dissipation.

2.3.1 Potential Electron Emission

As described above deexcitation energy is released via the emission of electrons as a consequence of AN, AD, AI and ICD. This is termed as ion-induced PE. PE not only arises at the surface impact but already when the projectile is still above the surface and continues inside of the target. The dependence of the electron yield on the projectile velocity in the case of PE was empirically derived as [18, 19]:

$$\gamma_{PE}(v)\bigg|_{\vartheta=\text{cons.}} = \gamma_{\infty} + \frac{c_v}{\sqrt{v}},\tag{2.4}$$

with system dependent fitting parameters γ_{∞} and c_v. In former times the velocity-independent contribution γ_{∞} was attributed to a "peel-off effect" [21] meaning that due to the dominant screening of the HA by target electrons close to the surface electrons in outer shells are stripped off and a HA of second generation is formed. However, within the refined model which includes deexcitation via ICD, γ_{∞} can very well be interpreted as ICD, since ICD is also dependent on the investigated target-projectile combination. The second term in equation 2.4 including the fitting parameter c_v, reveals an increasing PE yield towards lower ion velocities. This trend reflects the increasing interaction time for slower ions leaving more time above the surface for AI processes [21].

Various experiments could show that at least for conducting targets in fact only the perpendicular velocity component

$$v_\perp = v \cdot \cos(\vartheta) \tag{2.5}$$

with ϑ as the angle of incidence with respect to the surface normal, determines the PE yield [70, 71]. The angle dependent potential electron emission therefore follows the relation

$$\gamma_{PE}(v, \vartheta) = \gamma_\infty + \frac{c_v}{\sqrt{v \cdot \cos(\vartheta)}}. \tag{2.6}$$

2.3.2   Kinetic Electron Emission

When measuring the total electron emission yield, in addition to PE the ion's kinetic energy deposition in the target system and the resulting emission of electrons due to momentum transfer in ion-electron collisions has to be considered. In contrast to PE this is a process which exclusively happens below the surface and is therefore comparably small when a 2D material is used as a target. In addition, multiplication cascades of electrons as present in a 3D solid are unfeasible in a 2D material.

Since during KE the projectile transfers parts of its kinetic energy into the electronic system of the target, KE can be approximated to be proportional to the electronic stopping power

$$S_e \propto \left.\frac{dE}{dx}\right|_e \tag{2.7}$$

i.e. to the loss of energy E per unit path length x. Target excitation results in electron transport towards the surface. Via scattering on other target electrons, depending on the mean free path in the material, additional (secondary low-energy) electrons are created. Especially in a solid, in which electrons from deeper layers can contribute, the initial excitation energy is dissipated within a multitude of target electrons. When reaching the surface they have to overcome the

surface barrier to be ejected into vacuum. Therefore a certain minimum energy introduced into the system is required for KE. This results in an ion velocity threshold v_{th} for kinetically emitted electrons depending on the work function W of the target, the Fermi velocity v_F and energy E_F [72]:

$$v_{th} = \frac{v_F}{2} \left(\sqrt{1 + \frac{W}{E_F}} - 1 \right) \tag{2.8}$$

The approximation is in good agreement with experimental data found in [72–75]. Typical threshold values are in the order of $v_{th} \approx 10^5$ m/s. Above the critical velocity the KE yield increases linearly with ion velocity until it reaches a saturation [15, 74].

For assuming a straight projectile path in the target and a continuous electron excitation along this path, the KE yield dependency on the impact angle ϑ follows an inverse cosine law [50]:

$$\gamma_{KE}(\vartheta) = \gamma(0°) \cdot \cos(\vartheta)^{-1} . \tag{2.9}$$

for which $\gamma(0°)$ presents the total electron emission yield at normal incidence with respect to the surface. While this approximation can be made for proton bombardment at a few keV, deviations for heavy particle impact were reported and the observed results could be fitted by the empirical expression:

$$\gamma_{KE}(\vartheta) = \gamma(0°) \cdot \cos(\vartheta)^{-\beta} , \tag{2.10}$$

where β is a fitting parameter related to the impact energy, the collision system and the angle of incidence itself. The parameter varies between $0.5 \leq \beta \leq 1.5$ [50] and approaches for high energies $\beta \to 1$.

The measured total yield γ_{total} for slow or moderate HCIs electron emission usually consists of both contributions, PE as well as KE, which are in general hard to separate from each other. As an example γ_{total} following from clean polycrystalline gold bombardment with Ne^{q+} ion is shown in figure 2.8 [74]. At low velocities PE dominates as the ion spends more time in front of the surface. Once a threshold in the ion's velocity, marked as the dashed line, is reached, KE starts to set in and increases linearly. The total electron emission yield can therefore be fitted as a sum of both contributions:

$$\gamma_{total} = \gamma_{PE} + \gamma_{KE} = \gamma_\infty + \frac{c_v}{\sqrt{v}} + k \cdot (v - v_{th}) \cdot \Theta(v - v_{th}) \tag{2.11}$$

with k as a collision system dependent parameter and Θ as the Heaviside step function [21].
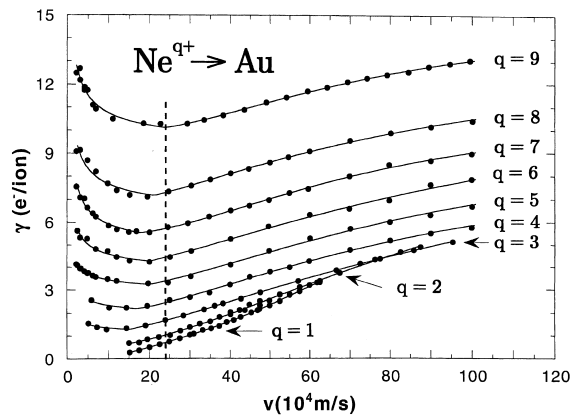
Figure 2.8: Total electron emission yield for Ne^{q+} impact on clean polycrystalline gold [74]. The dashed line symbolizes the velocity threshold for KE onset.

2.3.3 Pore Formation

Considering the low ion fluences typically applied in irradiation experiments of thin membranes with keV HCIs, direct knock-on damage induces typically single vacancies but do not lead to the formation of a nanometer-sized pore. Single atoms removed in such a way from graphene, for example, they recombine with carbon adatoms within picoseconds due to the so-called "self-healing" ability of graphene [76] since missing carbon atoms are always present in surrounding

hydrocarbon contaminations. However, such holes can be drilled when applying sufficient flu-ences as this is usually done with singly charged focused ion beams [77].

Applying HCIs as tools for the creation of such pores is possible as long as the characteristics of the specific target material is taken into account. Although the neutralization concept de-scribed above is applicable for insulating and semi-conducting targets as well [78], especially the further energy dissipation within the material strongly depends on its electronic and thermal properties.

Thus, different target response to the strongly localized electric field of a HCI is to be expected as a second step after HA deexcitation. Local charge-ups are the consequence of high charge removal and the lacking electron mobility in band-gap materials but especially in insulators. As a result Coulomb repulsion of positively charged target atoms can lead to the rupture of the material around the ion impact point, a process termed as "Coulomb explosion" [79]. Further, destabilization of atomic bonds can also follow from high density electronic excitations due to the promotion of electrons from bonding valence band states into anti-bonding states in the conduction band [80]. HCI-induced pore formation in 1 nm thick carbon nanomembranes (CNMs) was recently concluded to result from the just discussed processes [7].

3

A Versatile Ion-Beam Spectrometer

Large parts of this thesis were focused on the setup of a coincidence ion beam spectrometer allowing multiple particle recording with different detection systems and further linking registered events with each other by sorting the recorded data into listmode files. Therefore, in the following chapter the implementation of such a versatile measuring apparatus named "Neutrals and Ion Energy Loss Spectrometer (NIELS)" as well as its performance and additional upgrades are described. A detailed review has been published in [42] and large parts of the following chapter are excerpt from this publication.

3.1   Electron Beam Ion Source EBIS-A

In collaboration with the Ion Beam Center at the HZDR parts of the measurements where performed in Germany using an Electron Beam Ion Trap (EBIT) for producing ions in high charge states. However, the ion-beam spectrometer located at the TU Wien in Austria and described in the following, is equipped with an Electron Beam Ion Source (EBIS). Since the working principle of those two ion sources are very comparable, only the EBIS will be explained in more detail. To be more precise, a room-temperature Dresden EBIS-A developed by the Dreebit GmBH Dresden and the Technische Universität Dresden [81, 82] enables the production of highly charged

ions of nearly every element along the periodic table. A cathode for electron beam emission of high intensity is placed inside the source chamber which stepwise ionizes the working gas inserted into the vacuum vessel. An arrangement of three drift tubes biased at different electric potentials confines the created ions in axial direction while the negative space charge of the electron beam keeps them trapped in radial direction. Magnets are used for compressing the electron beam in the ionization volume. Figure 3.1 shows the arrangement of cathode, drift tubes and the ion beam extraction system. With optimized settings, Ne-like Xenon, which was the main working gas within this studies, can easily be extracted. The base pressure in the chamber is kept at 10^{-10} mbar and ion beam currents of > 100 fA and up to several 10 pA can be reached. The source can be operated in 'leaky mode', meaning only ions with sufficient thermal energy can overcome the potential barrier

$$E > q \times (U_b - U_a) \tag{3.1}$$

with U_a as the potential applied to the middle drift tube and U_b to the third drift tube. Further, ion beam pulses with a length of 50 ns of up to 100 µs can also be extracted within the 'pulsed mode'. Since the source chamber is biased at U_0 (typical 4.5-12 kV) ions leaving the chamber have an initial energy of

$$E_{kin} = q \times U_a. \tag{3.2}$$

A Wien filter with an aperture of 1 mm is used for selecting a specific charge state by mass-to-charge separation.

Further, the required initial ion beam energy can be adjusted by an electrostatic deceleration lens system. Therefore a negative potential U_{decel} is applied to the source chamber including all power supplies galvanically isolated from ground through an isolating transformator. As a result - in principle – ions with arbitrarily low kinetic energy can be extracted. In praxis, a reasonable beam diameter at the sample of ~2 mm is only possible down to a few 10 eV×q ($E_{kin} = q \times (U_a - U_{decel})$). Reducing the initial kinetic energy leads to a radial spread of the resulting beam. For further focusing a multi-segment system of electrostatic lenses was designed and simulated (using the SIMION code [83]) for this setup. With 7 individually biased segments a stepwise deceleration is realized leading to a reasonably good beam focus at a working distance of 460 mm. Two lens segments are split in horizontal and vertical direction enabling beam steering to correct for beam misalignment [42].
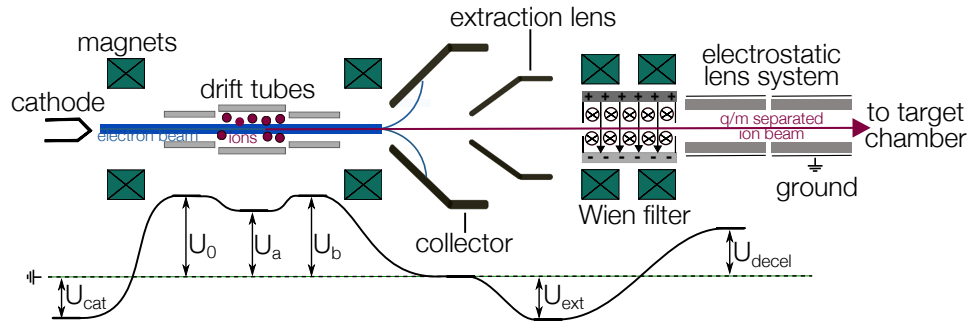
Figure 3.1: Schematics of an EBIS extraction system. HCIs created by electron impact ionization are trapped in an arrangement of drift tubes. Electrostatic potentials applied to each component are shown with respect to ground potential. The extracted beam is mass-to-charge separated in a Wien filter and further steered and focused with an electrostatic lens system. Figure taken and modified from [42].

3.2 Ion Beam Alignment and Beam Chopper

To measure the time of flight (TOF) of the ions after target transmission, a pulsed ion beam is required. In priciple, the pulsed mode of the EBIS-A would deliver such beam pulses but the power supplies (used for U_b) do not provide fast enough (<10 ns) voltage ramping. Therefore, the ion beam is guided through an electrostatic beam chopper and an arrangement of horizontal and vertical slit apertures (selectable 0.5x10 mm or 1x10 mm each) when leaving the extraction zone. Adjustable beam spot diameters of either $0.25\,mm^2$ or $1\,mm^2$ can be chosen with a beam divergence of 0.04° or 0.09°, respectively [42].

Figure 3.2 shows the working principle of the beam chopping with a spacing between the plates of d=2 mm, a width of the deflection plates of w=6 mm (perpendicular to the ion beam direction), and a plate length (in direction of the ion beam) of s=2 mm, mounted in a distance of l=100 mm in front of the first slit aperture. Applying voltage to the chopper plates $U_{chopper}$ lifts the passing ion beam above the opening of the following slit aperture (Δy) according to equation 3.3, preventing the ions to reach the target. The required chopping voltage $U_{chopper}$ and the width of those pulses depend on the ion's mass m and charge state q as well as on the kinetic energy, i.e. the ion's velocity v.

$$\Delta y = \frac{U_{chopper} \cdot q}{d \cdot m} \frac{s}{v^2}\left(\frac{s}{2} + l\right) \tag{3.3}$$
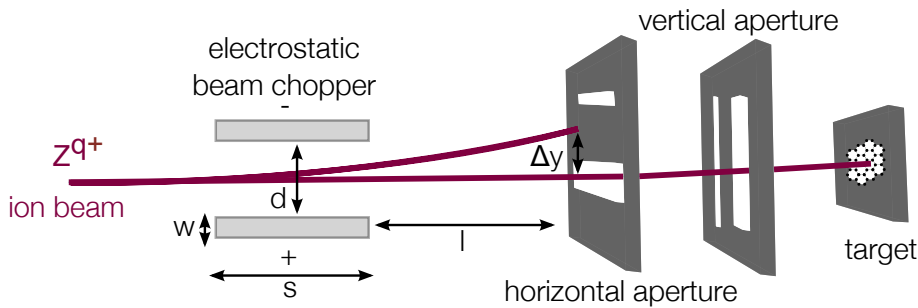
Figure 3.2: Arrangement of an electrostatic beam chopper and apertures for generating ion pulses. Beam alignment can be accomplished by choosing between a 0.5x10 mm or 1x10 mm horizontal as well as vertical aperture. Once the beam has passed the chopper, ions hit the aperture (chopping voltage on) or pass another (vertical) aperture and reach the target (chopping voltage off).

The electrostatic beam chopper was designed and mounted by David Melinc and therefore more details on the beam chopping process and technical drawings can be found in his master thesis [84]. For chopping a keV to a few 100 keV ion beam, a fast pulsing electronics enables to switch on and off voltages of ±60 V applied to both deflection plates for 8-34 ns within a rise/fall time of 3-5 ns [85]. The electronics is triggered by a standard TTL pulse with a maximum frequency of 2 MHz. Figure 3.3a shows an oscillograph of the voltages (±13 V) applied to both chopping plates for a typical setting of 34 ns opening time. Even tough the maximum opening time was chosen, the chopper is effectively opened for only 9 ns [42]. The opening time as well as the chopping voltage needs to be adjusted to the ion velocity since slower ions need more time to pass the chopper. With this method ion pulse widths in the range of 4-10 ns can be achieved as it is depicted in figure 3.3b. Nevertheless, the time the ions need to pass the chopper can exceed the adjustable opening time of 8-34 ns depending on their kinetic energy, limiting the lowest possible kinetic energy for TOF measurements with the described beam chopper setup to about 30 keV for Xe ions. A further limitation of this TOF measurement technique is the high loss in ion beam intensities, since the majority of extracted ions do not reach the target for a required 10 ns opening time of the chopper and an ion beam frequency of 5 MHz [84]. Especially when working with high charge states and two-dimensional materials with low coverage this limitation becomes unbearable.
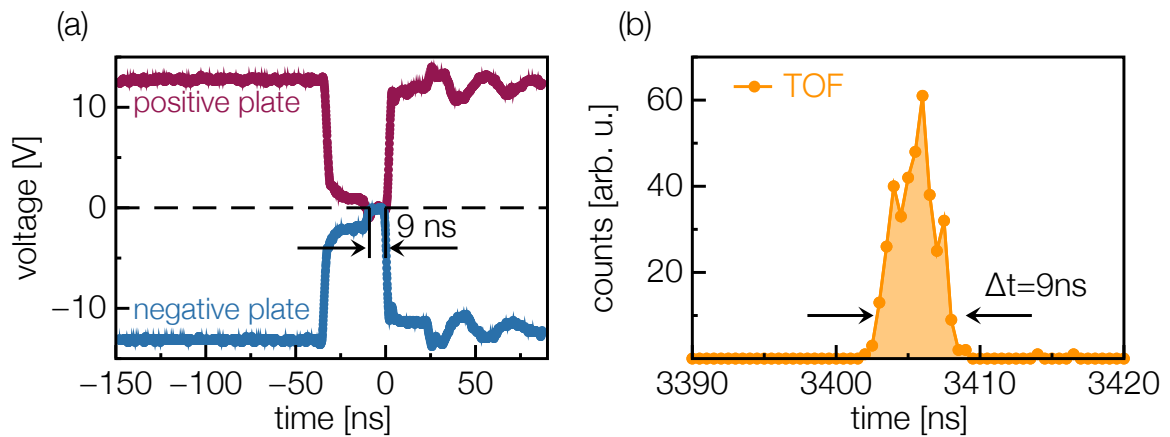
Figure 3.3: (a) Voltage applied to electrostatic beam chopper. Even though the chopper opening time was set to the maximum (34 ns), a completely switching off (0 V) was only reached for a duration of 9 ns. (b) Measured TOF for 131 keV Xe^{30+} ions with an effective chopper opening time of 9 ns. Figures adapted from [42].

3.3 Target Mounting

Once a specific ion charge state q with a certain kinetic energy E_{kin} is chosen, the aligned beam is focussed onto the target in the middle of the experimental chamber, also kept under ultra high vacuum (UHV) conditions ($<5 \times 10^{-9}$ mbar). The target holder is movable along all axes (x-,y- and z-axis) and enables sample mounting of up to three individual targets (with an outer diameter of 3 mm) at the same time. After their growing process all 2D materials are transfered onto a perforated 10-12 nm thick carbon support foil (Quantifoil [86]) placed on top of a copper or gold transmission electron microscopy (TEM) grid. The TEM grids with a diameter of 3 mm and typical mesh sizes of 300 bridges/inch can be placed into one of the target holder slots (see figure 3.4). Quantifoils (QFs) with typical hole sizes of 1.2-2μm with a spacing of 1-4μm are used. To ensure ion transmission only through the freestanding 2D material but not its QF support, QF supports covered with an additional 50-100 nm thick Au layer were used in several measurements. The sample holder can be rotated by an angle φ of up to 60° (self-shadowing for larger angles) with respect to the incoming ion beam. Via a load lock system target transfer can be accomplished within 30 min. The load lock chamber is equipped with a separate pre-vacuum as well as turbo pump and is usually kept at a pressure of $<1 \times 10^{-6}$ mbar.
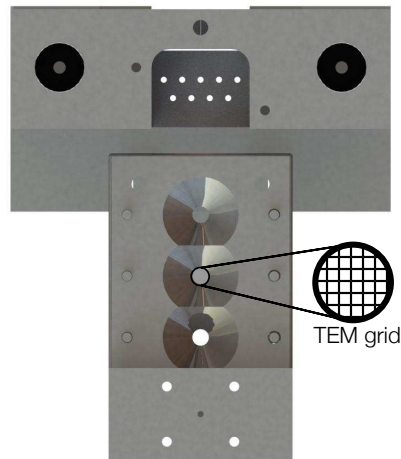
Figure 3.4: Targetholder for ion transmission experiments enables mounting of up to three individual samples placed on a TEM grid.

3.4 Electron Detection

The impact or even the ion's close approach towards the surface of the target (in case of HCIs) promptly leads to the emission of electrons which are recorded and counted by means of electron emission statistics [16–18, 87]. Along with the passivated implanted planar silicon (PIPS) detector for electron counting figure 3.5 shows the required main components for this measurement method. Further, the sketch depicts a silicon drift detector enabling x-ray detection following from the ion's interaction with the sample. Currently, such a detector is not installed at the ion-beam spectrometer but is considered for future upgrades of the setup and was used for measurements at the HZDR [43].

3.4.1 Passivated Implanted Planar Silicon Detector

For electron detection a PIPS detector is used. A bias voltage of +60 V is applied in reverse direction in order to create a charge depleted regime (active area) in the semiconducting layer (silicon chip). Penetrating charged particles are stopped within this region and create electron-hole pairs. The energy required for an electron-hole pair formation depends on the layer material but is independent of the incoming particle's energy. Thus, the number of created electron-hole
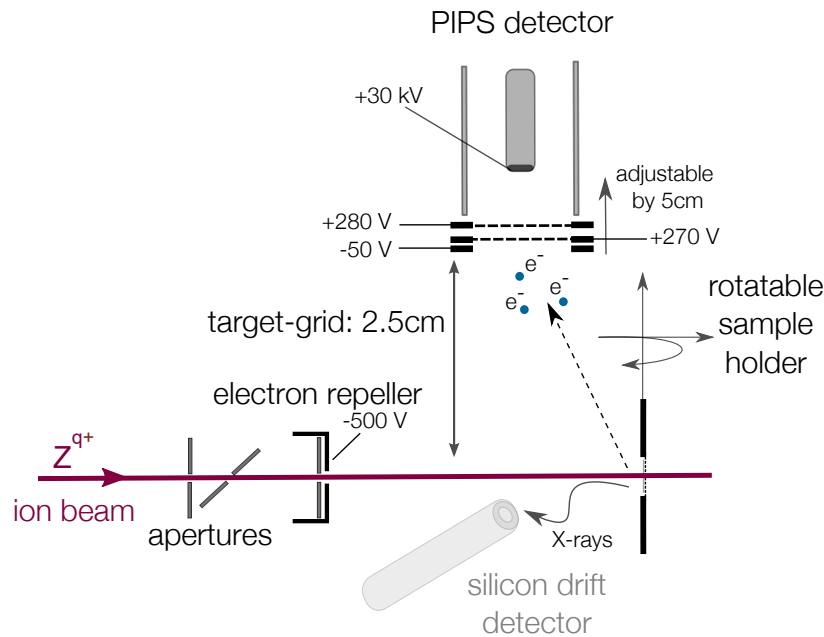
Figure 3.5: Electrons are extracted via a positive field applied to a highly transparent grid. A second grid optimizes the collection efficiency before the electrons reach the PIPS detector. A negative biased frame and an electron repeller assist to focus the electrons onto the active area of the detector.

pairs is directly proportional to the energy of the impinging particle [87]. The applied bias voltage triggers electrons to move to one side while holes migrate to the other and as a result a charge pulse is formed. The following charge senstive preamplifier integrates over the charge and the extracted pulse height corresponds to the deposited energy in the active area. Figure 3.6 shows the partially depleted PIPS detector used in the current setup with an active area of $100\,mm^2$, a resolution of $12\,keV$ (FWHM) for α particles and an active area thickness of $100\,\mu m$ provided by Canberra (model: PD100-13-100AM). The PIPS detector is biased at high voltage (up to $30\,kV$) to accelerate electrons towards the active area.

3.4.2 Electron Extraction Units

In order to extract emitted electrons from the target an arrangement of two highly transparent grids, a frame and an electron repeller is used (see figure 3.5). First hand, a second grid (bi-
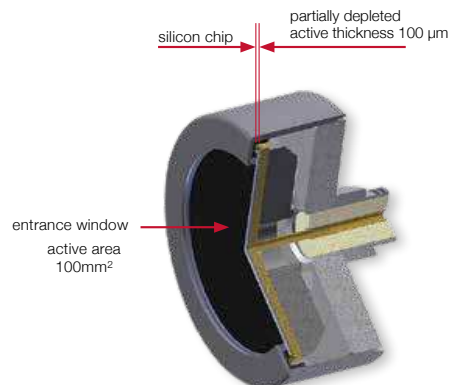
Figure 3.6: Sectional view of a PIPS detector [88]. Silicon is used for the semiconducting layer of the active area.

ased slightly less positive than the first one) was installed to avoid secondary electrons following from electron impact on the first grid to reach the detector. Since within the first measurements this procedure turned out to be not necessary (no change in the measured electron emission yield) the additional grid was used to further optimize the electron collection efficiency and is therefore biased slightly more positive than the first grid (compare figure 3.5) when measuring electron number statistics. The outer diameter of both grids is 91.2 mm, consisting of a highly transparent copper mesh with a diameter of 60 mm and a mesh size of 0.63/0.2 mm and a non-transparent supporting frame of 31.2 mm. An additional frame, a circular aperture without any mesh having the same dimensions as the support frame of the collection grids, is biased at negative potential. This shields the positive biased grid frames and enables electron transmission through the grids rather than impinging on their (biased at same positive potential) support frame. Since ion beam alignment is accomplished through an arrangement of slit apertures (compare figure 3.2) electron emission also follows from ion impact on those apertures. Therefore an electron repeller biased at negative potential is used to suppress detection of such electrons through the PIPS detector. As an additional feature, the electron repeller assists to steer electrons emitted from the target in backwards direction towards the collection grids. Besides the determination of electron number statistics the setup further allows to analyze the energy distribution of emitted electrons. Therefore the collection grids are used as a pair of retarding grids via varying the potential difference between them. More precisely, the first grid is grounded while the - in this case - negative voltage applied to the second grid is varied starting from 0 V, i.e. all electrons can pass the grid and reach the PIPS, and ramped down to -20 V, i.e. until no more signal is measured at the detector. The vacuum vessel of the target chamber is not equipped with µ-metal shielding. Therefore, trajectories of low-energy electrons (<5 eV) can be influenced by external magnetic fields, e.g. the earth magnetic field, and a drop in the

collection efficiency for those electrons has to be assumed. Hence, measurement uncertainties towards lower electron energies are increased.
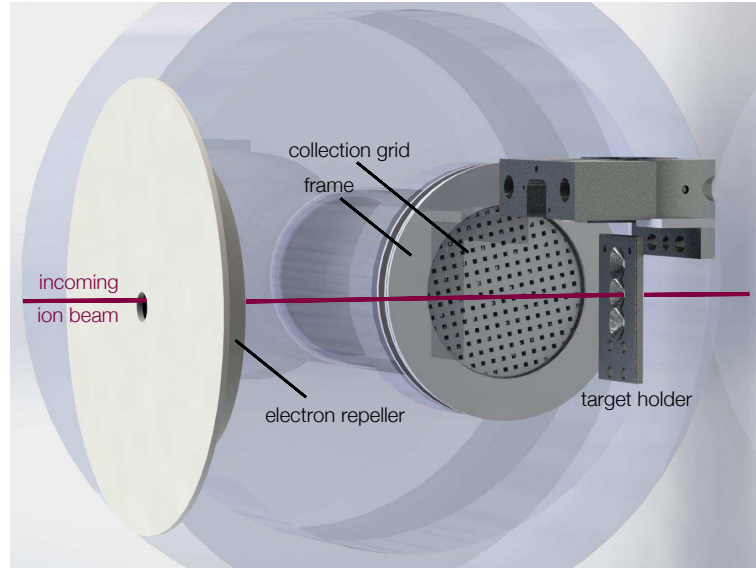

Figure 3.7: Simplified target chamber used for particle trajectory simulations. PIPS detector and a second collection grid are also present in the CAD drawing but not clearly visible in this image.

3.4.3 Electron Trajectory Simulations

In order to achieve the optimal collection efficiency requirements, particle trajectory simulations have been performed by Anna Niggas with Simion [83] and IBSIMU [89] within the scope of her master thesis [90]. Therefore the simplified CAD drawing of the target chamber shown in figure 3.7 was imported with a mesh size of 1.4 mm and a variety of potentials to the electron repeller, the frame and the pair of extraction grids was applied in order to simulate electron as well as ion trajectories for the applied voltages. In this way the efficiency of focusing electrons onto the active area of the PIPS detector can be improved and for the majority of performed measurements the voltages presented in figure 3.5 were used (U_{grid1} = +270 V, U_{grid2} = +280 V, U_{frame} = −50 V and $U_{repeller}$ = −500 V). Further, when assuming a cylindrical beam profile and a beam diameter of 2 mm the deflection of the ion beam towards the center due to the applied voltages can be reproduced as this is shown in figure 3.8a. The simulations with IBSIMU also reveal a corresponding drop in the electron emission yield probably caused by decreasing electron collection efficiency due to the deflection of the beam towards lower ion energies. Even

though this cannot be quantified by the simulations the trend is illustrated for Xe^{40+} ions and the applied voltages mentioned above.
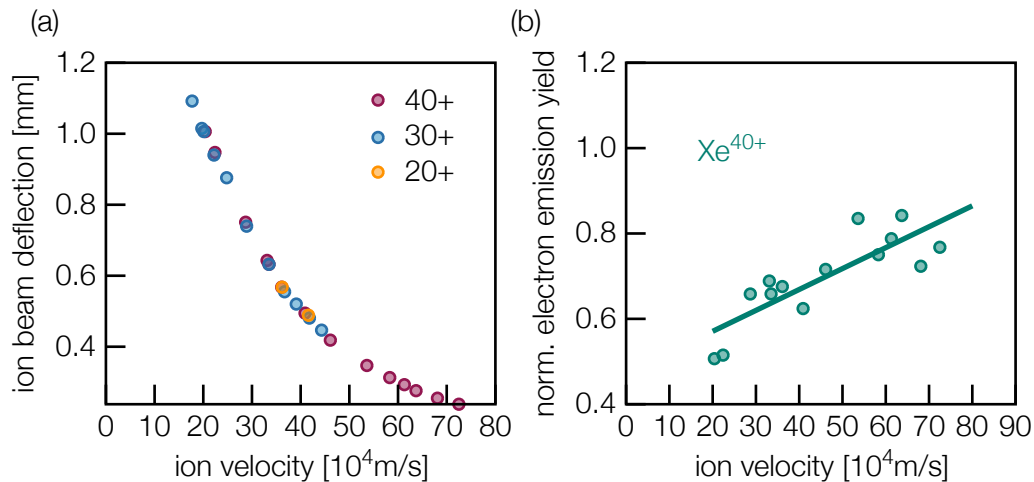
Figure 3.8: (a) Deflection of the beam for low-energy ions due to the applied voltages. (b) Corresponding drop in the electron yield caused by decreasing collection efficiency. Electron emission yield was measured for Xe^{40+} impact on SLG.

3.5 Ion Detection

After the transmission through the freestanding target membranes, the ions are registered at a position-sensitive microchannel plate (MCP) detector equipped with a delay-line anode. The MCP signal serves as a stop signal for TOF measurements of the ions while the position of their impact is used for analyzing their charge state and their scattering angle. Especially for measuring electron emission from 2D materials, recording the corresponding transmitted ion is crucial since it allows to distinguish between electrons emitted from the sample and these emitted from the support.

3.5.1 Microchannel Plate Detector

A state-of-the-art RoentDek DLD40 MCP delay-line detector ensures simultaneous recording of time (resolution <0.2 ns) and position (resolution < 0.1 mm) of impinging ions [91]. Based on electron multiplication via secondary emission the device consists of a pair of MCPs in chevron configuration with an active area of 40mm^2. For recording ions, the MCP front side is biased

at -1900 V while the back side is grounded. The anode is typically biased at +100 V. The whole detector is housed in a metal box with a highly transparent grid at the entrance to shield the target chamber from the high electrical field [42]. Position encoding is accomplished via the difference in the signal arrival time measured at the end of the parallel-pair delay-line, for each layer independently. Therefore, reference- and signal-wires are biased at +250 V and +300 V, respectively.

3.5.2 Exit Charge State Analysis
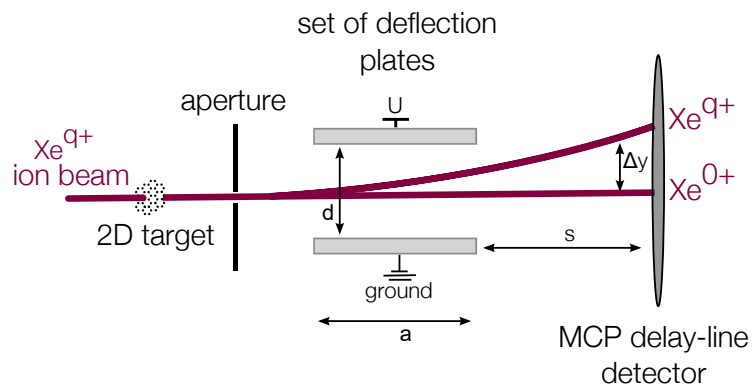
Figure 3.9: Sketch of ions transmitted through a freestanding target and charge state separated by passing a horizontal aperture and a set of deflection plates. The ion's impact position at the MCP detector in vertical direction corresponds to their charge state, while in the horizontal direction it corresponds to their scattering angle.

A set of deflection plates (length a=39.6 mm and gap between plates d=21.15 mm) in a distance of s=210 mm in front of the MCP delay-line detector (shown schematically in figure 3.9) is used for charge state separation of transmitted ions through the target. Biasing one plate negatively and grounding the other, leads to an ion deflection onto a specific position of the detector depending on the charge state. A horizontal slit aperture with an opening of 0.5x10 mm is placed (750 mm after the target) to stop ions from scattering in vertical direction [42] and performing a proper exit charge state analysis. The deflection of charged particles with respect to a neutral projectile passing the deflection plates (Δy) can be used to calculate the exit charge state q_{exit} of an ion after transmission according to the following equation:

$$\Delta y = \frac{1}{2} \frac{U \cdot q_{exit}}{E_{kin}} \frac{a}{d} \left(\frac{a}{2} + s \right), \tag{3.4}$$

with an ion beam energy of E_{kin} and a voltage U applied to the deflection plates. In order to use the whole detector, the MCP is movable in y-direction and is for typical measurements adjusted in a way that neutrals impinge at a position y=-12 mm and ions still in their initial charge state q_{in} at y=+12 mm.
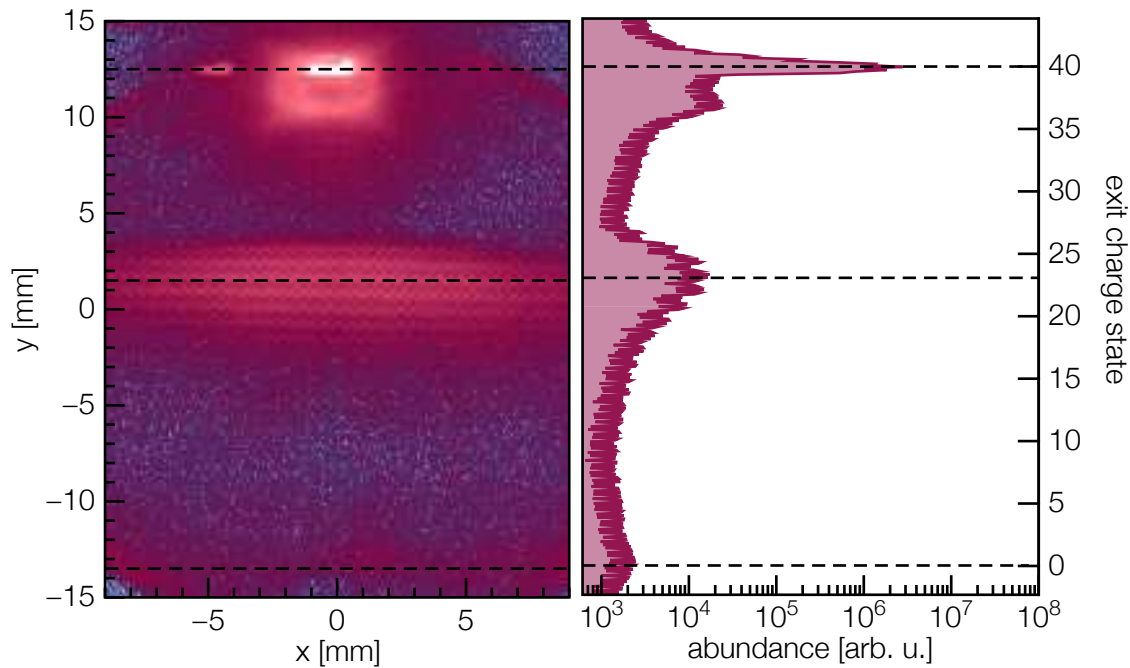
Figure 3.10: 2D image recorded with the MCP delay-line detector and further processed using RoentDek's CoboldPC software [92].

Figure 3.10 shows an example 2D image (left) recorded for 310 keV Xe^{40+} ions transmitted through a freestanding SLG and the further converting into exit charge states (right) according to equation 3.4. Data registered at the delay-line detector are processed with the CoboldPC software provided by RoentDek [92]. In this particular case, a mean exit charge state of q_{exit}=23 is found for the measured charge state distribution. Further, ions passing holes in the sample and therefore remaining in their initial charge state q_{in}=40 as well as ions in their ground state (q=0) are highlighted (dashed lines).

3.6 Electronics and Data Acquisition

When measuring ion-induced particle emission from a two-dimensional material, attempts to achieve detection from reactions at such a thin layer only but not at its support become inevitable. To realize this intention in the current setup ions and emitted particles, e.g. electrons, are detected in coincidence. In this way emission from the 2D layer and from the supporting material can be distinguished. Proof of principle measurements have already been performed in earlier works [93]. The NIELS setup allows now not only the measurement of electrons and ions in coincidence but also the correlations between emitted electrons and ions in a certain charge state after transmission. An overview of the required electronics is presented in figure 3.11.
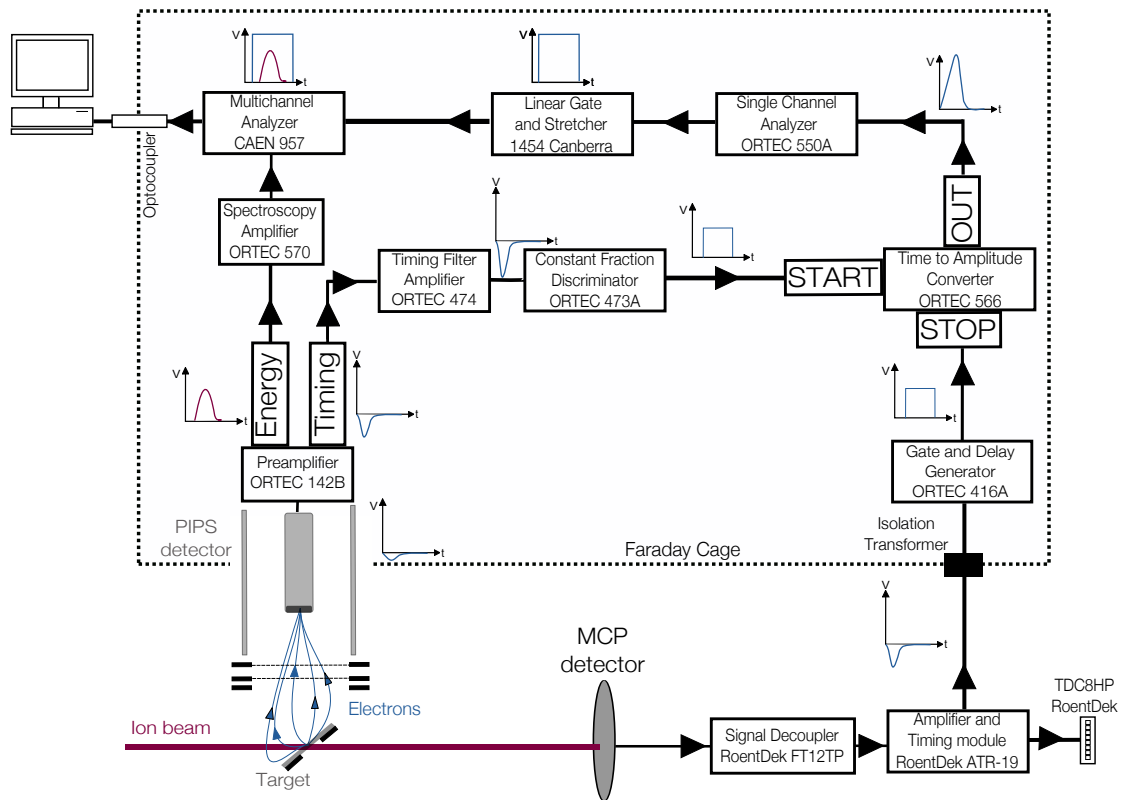
Figure 3.11: Electronics for simultaneous data processing of ion and electron signals. Adapted and modified from [94].

The main principle of assigning an electron signal to a corresponding transmitted ion is based on the simultaneously measurement of both signals, one registered at the PIPS and the other at the MCP detector but delayed by the ion's TOF. The latter is picked up by a FT12TP signal decoupler and further processed in an amplifier and timing module ATR19, both units provided

by RoentDek. Fast negative NIM pulses (channel 1-4 for x- and y-position decoding and channel 8 for MCP timing signal) are transferred into a time to digital converter (TDC) (RoentDek TDC8HP). When connecting the pulsed chopper signal (as fast negative NIM-standard signal) to channel 7 of the TDC - serving as the START trigger - the CoboldPC software can be used to visualize the ions TOF by interpreting the MCP timing signal as the corresponding STOP.

At the same time this MCP signal is transferred as a NIM-standard fast negative logic pulse via an isolation transformer into a Faraday cage, which is necessary since all further electronic components are set at the same potential (up to 30 kV) as the PIPS detector. In an ORTEC 416A gate and delay generator the signal is converted into a positive NIM-standard signal further required for processing in a time to amplitude converter (TAC). The ion signal here is connected to the STOP input.

For the START input of the TAC the signal generated by the electron's impact at the PIPS detector is required. The charge pulse is integrated via a charge sensitive ORTEC 142B preamplifier and the negative timing output (corresponding to the time of impact) is further shaped and amplified in an ORTEC 474 timing filter amplifier. A following ORTEC 473A constant fraction discriminator is used to generate a positive NIM-standard logic pulse which serves as START trigger.

The TAC generates now an output pulse with an amplitude corresponding to the time difference between START and STOP (0 to +10 V). Hence, the pulse with a height corresponding to the ion's time of flight from the moment of electron emission to the impact at the delay-line detector is transferred into a single channel analyzer (SCA). Here an upper and a lower window (between 0 to +10 V) can be adjusted according to the corresponding ion's TOF visualized via the CoboldPC software or calculated through the following equation:

$$\text{TOF} = s \cdot \sqrt{\frac{m}{2 \cdot (E_{kin} - \Delta E_{kin})}} \tag{3.5}$$

in which s represents the distance from the target to the detector, E_{kin} the ion's inital kinetic energy and ΔE_{kin} a possible energy loss within the target.

In this way only signals corresponding to this TOF pass the SCA and generate a gate in the following linear gate and stretcher module (1454 Canberra). The gate is further transferred into the "gate input" of a CAEN 957 multichannel analyzer (MCA) enabling detection of an incoming signal only if a gate is present.

As such an incoming signal, the energy output pulse of the ORTEC 142B preamplifier is used for which the height is proportional to the deposited energy in the detector, i.e. the number of simultaneously detected electrons. The pulse is further shaped and amplified in an ORTEC 570 spectroscopy amplifier before transferred into the MCA input. The gated electron pulse height distribution is recorded through the MCA and transferred via an optocoupler to the ground side for further data acquisition via a CAEN Demo software.

3.7 Upgrade I - Electron Signal as START Trigger

Within the frame of this thesis, the NIELS setup received an upgrade leading to an improvement in TOF measurements and electron data acquisition. Therefore, the START trigger generated by the ion beam chopper is replaced by the electron emission signal resulting from the ion's interaction with the target. The electron's TOF (about 7-20 ns depending on the target-grid distance) is comparable short in contrast to the flight time of slow ions (a few μs depending on the ion's kinetic energy). Further, the new upgrade abstains from using the broad energy output signal of the PIPS detector's preamplifier for which additional time consuming shaping is required. Instead, the fast negative timing output (rise time from <5 ns to 25 ns [95]) is amplified with an ORTEC 474 timing filter amplifier and directly extracted onto ground side via an arrangement of seven high voltage (HV) (<30 kV) ceramic capacitors. The timing output is an inverted version of the energy output differentiated by a transformer [95] and can therefore be used for electron number statistics when amplified accordingly. A sketch of the updated electronics can be seen in figure 3.12.

In order to prevent damage of high frequency electronics on the ground through voltage break downs from the HV side, a special protection electronics is installed which is based on a series of switching diodes easily to be replaced. It keeps the shape and the timing information of the pulse which is further processed in a fast timing amplifier (RoentDek FAMP1) designed for high frequency signals. The amplified timing pulse is transferred into a RoentDek CFD1x. The output of the CFD1x matches the timing of the electron detection, i.e. the START trigger, with a width corresponding to the height of the input pulse, i.e. the number of registered electrons. Since input pulses should not exceed -2 V, the resolution of the recorded pulse height spectrum is decreased dramatically. However, electron number statistics can be stored in a listmode file additional to the ion's timing and position information and a mean number of emitted electrons can be extracted sufficiently. Therefore electron emission can be directly assigned to a specific ion exit charge state and TOF, again visualized with the RoentDek CoboldPC software.
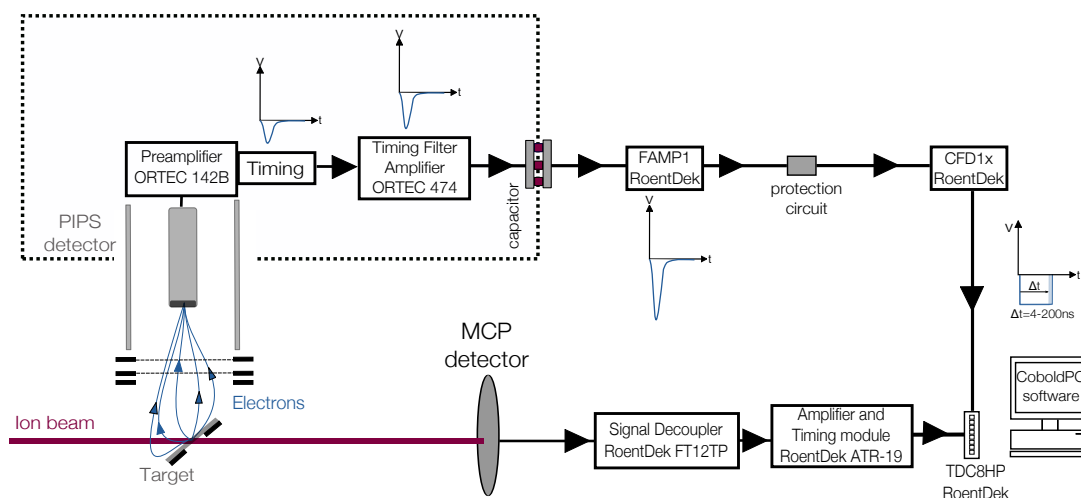
Figure 3.12: Electronics for recording ions and electrons in coincidence. The upgrade analyzes only the electron's timing signal and converts the pulse height (which is proportional to the energy output) into a pulse width via a constant fraction discriminator (CFD) while the timing information remains.

3.8 Upgrade II - Cleaning Procedure for 2D-Samples

Contaminations on the surface of a sample are a crucial issue for studies on structural and electronic properties of 2D materials, which essentially consist of surfaces only and are therefore dominated by their surface properties [96, 97]. Further, when it comes to applications the consequent drop in their performance can become dramatically [98–100]. Adsorbates such as water and hydrocarbons cover basically every surface [101]. Additionally, for 2D membranes, residuals from transfer processes to the TEM grid as well as metallic residuals (Cu,Fe,Ni) from the growing process via chemical vapour deposition (CVD) [?, 97, 101–103] supervene. Since transmission studies crucially depend on having a monolayer sample only, any form of contamination on the membrane might already influence the result. To minimize the presence of contaminations originating from the growth and transfer process, a major focus was put on receiving 2D samples for which a ploymer-free transfer process can be accomplished. The University of Duisburg-Essen provided such graphene samples, meaning that there are no polymethyl methacrylate (PMMA) residuals present on the single layer graphene placed on a QF/TEM grid [104]. The transfer of the CVD grown graphene to the supporting grid was accomplished based on the dry-cleaning process described in [97]. A scanning transmission electron microscopy (STEM) image of such a sample can be seen in figure 3.13. It shows areas of clean pristine graphene (middle) with an extension of up to hundreds of nm surrounded by ad-

sorbates at the surface (left) [40]. The thickness of these hydrocarbon adsorbates in equivalent numbers of graphene layers can be deduced from STEM and is also shown (right).
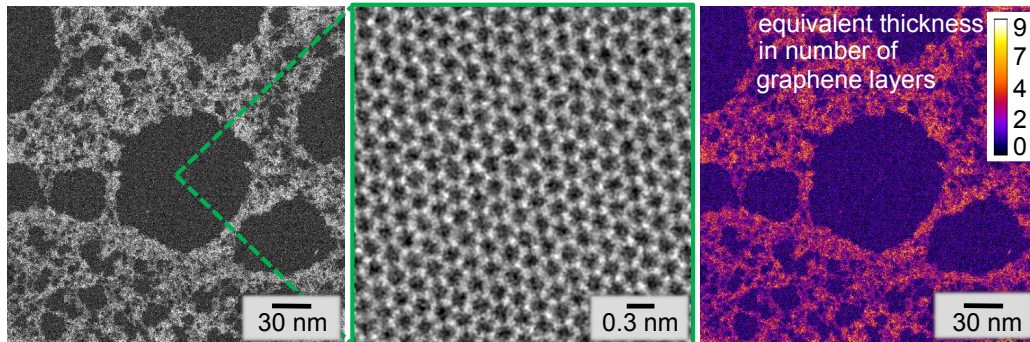
Figure 3.13: Single layer of graphene covered by contaminations. Hundreds of nm large areas of pristine graphene (middle) are surrounded by hydrocarbon adsorbates at the surface (left). The thickness can be estimated as an equivalent of number of graphene layers (right). Taken from [40].

The STEM image in 3.13 shows the absence of any PMMA residuals. However, for other 2D samples such as molybdenum disulfide, investigated in this thesis, a ploymer-free transfer process could not be applied. Hence, thick residuals remain on the sample threatening the transmission spectra to origin from ion interaction with heavily contaminationed areas. Furthermore, bubbles or dirt pockets within two layers of heterostructures or bi-and trilayer samples [30, 105] resulting from the stacking process persist. Therefore, an in-situ cleaning procedure for 2D samples was developed and applied at the NIELS setup within the master thesis of Anna Niggas [90]. The target holder was equipped with a 1Ncl15 heating wire and a PT1000 temperature element for recording the applied temperature. The wire has a room temperature resistance of $R=1\Omega$ and can be operated with $I=5\,A$ to heat the target up to 400°C. Usually the samples were annealed at maximum temperature for about 30 minutes and kept at 200°C during the measurements. At high temperatures polymer residuals remaining from production and transfer processes could be removed or clustered together to thick pockets (no ion transmission) while the measurements at 200°C ensured no further attachment of hydrocarbons at the surface. Through the annealing treatment, the 2D samples were cleaned within one day [90]. To further improve the efficiency of the cleaning procedure by minimizing the required time a 6 W 445 nm laser diode [106] was additionally installed. The laser can be controlled via a modulation voltage between 0 and 5 V and a spot size of 4x1 mm can be reached. When applying the maximum power, clean samples can be expected within one hour of laser treatment [90].

3.9 Performance

The following section will focus on the reliability of the NIELS apparatus including the above described upgrades of the experimental setup and highlight its unique features by enabling simultaneous recording of ions and secondary particles.

3.9.1 Ion Beam Divergence and Angle Acceptance

Especially for analyzing the impact parameter dependence of transmitted ions by extracting their scattering angle from the recorded 2D spectra, it is essential to know the initial spatial profile of the beam when extracted from the source. Without using any target, it can be directly measured at the delay-line detector via position imaging. The beam diameter and its angular divergence is determined on the one hand by the aperture used for the Wien filter (1 mm) and on the other hand by the potentials applied to the electrostatic lens extraction system. Since the latter are used for beam deceleration they crucially depend on the chosen ion beam energy. The extraction is far more precise when choosing higher ion beam energies (>120 keV). At a certain value, it is impossible to keep the focus of the ion beam and the beam diameter continuously spreads with decreasing ion's energy until even external magnetic fields seem to influence the trajectory of the beam (below $\simeq$ 50 eV). Additionally, the beam can be collimated by a set of vertical and horizontal slit apertures after the extraction unit (compare figure 3.2). Depending on the chosen slit diameters (0.5x10 mm or 1x10 mm), beam spot sizes of 0.25 mm^2 and 1 mm^2 with a divergence of 0.04° and 0.09° can be reached [42]. The inset in figure 3.14 shows the 2D image of a 170 keV Xe^{30+} ion beam when choosing 0.5 mm horizontal and vertical slit apertures. A Gaussian shaped line profile (red line in the inset) can be extracted from the delay-line detector (DLD) and shows a full width at half maximum (FWHM) of 1 mm. With a target-detector distance of 1105 mm and an allowed divergence of 0.04°, a beam spot size of 0.52 mm at the sample can be determined and is well in agreement with the chosen collimation slits [42]. Further, after the transmission ions can practically be scattered in all possible angles ϑ according to the following equation [107]:

$$\sin\vartheta^2 < \frac{m_2^2}{m_1^2}. \tag{3.6}$$
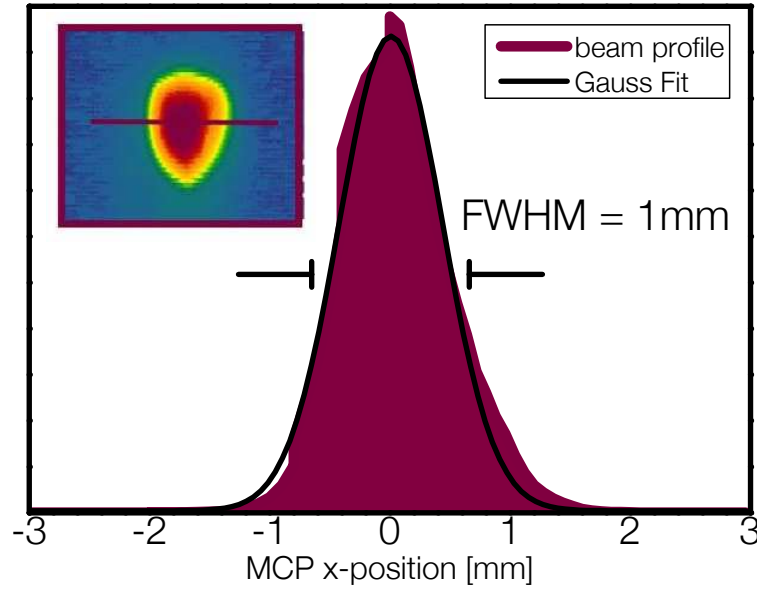
Figure 3.14: Gaussian shaped line profile of a 170 keV Xe^{30+} ion beam impacting on the DLD. The inset shows the recorded 2D image of the beam at the MCP. Taken and adapted from [42].

for $m_1 > m_2$. This is the case for Xenon ($m_1 = m_{Xe}$) scattering on Carbon ($m_2 = m_C$) since for a monolayer of graphene multiple collisions are prohibited. Hence, a maximum scattering angle follows:

$$\sin \vartheta_{max} = \frac{m_C}{m_{Xe}}$$
$$\vartheta_{max} = 5.34°$$

(3.7)

Since the set of deflection plates in front of the DLD allows to separate transmitted ions by their charge state, their angular distribution has to be limited in vertical direction in order to avoid an overlap between charge states and scattering angles. This is accomplished by using a 0.5x10 mm slit aperture at the entrance of the deflection plates. It allows a beam divergence of 0.04° in vertical direction for passing ions. The horizontal angular acceptance due to the aperture amounts ±0.25°. The whole drift chamber is rotatable within an angle of $\Delta\varphi = \pm 8°$ as it is sketched on figure 3.15. The impact position at the MCP in x-direction can be converted into a corresponding scattering angle by means of the following equation:

$$\varphi = \text{atan}\left(\frac{x[mm]}{1105[mm]}\right) \cdot \frac{180°}{\pi}$$

(3.8)
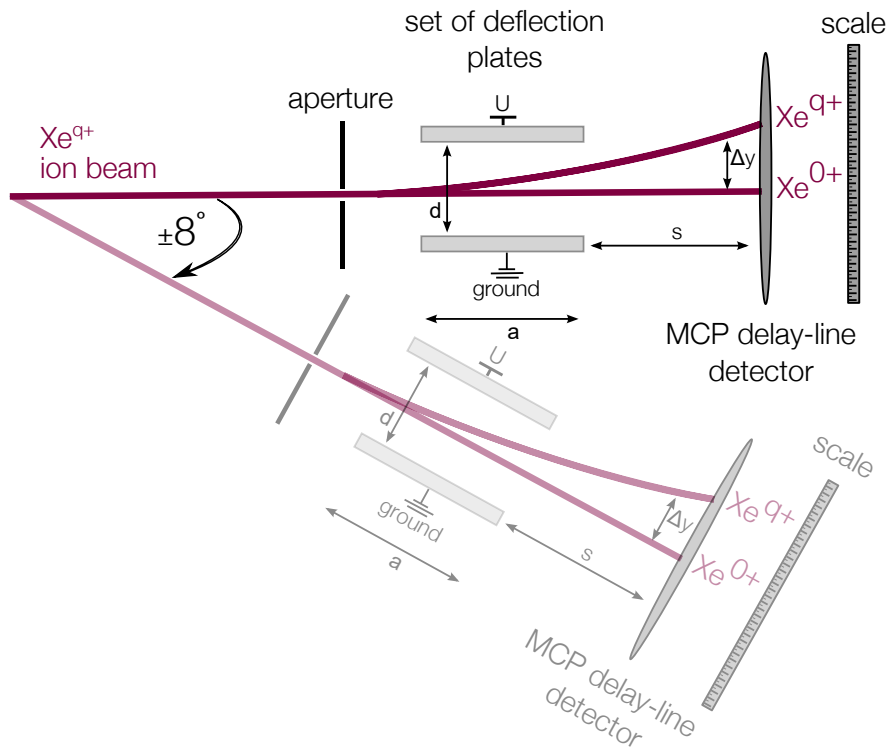
Figure 3.15: The drift chamber can be tilted by an angle of $\Delta\varphi = \pm 8°$. A scale is mounted in order to precisely adjust the rotation angle. 25 mm on the scale corresponds to a tilting angle of $\varphi = 1°$.

When the drift chamber is tilted by an angle φ, this has to be considered in the conversion. A scale (in mm) was mounted at the back of the MCP detector to adjust the recording angle. 25 mm correspond to a tilting angle of $\varphi = 1°$ [108]. With a distance of a=1381 mm from the target to the scale, a scaling factor of $\mathrm{atan}\left(\frac{25\,\mathrm{mm}}{1381\,\mathrm{mm}}\right) = 0.0181$ is introduced and included in the conversion from the DLD x-position [mm] to a scattering angle [90]:

$$\varphi = \mathrm{atan}\left(\frac{x[\mathrm{mm}]}{1105[\mathrm{mm}]} \pm 0.0181\varphi\right) \cdot \frac{180°}{\pi}. \tag{3.9}$$

As an example, figure 3.16 shows a 2D spectrum for 177 keV Xe^{40+} transmission through single layer graphene. The drift chamber was tilted within an angle range of $\Delta\varphi = \pm 5°$ and the recorded spectra have been added up accordingly. The y-axis has been calibrated in exit charge states following equation 3.4 while the x-axis is translated into scattering angles using the conversion in equation 3.9.
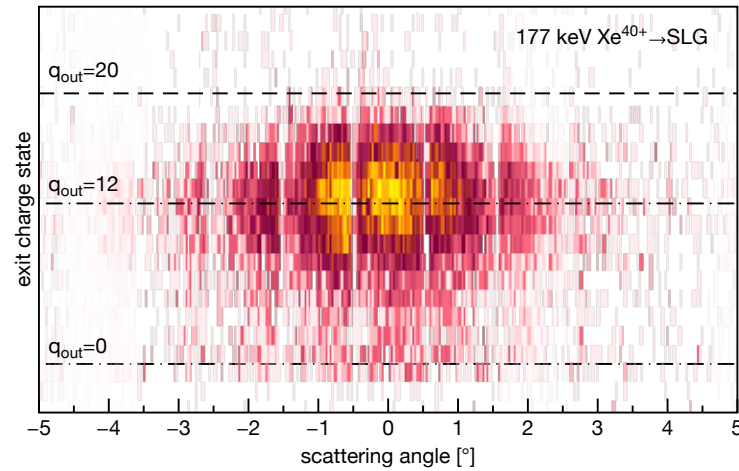
Figure 3.16: Individual recorded transmission spectra for 177 keV Xe^{40+} impact on single layer graphene by tilting the detection system by an angle of $\Delta\varphi = \pm5°$. The measured spectra are added accordingly into one 2D plot.

3.9.2 Energy Limitations

As already mentioned in the previous section extraction of HCIs with in principle every kinetic energy below 400 keV is possible using the current deceleration lens at the NIELS setup. However, underneath a certain energy threshold focusing the ion beam with the extraction system and the steering units becomes rather difficult to accomplish. Once the ions get slow enough, the beam spreads until it covers the whole MCP (diameter ~ 40 mm). Aside from that, the ions tend to deviate especially when other electric fields in the UHV chamber are applied and their trajectories are influenced by external magnetic fields. Therefore, the current setup is limited within its minimum extraction energy. Experiments requiring low and accurate beam energies such as ion implantation into 2D materials, fail due to this circumstances. Nevertheless, projects are planned in future at the NIELS setup and therefore the ion beam's energy distribution has to be precisely analyzed. In the following, two methods to evaluate the energy spread right after the extraction from the source as well as shortly before their detection at the end of the beamline will be presented and have also been discussed in [90].

Ion beam energy distribution after extraction unit

The energy distribution of the ion beam is estimated directly after the extraction from the source chamber by measuring the beam current at a plate inserted into the beam. The plate is biased

at negative voltage and by means of a retarding field, the voltage is ramped up towards positive values until the recorded signal drops and vanishes completely. The measured current can be fitted by an error function

$$f(E) = a \cdot \text{erf}(b(x - x_0) + c). \tag{3.10}$$

The derivative of the fit is used to extract the beams Gaussian shaped energy distribution. Figure 3.17 shows the results of the current measurement for Ar^{2+} with a FWHM of 28 eV.
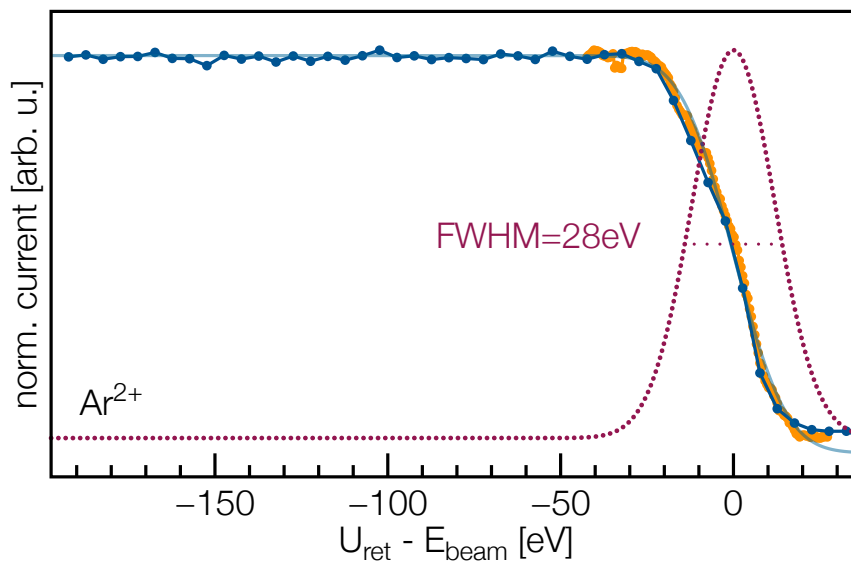
Figure 3.17: Measured Ar^{2+} current (blue line) at a plate inserted into the beam versus applied retarding field potential. The derivative of the fitted error function (yellow line) exposes an energy FWHM of 28 eV. Figure adapted from [90].

For Xe^{11+}, however, a superposition of two error functions has to be fitted to the data, presented as black lines in figure 3.18. The beam current was measured for two different extraction potentials, but still the superposition is present only shifted due to the difference in U_b. Energy distributions with FWHM of 8 eV and 11 eV as well as 7 eV and 14 eV are derived for U_b=171 V and U_b=219 V, respectively. The origin for two distinct beam energies might by due to a variation of ionization positions in the source or results from a certain geometry dependent deceleration behaviour. Further, also the Wien filter aperture determines an energy window of ±15 eV, all adding up to the final energy distribution of the beam after the extraction to be less than 15 eV.

(a)

(b)
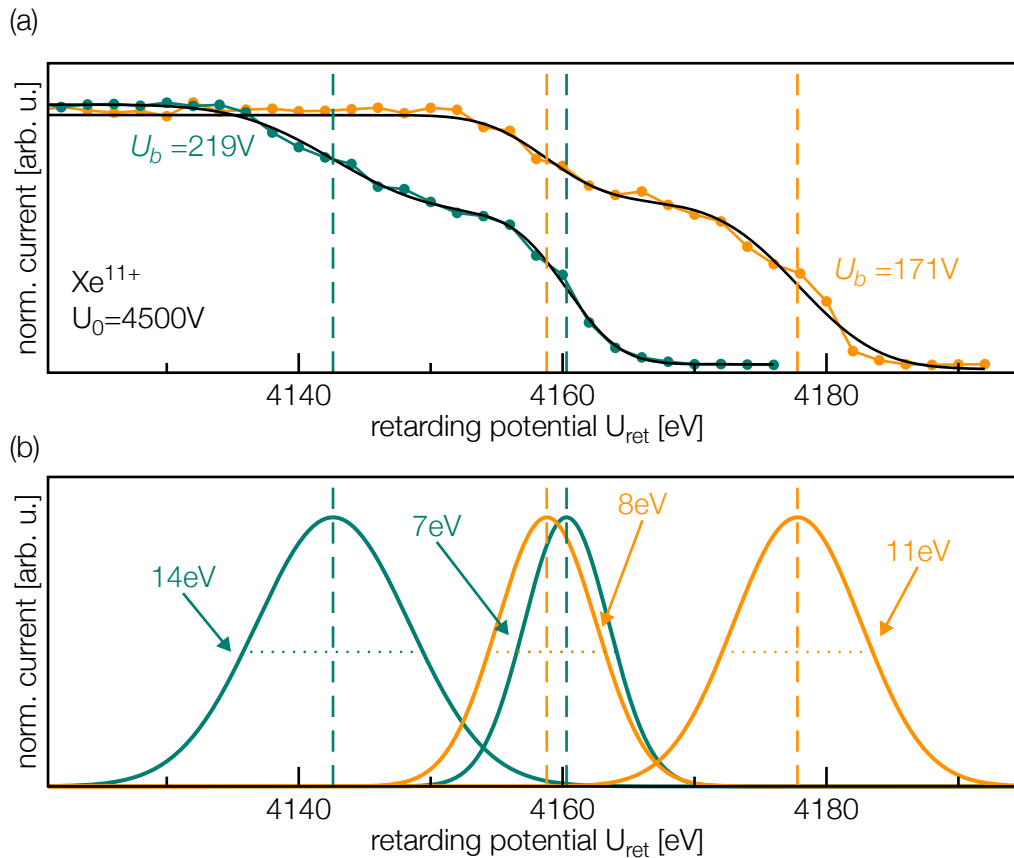
Figure 3.18: (a) Xe^{11+} current measured for U_b=171 V (yellow line) and U_b=219 V (green line) and fitted with an error function according to equation 3.10 (black lines). (b) Beam energy spread obtained from derivatives of signals measured in (a). Dashed lines represent the mean of the Gaussian shaped distributions. Figure adapted from [90].

Beam energy analysis at the MCP detector

With collimator slits already described in previous sections the energy dispersion of the extracted beam can be further minimized. It is analyzed at the end of the drift chamber by the energy dependent spreading of the beam inside the deflection plates. The voltage applied to the deflection plates is varied and the beam profile is recorded at the DLD for 10 eV Ar^{2+} ions, shown in figure 3.19. The received energy distribution is a convolution of the energy width extracted from the source chamber f and the width resulting from the slit apertures in the experimental chamber g (derived from the beam profile without deflection voltage).

$$F(f * g) = F(f) \cdot F(g) \tag{3.11}$$
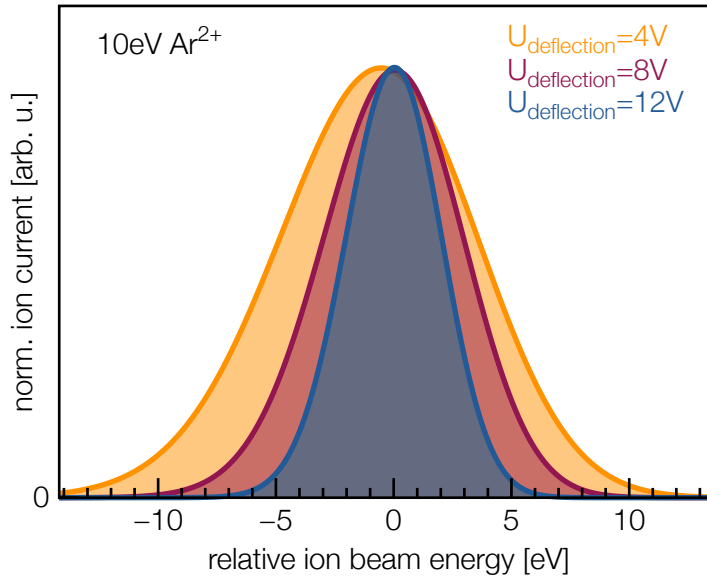
Figure 3.19: Final ion beam profile after deconvolution of signals recorded at the MCP detector shows a maximum energy spreading of 10 eV.

When measuring g and f ∗ g, according to the convolution theorem in equation 3.11, the energy dispersion of the initial beam f can be derived. Here, a Gaussian form of f is assumed, which can be expressed through

$$f(y) = e^{-a(y+b)^2}. \tag{3.12}$$

Transformation of f(y) in f(E) leads to a final energy dispersion of less than 10 eV, shown in figure 3.19.

3.9.3 Time of Flight Measurements

An example for a recorded TOF spectrum using a pulsed ion beam as START trigger and the impact of the projectiles at the MCP as corresponding STOP, was already presented in figure 3.3. According to equation 3.5 the measured TOF can be used to derive the ion's energy loss within the target. When applying the electron emission induced by ion impact on the sample

as START signal ions simply passing holes in the target will only create a STOP signal and contribute therefore merely to the noise in the spectrum. This implies that recorded TOF signals always belong to ion's suffering energy loss. Hence, the TOF T_0 for ion's with their initial energy E_0 has to be calculated following to equation 3.5 to further derive the energy loss from recorded spectrum.

Conversion into Energy

The x-axis of a TOF spectrum can be converted into an energy-axis according to the following equation:

$$E = \frac{mv^2}{2} = \frac{ms^2}{2t^2},$$
(3.13)

and the corresponding energy loss for ions with an initial energy E_0 after extraction from the source consequently results in:

$$E_{loss} = E_0 - E = E_0 - \frac{mv^2}{2} = E_0 - \frac{ms^2}{2t^2},$$
(3.14)

with m as the mass, v as the velocity of interacting ions and t as the time they need to travel the distance s.

However, when converting a TOF spectrum f(t) into an energy loss spectrum $\tilde{f}(E)$ one has to consider that E is inversely dependent from t^2. The non-linear transformation has to fulfill the following requirement:

$$\int f(t)dt = \int \tilde{f}(E)dE$$
(3.15)

$$\int f(t)dt = \int \tilde{f}(E)dE$$
$$\tilde{f}(E(t)) = f(t)\frac{dt}{dE}$$
(3.16)

and the conversion into an energy loss spectrum $\tilde{f}(E)$ follows:

$$\frac{dt}{dE_{loss}} = \frac{t^3}{ms^2}$$

$$\tilde{f}(E_{loss}(t)) = \frac{f(t)t^3}{ms^2}$$

(3.17)

Figure 3.20 shows the typical procedure from converting the received TOF spectrum into a corresponding ion's energy. T_0 and E_0 represent the calculated TOF and energy for Xe^{30+} ions extracted with 130 keV from the source chamber, respectively. The spectra are fitted (black lines) by an analytic approximation of the Landau distribution, a Moyal function:

$$f(x) = \frac{a}{\sqrt{2\pi}\sigma} \exp\left(-\frac{1}{2}\exp\left(\frac{x-\mu}{\sigma}\right) + \frac{x-\mu}{2\sigma}\right),$$

(3.18)

for which $\sigma \rightarrow -\sigma$ in case of the TOF spectrum has to be applied. Further, the energy loss of ions through a SLG sample can be deduced (compare figure 3.20c).
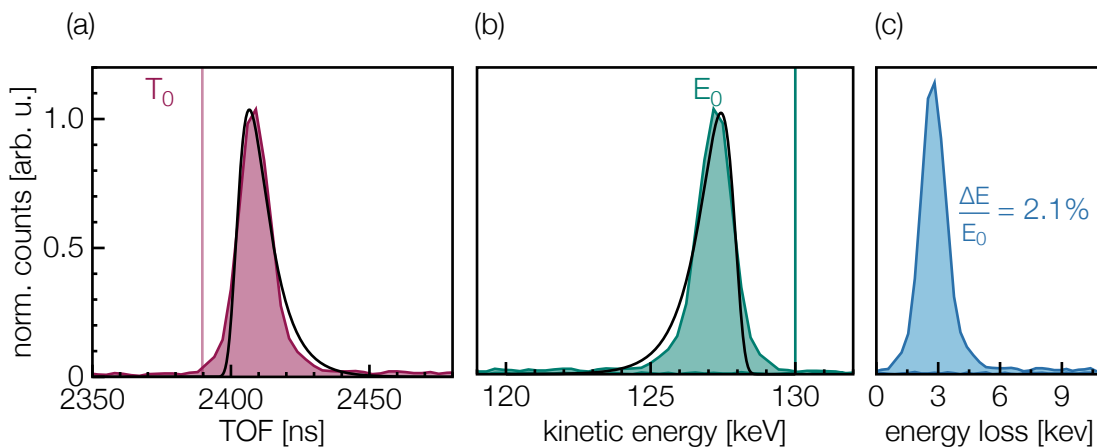
Figure 3.20: (a) Recorded TOF spectrum (red) for 130 keV Xe^{30+} through SLG. The black line represents a Moyal fit to the data. (b) Converted energy distribution according to equation 3.15 shows again a Moyal distribution (fit in black). (c) Energy loss for 130 keV Xe^{30+} passing SLG extracted from a TOF spectrum.

Calibration

In general, the initial ion beam energy E_0 can be determined by the known source potentials U_0 and U_b by means of $q \times (U_0 - U_b)$. Even tough fluctuations in U_0 and U_b are reasonably small (<420 mV in leaky mode), there remains an uncertainty in the extracted beam energy, which is highly required for energy loss measurements. As it was discussed in the previous section 3.9.2, different starting positions for ions created in the source chamber or a geometry dependent deceleration behaviour further contribute to a broadening in the initial ion energy. Therefore, T_0 derived from $E_0 = q \times (U_0 - U_b)$ cannot be promptly applied for calibrating a TOF spectrum and further extracting an energy loss.

Also, electronic delays and data processing times lead to an offset in the measured TOF, which has to be considered in data evaluation. To precisely define this TOF offset a calibration (reference) sample (SLG) was chosen. The energy loss of ion's with a certain initial energy and charge state was measured at the Ion Beam Center at the HZDR using an electrostatic analyzer with an angle acceptance of 1.6° and an energy resolution of $\Delta E/E \approx 1.5 \times 10^{-3}$ [40]. By applying exactly the same extraction and source potentials to the EBIS-A at the NIELS setup, TOFs were recorded for transmission through the same sample. The extracted energy loss for ions in a certain exit charge state were compared.

Figure 3.21 shows the TOF spectrum for ions in an exit charge state of 6+ after the transmission of Xe^{30+} ions through the reference sample. Converting the received TOF distribution, which can be fitted by a Moyal function, into an energy spectrum delivers the yellow distribution shown in figure 3.21b. The vertical lines marked with T_0 and E_0 correspond to the calculated TOF and initial ion energy, respectively. Due to an offset in the recorded TOF and an uncertainty in the initial beam energy, the measured data do not match with the calculated values. The Moyal shaped energy loss for $q_{exit}=6$ measured with the electrostatic analyzer was added into the plot. When converting the TOFs into energy and shifting the results according to the estimated offset, an agreement of measured energy distributions recorded at the HZDR and Vienna can be found, depict in figure 3.22). Note that the energy resolution of the MCP detector is by a factor of 2 worse than the precise electrostatic analyzer. However, the procedure was repeated for various exit charge states and an average TOF offset of 385 ns, present in all recorded data, could be derived.
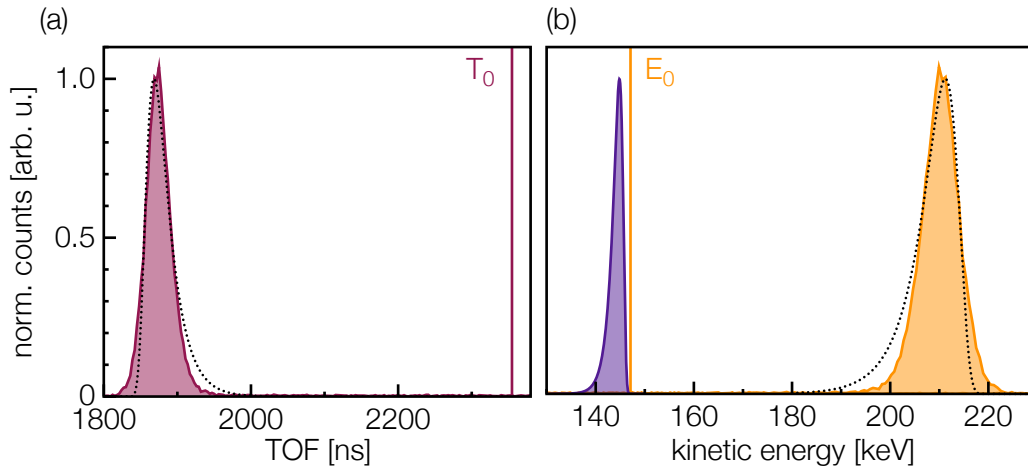
Figure 3.21: (a) recorded TOF spectrum for Xe^{6+} ions after transmitting Xe^{30+} through single layer graphene. The red line depicts the actual calculated position for ions with the chosen initial energy of 147090 eV without any energy loss. (b) The yellow peak shows the ions energy distribution after transmission through the sample corresponding to the TOF peak in (a) without correcting the TOF offset. The purple Moyal distribution $q_{exit}=Xe^{6+}$ was measured with an electrostatic analyzer at the HZDR for the same SLG sample.
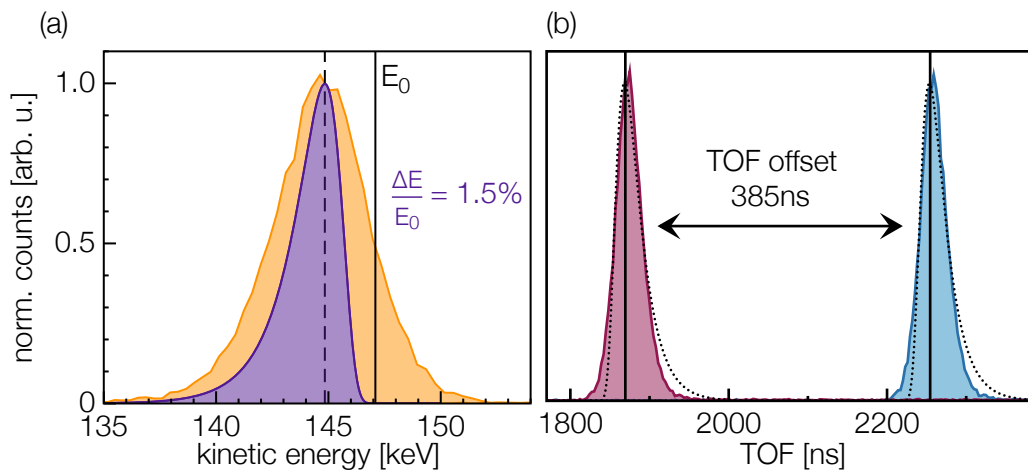
Figure 3.22: (a) When shifting the TOF by an offset, the converted energy distribution (yellow) overlaps with the Moyal distribution (purple). (b) An offset of 385 ns due to electronic delays, processing time and uncertainty in the initial ion beam energy can be extracted.

Filtering of 2D spectra through ion's TOF

A big amount of currently available freestanding 2D materials placed on QF grids come with the big disadvantage that the actual area covered by the 2D flake is often <50% or even less (compare figure 3.23).

Electron beam driven hole during imaging
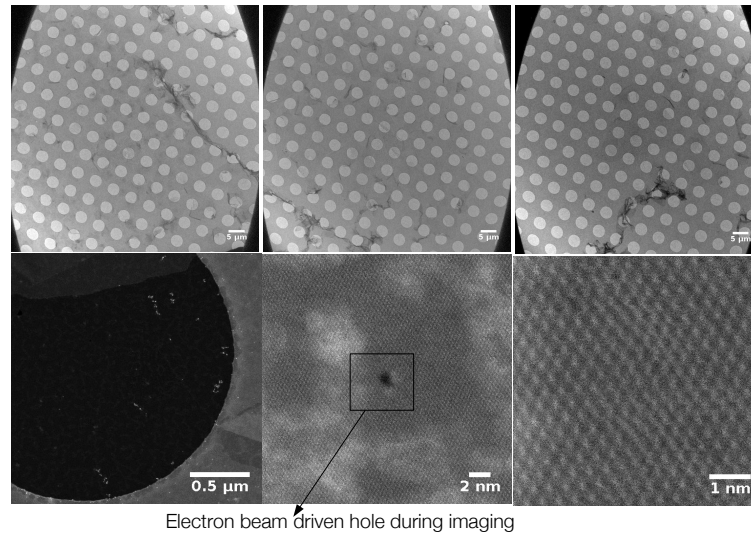
Figure 3.23: Clean sample but MoS$_2$ coverage of QF grid only ~45% coverage. STEM images recorded at the University of Vienna (H. Inani and M. Tripathi).

Macroscopic holes or ruptures of the membranes are the consequence of demanding transfer processes of such thin layers onto the grid and are often inevitable. Ion transmission studies of such samples therefore become rather difficult, since many ions pass the target without any interaction but nevertheless are detected at the MCP. Such ions, still in their initial charge state, are always present and will further on be referred as 'primary ions'. They contribute to the noise in the TOF recording (signal-to-noise ratio of 2:1 in spectrum shown in figure 3.24b) since they only deliver a STOP signal without a corresponding START (triggered by electrons). For samples in which the coverage rate is very low (<50%) and the scattering angle of ions with the specific target are large, i.e. the detection angle is small in contrast to the scattering angle, those ions will dominate the recorded 2D spectrum and the actual desired exit charge state distribution will vanish within the noise. Such a situation is present in figure 3.24a in which the exit charge states of 87 keV Xe^{30+} ions transmitted through a monolayer of MoS$_2$ were recorded. However, after recording the data, such a 2D spectrum can be filtered through the corresponding TOF spectrum. Figure 3.24 shows an example for such a data processing. The 2D spectrum shows mainly 'primary ions' impinging on the MCP. Since the recorded TOF spectrum results only from ions interacting with the sample and the QF support film in case the ion's energies are high

enough, the TOF peaks can be used as a filter and the time window can be set as a condition for the 2D spectrum accordingly. Figure 3.24c shows the exit charge state distribution originating from the actual interaction with the sample appearing once the TOF filter (green marked TOF range) is used. Using the TOF peak for ions passing the support grid (blue marked TOF range), reveals that all ions neutralize within the QF carbon support film (figure 3.24d). Further, such filter conditions can, for example, also be used for deriving the corresponding electron emission yield for a certain exit charge state.
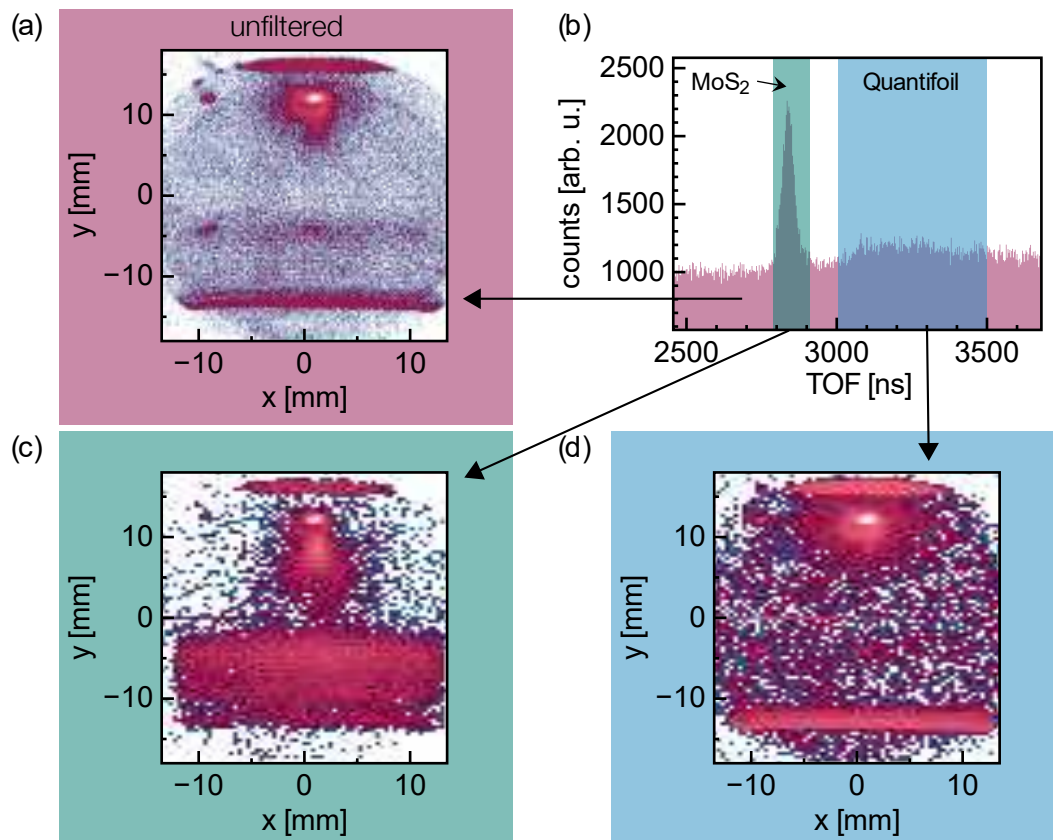
Figure 3.24: (a) Recorded exit charge state spectrum for 87 keV ions passing a MoS$_2$ sample. (b) Corresponding TOF spectrum of (a). Green range highlights the TOF peak for ions actually interacting with the target. The blue range indicates interaction with the QF support film. (c) Filtered exit charge state spectrum for green marked TOF in (b). (d) Ions transmitted through target support (blue marked range in (b)).

3.9.4 Electron Emission Statistics

The particle-induced electron emission statistics using a surface barrier detector biased at high voltage, is an acknowledged technique and has proven its applicability in various experiments in the past 30 years [16, 18, 68, 70, 87, 109–112]. Particle emission such as PE lasts no longer than 10^{-13} s [113] and also subsequent KE processes are finished within 10^{-11}-10^{-12} s [114]. Hence, all electrons emitted due to one ion impact reach the detector within its time resolution ($\sim 0.5\,\mu$s) and are therefore counted in one pulse. The height of this pulse equals the deposited energy. Therefore, n arriving electrons counted simultaneously deliver one pulse with a total height of $E_e = $ nx30 keV rather than n individual pulses. Apparently this results in an upper limit of impinging ions, since an ion flux of ≥ 10 kHz leads to inevitable pulse pile-up. However, some of these electrons might backscatter from the detector with a certain possibility p_r [16, 87] and therefore deposit only a fraction E_b of their energy E_e. Especially for high yield spectra this effect leads to a smearing out of the recorded spectra and has therefore to be considered in the following yield evaluation process.

Yield Evaluation

Besides measuring the mean number of emitted electrons $\bar{n} = \gamma$ in an ion impact event, also the number statistics for n emitted electrons can be extracted. The measured electron emission yield γ is a superposition of individual probabilities W_n for the emission of n electrons.

$$\gamma = \bar{n} = \sum_{n=0}^{\infty} nW_n, \sum_{n=0}^{\infty} W_n = 1 \tag{3.19}$$

Note that the probability for no emission of an electron W_0 cannot be directly measured, but can be neglected for $\gamma \geq 3$ [18]. In general, the probability of independently emitted electrons should obay a binomial distribution which further approaches a Poisson statistics [109] for a large ensemble of electrons:

$$W_n(\gamma) = \frac{\gamma^n e^{-\gamma}}{n!} \tag{3.20}$$

This obedience holds as long as PE contributions are comparable small and therefore the measured yield is low. For a high number of emitted electrons n a clear deviation from the Poisson distribution is observed [87]. Recorded spectra show a superposition of n individual peaks for which each peak n should be Gaussian distribution centered around the deposited energy $E_e = n \times 30\,\text{keV}$. Due to a certain backscattering probability p_r for each electron, the form of the spectrum deviates from its Gaussian shape. The contribution of backscattered electrons can be considered in the yield evaluation procedure by assuming a possibility of $p_r = 17\%$ for backscattering of 30 keV electrons from bulk Si [115] and an average fraction of $E_b = 0.6 \times E_e$ deposited energy [116]. For yield evaluation of a typical measurement, the spectrum can be fitted by a linear combination of n normalized functions $F_n(E_e)$, which would be Gaussian-shaped and centered around $n \times 30\,\text{keV}$. Including electron backscattering, each $F_n(E_e)$ can be seen as the sum of m individual peaks f_n for m-fold electron backscattering [16, 87]:

$$F_n(E_e) = \sum_{m=0}^{n} P_n \cdot f_n(E_e, E_m, \Delta E_m). \tag{3.21}$$

The f_ns are normalized functions of Gaussian shape centered around

$$E_m = n \times 30\,\text{keV} - m \times 0.6 \times E_e \tag{3.22}$$

with a FWHM of

$$\Delta E_m = \sqrt{(\Delta E_{Det})^2 + m \cdot (\Delta E)^2}. \tag{3.23}$$

Each function $f_n(m)$ is weighted with a certain probability $P_n(m)$, which all obey the binomial statistics:

$$P_n(m) = \binom{n}{m} p_r^m (1 - p_r)^{n-m} \tag{3.24}$$

Following this procedure, a measured spectrum $S(E_e)$ can be fitted according to:

$$S(E_e) = \sum_{n=0}^{n_{max}} C_n \cdot F_n(E_e). \tag{3.25}$$

with fitting parameters C_n which correspond to the emission probabilities $W_n = kC_n$ of n electrons. Further, the electron emission yield can simply be derived from equation 3.19 [16, 87]. However, for yields $\gamma \geq 20$ the inelastic backscattering of electrons smears out the individual peaks in the spectrum and the described fitting routine becomes no longer feasible. Instead the resulting smoothed spectra can be fitted by a Gaussian. The mean of this fit can be directly related to the electron emission yield corrected by a factor α when including the shift of the spectrum due to electron backscattering [19]. With a fraction of deposited energy k_r (typically 60%) by backscattered electrons and again, a probability p_r (17% for Si active layer of detector) for backscattering, the extracted mean of the Gaussian shaped fit has to be multiplied with

$$\alpha = \frac{1}{(1 - p_r(1 - k_r))} \approx 1.07. \tag{3.26}$$

Calibration

The received pulse heights are stored in the MCA into 8192 channels. Those channels have to be calibrated into deposited energy, i.e. number of emitted electrons. In principle, this procedure has to be performed every single time the PIPS detector is newly operated, since the calibration crucially depends on the applied acceleration voltage and the amplification settings in the electronics. Low-yield spectra for which individual peaks can be identified, usually obtained from field emission, are recorded and their position (in channels) is assigned to an electron number. Not necessarily, the first determined peak has to result from the emission of one electron due to an internal minimal threshold of the amplification electronics as well as the analyzing software. Therefore, spectra for different acceleration voltages are recorded and the peak positions (in channels) are determined. The peak position versus the electron number follows a linear behavior, shown in figure 3.25. The crossing of the individual fits shows the position for "zero" electron emission.

With a lower resolution but therefore stored in a listmode file together with the ion's TOFs and impact positions, the electron emission yield can also be derived from the electron's timing signal, processed in the CFD1x, as presented in figure 3.12. Here, the pulse height corresponds to a pulse width, stored in a histogram via the CoboldPC software. Therefore, the received timing signal (in ns) has to be calibrated in an electron emission yield. As the yield is known from the procedure described above, both spectra can be recorded at the same time and the pulse width (in ns) can be assigned to the corresponding yield as this is depict in figure 3.26.
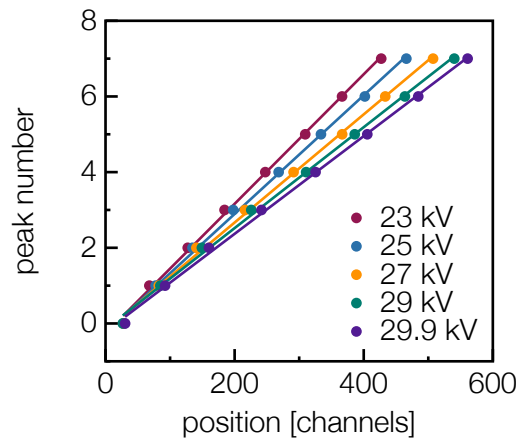
Figure 3.25: Field emission spectra are used to assign each peak in the recorded pulse heights, which are stored in MCA channels, a number of emitted electrons.
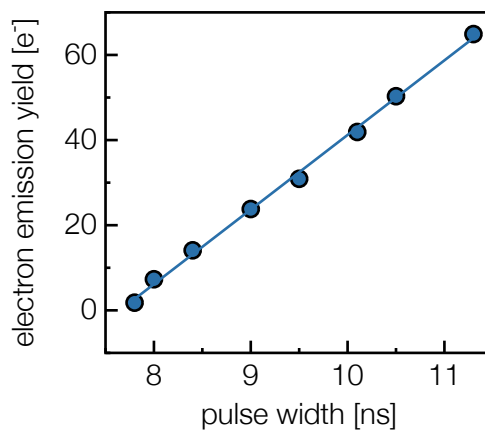
Figure 3.26: Electron emission yields determined from pulse height spectra and assigned to pulse widths extracted from CFD1x output.

This procedure was performed for Xenon ions with various incident charge states resulting in electron emission spectra with different yields used for the calibration. A Au(111) single crystal was chosen as a sample. In figure 3.27 an example for the simultaneously recording of the pulse width received from the CFD1x output and the corresponding pulse height for 87 keV Xe^{40+} impact is shown.
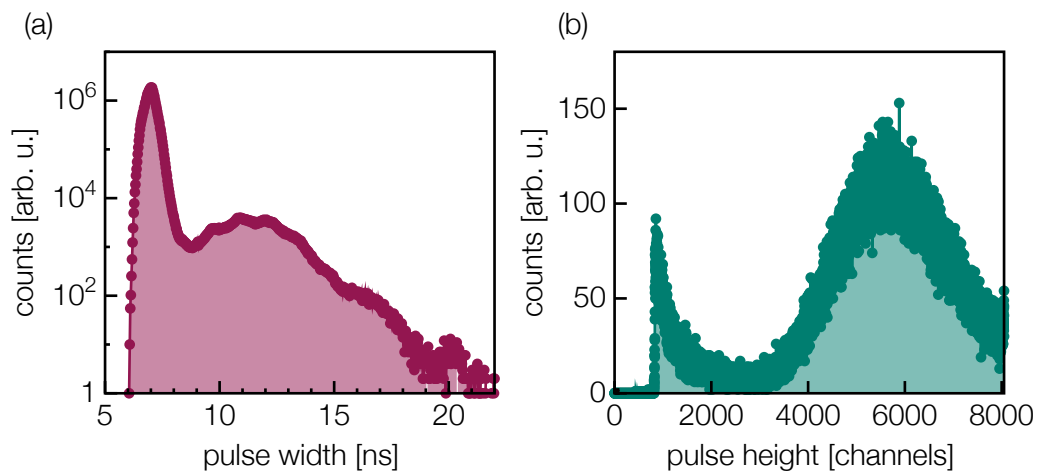
Figure 3.27: (a) Pulse widths of the CFD1x output stored in a listmode file by the CoboldPC software. (b) Pulse height spectrum for recorded electron emission from single crystalline Au(111) induced by 87 keV Xe^{40+} ions. Spectra (a) and (b) recorded at the same time.

Collection Efficiency

Electron collection efficiency is a crucial point in electron statistics measurement, as it represents the largest contribution to the total experimental error. In general, it depends on the geometry of the setup as well as the electrostatic potentials inside the experimental chamber and therefore also on the energy of ejected electrons. Further, especially for low-energy ions the trajectory of the ions itself can be influenced by the electric fields leading to a change in the impact point on the sample and therefore a slight change in the collection efficiency as it has been already discussed in section 3.4.3. The attempt was made to keep the collection efficiency for a series of measurements constant by optimizing the applied voltages (repeller, grids, frame) and a collection efficiency of $\sim 70\%$ was estimated from IBSIMU and Simion simulations for most of the measurements. Additionally, to check the collection efficiency for each measurement a reference single crystalline Au(111) sample was present in a different slot in the target holder. The change in the collection efficiency for different target slots is only a minor effect as it was found in [94] when determining the electron emission yield for a target in each slot. Since the xenon induced electron emission yield for a clean single crystalline Au(111) surface is very well known [17–19], the measured spectra were analyzed and the extracted yield was compared to results from former studies [8]. Also here, typically $\sim 70\%$ were found to reach the active area of the detector.

4

Single Layer Graphene

The interaction of HCIs with freestanding SLG in terms of emitted particles and ion exit charge states as a consequence of ion deexcitation within this material is discussed. The experimental methods have been published in [42] while results on x-ray and electron emission following from ion impact and interaction processes are discussed in detail in [43, 44]. Therefore parts of the following chapter are excerpt from these publications [42–44].

4.1 Properties & Sample Preparation

Graphene, the thinnest material and regardless the strongest one as well, has made its rapid way into modern experimental and theoretical hot topics in science since its first realization in 2004 [26]. At first, few layer graphene was isolated via mechanical exfoliation from highly oriented pyrolytic graphite. Graphene is the given name for carbon atoms densely packed into a single atomic plane and arranged in a hexagonal structure with a carbon atom-atom distance of 1.42Å [26]. Eventough later discovered, with its two-dimensionality, it provides the basis for other carbon allotropes as fullerenes (0D) can be seen as wrapped up graphene, carbon nanotubes are basically obtained by rolling graphene along a given direction resulting in a 1D structure while graphite (3D) is obtained by stacking of individual graphene layers. However,

graphene shows a number of properties completely different from its 1D or 3D counterparts. A sp^2 hybridization between the s-, the p_x- and p_y- orbitals leads to a σ bound connecting each carbon atom with three neighbors. The remaining p_z-orbital is oriented out of plane and leads to a half filled Π band. The conduction band is fully occupied while the valence band remains empty. The two bands touch each other only at the Dirac point, hence the linear dispersion makes graphene to a zero-bandgap semiconductor, a semimetal.

Its excellent electronic properties arise from the free-moving electron of the p_z-orbital along the plane [117]. Carrier mobilities of up to $\mu \approx 10.000\,cm^2V^{-1}s^{-1}$ at room temperature, ballistic transport and strong sustainabilty against currents of up to 10^8 A/cm^2 make graphene to a highly favoured candiatate for metallic transistors [26]. Among many others, record values in thermal conductivity at room-temperature ($\sim$ 5000 W/mK) [118] and breaking strength of $\sim$ 40N/m above the theoretical limit and a Young's modulus of $\sim$ 1.0TPa [119] have been reported [31]. To summarize, since its first discovery graphene has been and still is treated as a promising candidate for a wide range of potential applications such as faster and more efficient electronics, solar panels, flexible displays, biosensors, water filtration membranes and many more. While a majority of them still remain speculative applications in future, some have actually already been applied in modern industry - and more in smaller niche applications. For example, with its low atomic mass a single layer of graphene can nowadays been used as support for atomic resolution TEM [120].

Since the first mechanical exfoliation of few layer graphene [26] in which mechanical forces are applied to split the layers of a bulk apart, this process has further been automatized by using ultrasonic cleavage [121]. As an alternative, graphene can nowadays be grown epitaxially by CVD on top of other crystals such as Cu or Ni [122]. When the growing process is stopped and the structure is cooled down, the substrate can be removed by chemical etching. PMMA masks are used to support the monolayer and enable the transfer onto the desired substrate. After the transfer the polymer film is dissolved by using acetone [123, 124].

For present ion transmission studies, highly transparent support grids are required to enable freestanding 2D samples. Therefore, TEM grids with additional QF support as shown in figure 3.4 were chosen as substrate. Since any residual from the transfer process via the PMMA mask might influence the transmission results, sample transfer was conducted as described in [97] without the use of any polymer film at the University of Duisburg-Essen. For comparison, commercially available freestanding CVD grown graphene samples from Graphenea [125], for which up to 10% residuals from the transfer process might have remained, were used as well.

Once the "Upgrade II", described in section 3.8, was installed in the setup all samples were annealed at 400°C for ∼ 30 minutes and kept at 180°C during the whole measurement procedure. It is reported that PMMA residuals facing the graphene begin to evaporate at 200°C [103], which is why the annealing procedure was especially essential for Graphenea samples [90]. However, keeping the target at 180°C, was beneficial for every sample as it should prevent additional hydrocarbons or water molecules (which are always present in the experimental chamber) from attaching to the sample.

4.2   Charge Exchange

Slow HCIs were transmitted trough a freestanding monolayer of graphene and the ion's exit charge states were recorded at the MCP detector. Extensive work on ion transmission through graphene has already been performed by Wilhelm and Gruber [38,39] and the conclusion of their investigations has been published (among others) in [40]. Ultra-fast charge exchange between highly charged Xenon ions and a single layer of graphene was reported. The first aim was to reproduce these findings with the new setup rather than with an electrostatic analyzer and in a second step clean the samples in-situ to validate the results.

Transmission of slow HCIs through graphene shows a Gaussian shaped exit charge state distribution with a FWHM of about 3-5 electrons. This was already reported in [39] and could be reproduced within this work using a different detection technique. Figure 4.1 shows the "charge exchange", i.e. the number of captured and stabilized electrons, for 170 keV Xe^{30+} measured with an electrostatic analyzer with an acceptance angle of 1.6° and compared to the recorded MCP signal integrated over a scattering angle of ±0.25°. The SLG sample was produced at the University of Duisburg-Essen using no polymer film for the transfer process. A mean exit charge state of q = 10±1 for both measurements can be derived, even if the spectrum extracted from the DLD shows a slightly broader distribution. We attribute this feature to the presence of contamination which will be discussed in the chapter below. Since the electrostatic analyzer setup does not allow the measurements of ions in low charge states and neutral particles, the spectrum ends already at an exit charge state of $q_{exit} = 5$. In contrast, for the first time, neutrals resulting from HCI-graphene interaction could be recorded with the MCP detector, maybe with somewhat lower efficiency since the secondary electron yield is charge state dependent [38].

For 1 nm thin amorphous carbon foils (CNMs) exit charge states were analyzed for various projectile scattering angles (0°, 2° and 4°) in [39]. While high charge states are only observed in forward direction, the low exit charge states are still witnessed for projectiles scattered under
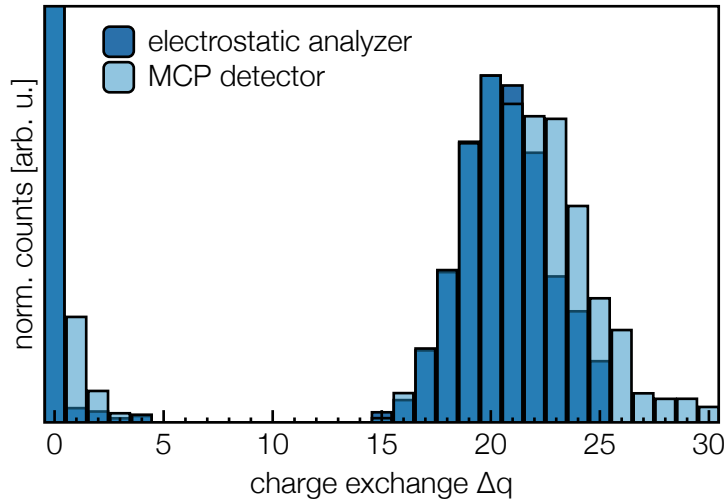
Figure 4.1: Histogram of the number of electrons captured and stabilized by a 170 keV Xe[30+] ion transmitted through freestanding SLG and recorded with an electrostatic analyzer [40] and with the MCP detector for comparison. Data have been published in [42].

slightly higher angles (maximum exit angle of 5.34° for Xe single scattering on C) with a significant decrease in intensity. In principle, the setup allows tilting angles of the detection system of up to ±8°. Therefore Xe scattering on SLG was investigated by recording spectra within the whole accessible detection angle range, an example is shown in figure 3.16. In all measurements a big drop in the intensity for scattering under higher exit angles was found [108]. However, most ions observed under such larger exit angles resulted from interaction with contaminations on the sample as could recently be shown [90] via cleaning procedures. In our experiments, the largest exit angle of ions transmitted through cleanSLG was found to be ±1°. Further, no rainbow scattering of protons, as this was proposed theoretically in [126], could be observed for 5 keV H^{+} ions on graphene.

Transmission spectra were recorded for different incident Xe[q+] (q=20,25,30,35) ions over a broad ion velocity range and the mean exit charge state was derived as the mean of the Gaussian distribution extracted from the recorded MCP spectra integrated over a scattering angle of ±0.25°. The charge exchange Δ q, i.e. the number of captured and stabilized electrons by the ion, with the freestanding graphene membrane is shown in figure 4.2 and plotted versus the interaction time τ

$$\tau = \frac{d_{eff}}{v} \tag{4.1}$$

with a charge state dependent effective thickness d_{eff} derived from TD-DFT calculations [40] and v as the ion's incident velocity. The data are compared to measurements of Gruber et al. [40] and fitted in the same way according to

$$\Delta q = q_{in} - q_{exit} = q_{in} \cdot (1 - e^{-\frac{\tau}{\tau_n}}). \tag{4.2}$$

However, one has to note that for our experiments the used SLG samples were not cleaned in first place in order to allow a direct comparison to data points measured by Gruber et al. (opened circles in figure 4.2). The exit charge state of the ions after their transmission has not yet reached its equilibrium charge state [127] revealing an incomplete neutralization of the HCI. However, an estimation for the time an ion needs to be neutral, the neutralization time constant τ_n, can be derived from the fit to the presented data for each charge state. With an on average neutralization time of 1.35 fs for each investigated Xe charge state, these findings further support the assumption of an involved multi-electron charge transfer process suggested in [41]. While in Gruber et al. [40] a linear increase with increasing incident charge state was reported (1.4 fs and 2.2 fs for Xe^{20+} and Xe^{35+} respectively), measurements presented in figure 4.2 lead to a more or less constant neutralization time value of 1.35 fs, depicted in the inset. This might result from a contamination layer on top of our samples, not present in samples used earlier by Gruber et al. [40], leading to an enhanced neutralization of the HCI. Therefore, results and comparison with samples treated with the cleaning procedure described above follow in the section 4.5.

4.3   X-ray Emission

As it is so far not clear whether the ICD process populates the ground states of an approaching HCI directly or only low lying excited states while leaving inner-shell holes unoccupied, radiative as well as non-radiative deexcitation remain as possible energy release channels.

To check this, x-ray and Auger electron emission for Xe^{q+} and Ar^{q+} on graphene was recorded. Spectra were measured at the setup described in [38] equipped with a windowless Bruker XFlash silicon drift detector at the HZDR. A sketch of the experimental setup can be seen in figure 4.3. X-rays as well as electrons having energies above 700 eV can be recorded. The detector has an energy resolution of $\Delta E = 140$ eV at 5.9 keV and is calibrated by using Mn-K_α and Mn-K_β emission lines of a mounted ^{55}Fe source. Also here, spectra were recorded in
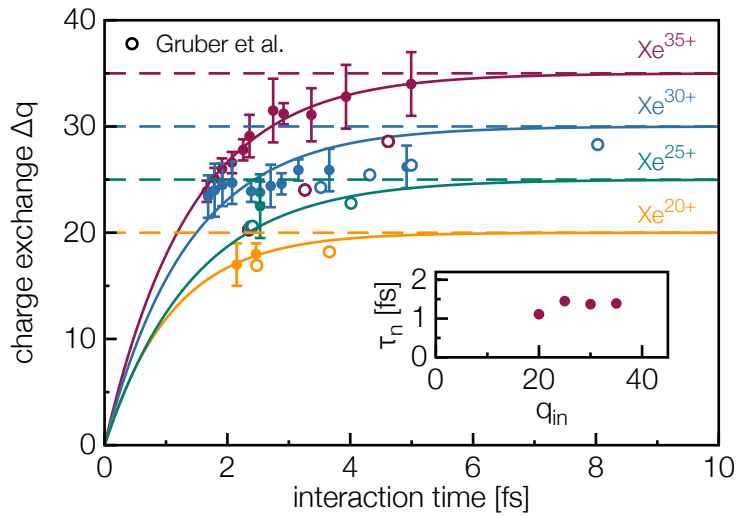
Figure 4.2: Charge exchange of Xe^{q+} ions with freestanding SLG versus interaction time measured at the NIELS setup (full circles) and compared to data in [40] (open circles). Inset shows the charge state independent neutralization time constant derived from the fit according to equation 4.2.

coincidence with transmitted ions registered at the channeltron at the exit of the electrostatic analyzer.
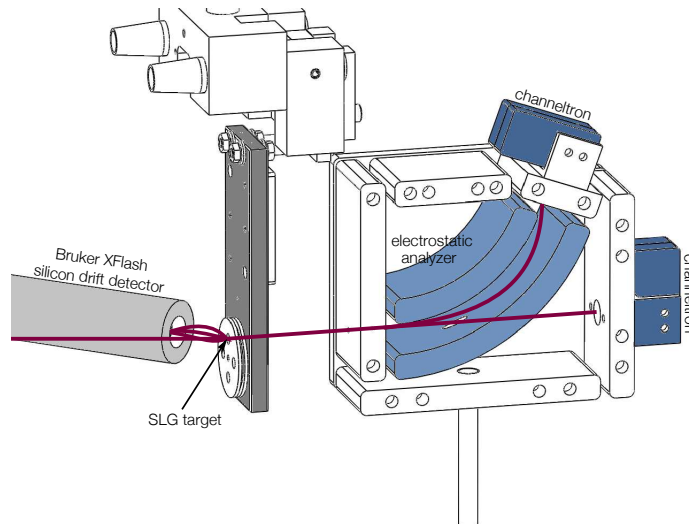
Figure 4.3: Silicon drift detector and electrostatic analyzer with channeltrons for coincident measurement of emitted electrons/x-rays and transmitted ions at the HZDR [43].

X-ray and Auger electron emission as measured for initially 75 keV Ar^{17+} ions following from interacting with a graphene sheet is shown in figure 4.4a. The radiative filling of the K-shell

hole can be concluded by observing the characteristic K_α and K_β lines for Ar. Energies and transition rates for various electronic configurations of Ar have been calculated by using an atomic structure code [51]. When a Gaussian detector function with a FWHM of 140 eV is assumed, the measured x-ray spectrum can be reproduced (red filled plot) and shows K-shell filling at the presence of L- and M-shell vacancies. More precisely, the measured K_α energy of 3006 eV corresponds to about 3 present vacancies in the L-shell. X-ray emission following from ion interaction with only a monolayer, is compared to spectra resulting from impact on bulk material [128]. Therefore, data on Ar^{17+} impact on Be have been added in figure 4.4 (blue line). The comparison shows very similar results with only a slightly broadened K_α peak towards lower energies which probably results from a poorer detector resolution.
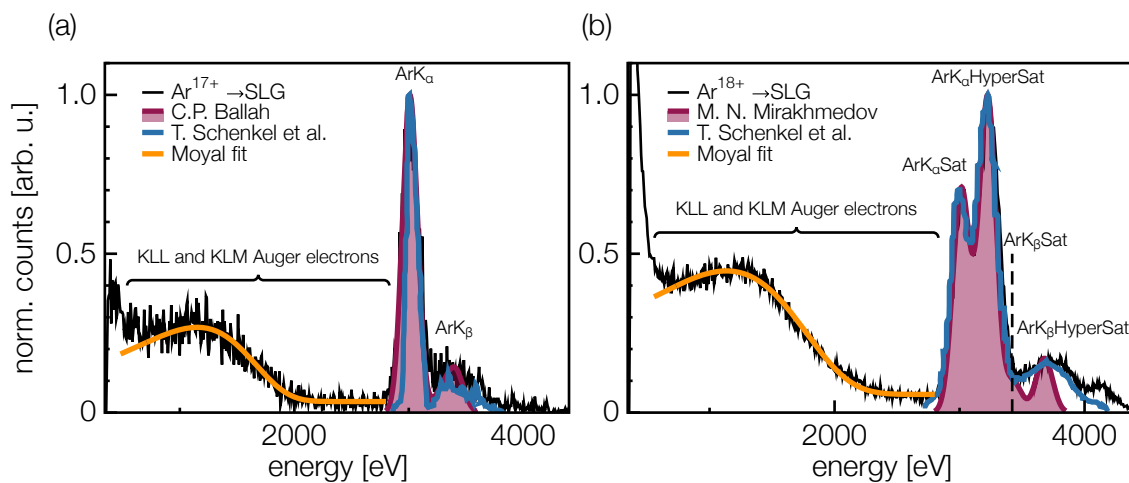
Figure 4.4: Auger electron and x-ray emission recorded for (a) 75 keV Ar^{17+} ions and (b) Ar^{18+} impact on SLG. Data are compared to calculations (red filled line, [51, 129]) and measurements on a Be surface (blue line, [128]). Auger electrons contribute to the spectrum and their energy loss is fitted with a Moyal fit (orange line).

Since a windowless detector is used, even electrons with energies above 700 eV (KLL and KLM Auger electrons) are measured as a broad distribution starting at an energy of about 2.8 keV and ranging towards the noise level. When fitting the distribution with a Moyal fit, mimicking the electrons straggling and energy loss within the dead layer of the detector, the contribution of electrons to the spectrum and therefore to the K-shell decay can be extracted. According to this estimation about 1.7 times more vacancies decay via Auger electron emission than radiatively [43].

The same procedure was performed for 75 keV Ar^{18+} ions transmitted through SLG. Also here, the results agree to calculated transitions [129] (red filled line) and measured x-ray emission from

a bulk material [128] (blue line). The stepwise filling of the two K-shell holes is represented by the K_α and K_β satellite and hypersatellite lines. The observed transition energies again correspond to unoccupied vacancies in the L-shell while K-shell filling takes place. Note that the Ar K_β satellite line is less pronounced and therefore marked as a dashed line in figure 4.4b. However, there is a prominent peak observed in the spectrum at an energy of 4130 eV, not present in the calculations and to some small extend in recorded x-ray emission following from interaction with a Be target. Such a transition energy was measured for Ar^{18+} interaction with residual gas atoms [130]. Also here, the authors compared their finding to a bulk Be target and could not observe any transition at such high energies due to enhanced screening of many present spectator electrons in the metal surface.

Therefore, the monolayer of hexagonal arranged carbon atoms, might represent an intermediate case between a 3D solid and a gas target [43] as screening is also reduced in the 2D case.

Also for bare Ar, the K-shell holes were partially filled via non-radiative transitions leading to a broad KLL- and KLM electron energy distribution. The contribution of such electrons to the recorded spectrum is about 1.8 times higher than the one by x-rays if one assumes that electrons and x-rays are detected with equal efficiency by the silicon drift detector.

To study the influence of the ion's initial charge state, x-ray emission for Xe ions with initially 0, 1, 4, 7, and 9 M-shell vacancies was recorded and the kinetic energy was kept constant at 100 keV for each charge state. The radiative filling of the M-shell with electrons from the N-shell can be clearly seen in figure 4.5 for all ions having initially vacancies in the M-shell (Xe^{27+}-Xe^{35+}). The broad distribution rather than separate emission lines originates from the multitude of electronic configurations present during the transition. For Xe^{22+} only the high energy tail of N-shell filling with electrons from higher n-shells can be seen due to the cut-off at an energy of about 400 eV via the low-level discriminator.

The main peak in the other spectra results from 4f → 3d transitions and is centered at 790 eV for Xe^{27+} and at 1030 eV for Xe^{35+}. The shift towards higher energies for increasing charge state can be interpreted as the presence of less spectator electrons. For each additional M-shell vacancy the peak shifts about 30 eV, remarked in figure 4.6. The less likely 4p → 3d transition is only present as a low-energy shoulder of the main peak in figure 4.5. A long tail towards high energies indicates high n-shell transitions (e.g. 30f → 3d) and therefore the presence of a HA in the moment the transition occurs can not be neglected. However, the dominance of the 4f → 3d transition peak suggest that the main fraction of radiative decay occurs when almost all inner shells are already filled [43], i.e. as a second step after collective electron demotion via ICD.
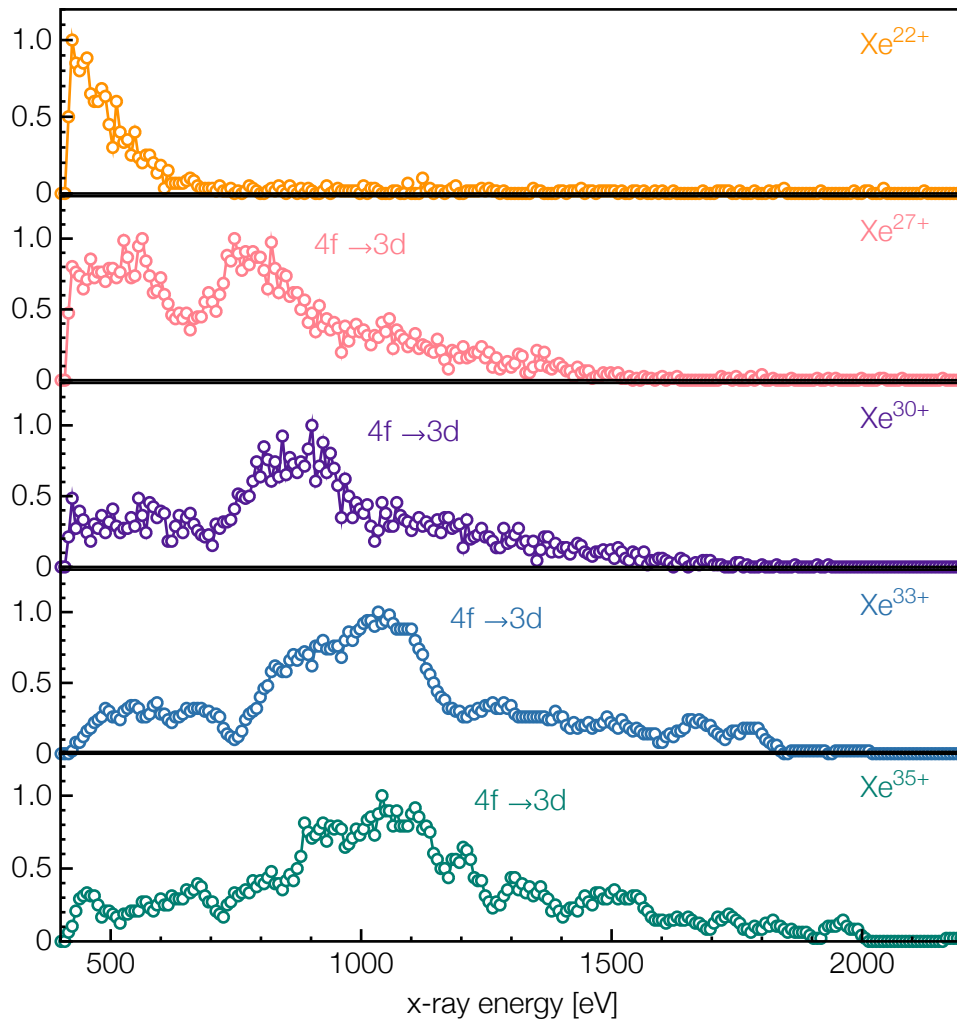
Figure 4.5: Radiative M- and N-shell filling for 100 eV Xe^{q+} recorded in coincidence with ions transmitting through SLG. Figure adapted from [43].

A much more detailed investigation of M-shell filling for slow (3 keV × q) highly charged Xenon ions (q=26-40) interacting with metal foils such as Be is performed at the Jan Kochanowski University in Kielce, Poland [131]. Also here, the authors measure nl → 3d transitions (n ≥ 4) with various multiple vacancy configurations. Additionally, they precisely calculated transition energies using the GRASP code based on a multiconfiguration Dirac-Fock (MCDF) method and could reproduce the measured x-ray spectra following from M-shell filling of electrons in higher-n-shells. The high energy tail for ions in higher charge states, e.g. Xe^{35+}, is concluded to result from transitions in which two electrons but only one photon is involved. Thus, x-rays at higher energies are measured [132].
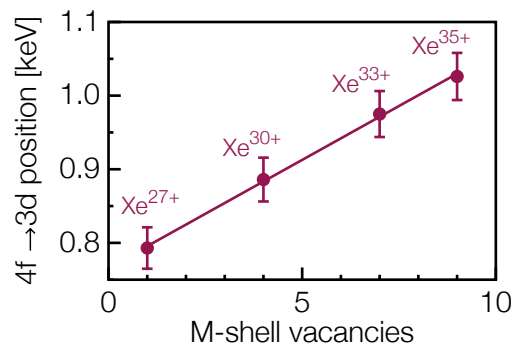
Figure 4.6: Increasing energy for 4f → 3d transition with increasing Xe charge state (about 30 eV for each additional M-shell vacancy). Figure adapted from [43].

4.4 Electron Emission

As it was just discussed in the section above, the filling of shell vacancies by non-radiative transitions is equally or even more important than radiative decay. However, the filling of such inner shell-holes occurs only as a second step following the quenching of electrons from high-n Rydberg states into intermediate states via ICD as indicated x-ray measurements performed in Kielce [131]. In ICD energy is released via the emission of many electrons from nearest and next-nearest neighboring carbon atoms [41]. Hence, many electrons ejected at the same time having low energies are to be expected.

4.4.1 Number Statistics

The number of electrons emitted due to a single HCI impact on SLG was recorded in coincidence with transmitted ions registered at the DLD. While KE is mainly determined by the ion's velocity, the measured PE strongly depends on the ion's charge state as already known from HCI impact on solid surfaces. Hence, the measured total electron emission yield increases for higher charge states as the ion's potential energy is converted into electronic excitation in the target leading to electron emission. Also for a 2D material such as graphene, the increase in the yield with increasing charge state was measured in this thesis, as this is shown in figure 4.7 for Xe^{20+}, Xe^{30+} and Xe^{40+} ions while keeping the kinetic energy constant at 87 keV. The x-axis was calibrated and corrected for electron backscattering as described in chapter 3. The data are fitted with a Gaussian shaped function while the mean of the distribution is indicated as a dashed line in (a) and plotted versus the incident charge state in (b). No saturation of the yield

with increasing potential energy can be observed for the semimetal monolayer. An electron depleted regime around the ion impact point would lead to suppression in the electron emission. Therefore it can be assumed that charge is resupplied promptly enough due to the high electron mobility within the graphene plane. These findings are well in agreement with suppressed Coulomb explosion in SLG as no hole formation is observed after exposing the monolayer to a strong localized field created by a slow HCI [40].
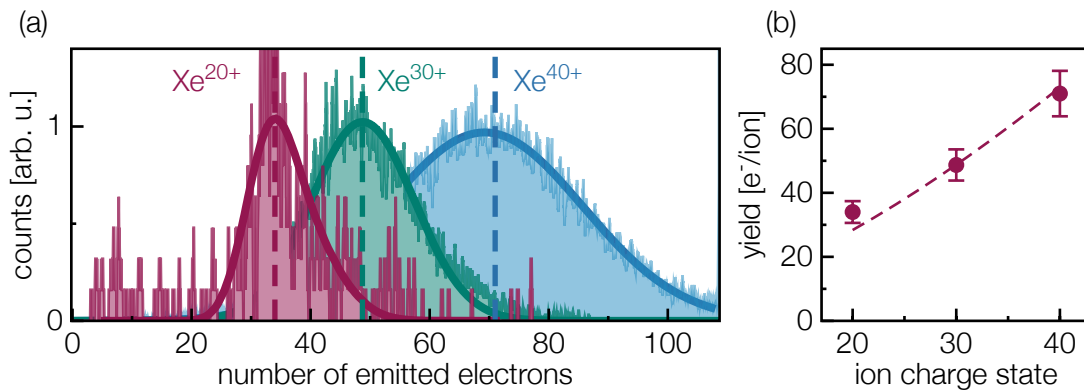

Figure 4.7: (a) Recorded electron statistic spectra for 87 keV Xe^{20+}, Xe^{30+} and Xe^{40+} ions fitted with a Gaussian shaped function. The dashed line indicates the extracted mean value of the distribution and is plotted in (b) versus the ion's incident charge state in which the dashed line is to guide the eye. Data adapted from [44].

When varying the kinetic energy, however, the electron emission yield tends to stay rather constant for a specific incident charge state within the error bars of the investigated velocity regime. In figure 4.8 the velocity dependent total electron emission yields are plotted in the inset for Xe^{20+}, Xe^{30+} and Xe^{40+} ions. All data were recorded under normal incidence with respect to the target's surface and therefore it can be ensured that the thickness of the monolayer is not artificially enlarged. The mean number of emitted electrons averaged over the whole velocity regime was extracted for each charge state and plotted in the main figure. Again, no saturation of the electron emission yield with increasing applied potential energy for graphene is observed.

When the assumption is made that only valence electrons with ionization energies $\leq 10eV$ contribute to the HCI deexcitation via ICD, only one electron per carbon atom will be emitted as the ionization energy for the second valence electron is already enhanced. A total electron emission yield of $\sim 70\,e^-$ for a Xe^{40+} ion therefore indicates that about 70 carbon atoms participate in the charge exchange process. However, the average value of $70\,e^-$ per Xe^{40+} ion is only a lower estimate since the collection efficiency was estimated to be only about $\sim 70\%$. If we correct
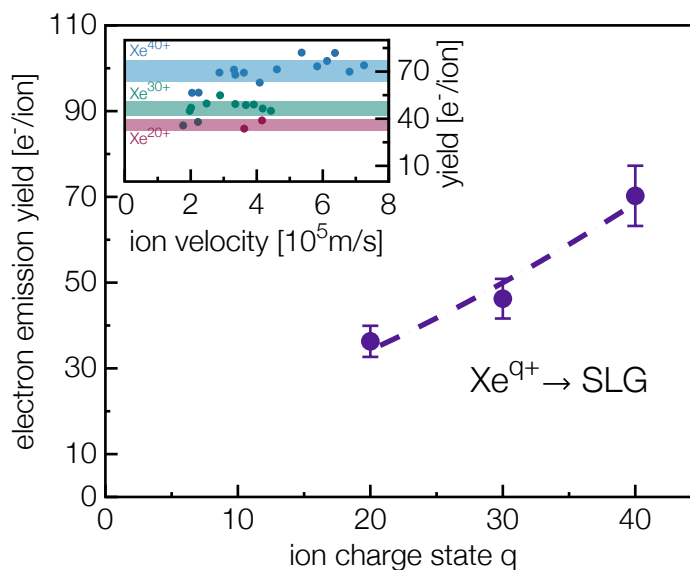
Figure 4.8: Total electron emission yield for Xe^{q+} impact on SLG averaged over the ion velocity range for each charge state presented in the inset. The dashed line is to guide the eye. The colored areas in the inset indicate an uncertainty band of ±10% (error bars in the main figure). Figure adapted from [44].

for this (total yield of 90 electrons) and take also the additionally 23 electrons captured and stabilized by a 2 keV/amu Xe^{40+} ion [40, 42] into account, a partially charge depleted area in the graphene can be determined. With a carbon atom density of 38.3 C atoms/nm^2 in graphene we calculate an electron extraction area of about 3 nm^2, i.e. a radius of r=1 nm, around the impact point of the projectile. This is still smaller than the defect radius identified by Kozubek et al. [104] for slow HCI bombardment of suspended SLG. With the help of Raman spectroscopy, here a defect radius (radius for structural disorder according to [133]) of 1.5 nm in a freestanding SLG sheet after bombardment with 2 keV/amu Xe^{40+} was identified. Thus, the electronic excitation of the target spreads considerably before being converted into permanent lattice distortion.

The high electron emission yield along with the fast ion neutralization we observe, further supports the model of HCI deexcitation via ICD since it requires the contribution of many surrounding carbon atoms. However, besides ICD there are other processes which might lead to electron emission and their contribution to the total measured yield will now be discussed.

In the presented data, the disentanglement between electrons resulting from PE and KE can hardly be made. Even tough one would expect the contribution of kinetic emission from a surface-only material to be rather small, we can estimate the general contribution of KE based

on measurements from single charged Xe impact on carbon surfaces for which no PE is to be expected.

The total measured electron emission yield from graphene induced by Xe^{40+} interaction is again presented in figure 4.10 along with experimental data for Xe^+ impact on carbon foils [134], on carbon velvet [135] and on HOPG [136, 137]. A linear fit through these data from literature shows, that at an ion velocity of 7.2×10^5 m/s (maximum accessible ion velocity in the setup) less than 10% of the total measured electron can result from KE. Further, an intra-atomic Auger-type decay cascade has to be considered as a possible electron release channel. If a HA is formed but is still too far away from the surface for ICD to set in, autoionization of the projectile might occur. Additional, as inner-shell vacancies can survive the ICD quenching electron emission can follow as a result of their decay. The rates for such processes were calculated for specific HA configurations by using a state-of-the-art relativistic atomic structure code MCDFGME (Multi Configuration Dirac–Fock and General Matrix Element) [138, 139]. For occupied principle quantum number of up to n=13, the rates do not exceed values of 10^{13}s^{-1}. Also, the Cowan code [140] was used in [20] to estimate a scaling behavior for transition rates in a HA.

$$R_{AI} = \frac{2.1 \cdot 10^{14} s^{-1}}{(\Delta n)^{3.46}} \tag{4.3}$$

For Xe^{40+} the fastest decay for one of the 14 M-shell vacancies is therefore found for electron transitions from the N-shell ($\Delta n = 1$) with a value of $R_{AI} = 2.1 \cdot 10^{14}$s^{-1} according to equation 4.3. We can estimate a maximum number of electrons emitted within the interaction time τ due to such an autoionization of the projectile by assuming an exponential decay of inner shell vacancies N_{vac}:

$$N_{vac}(t) = N_{0,vac} \cdot e^{-R_{AI}t} \tag{4.4}$$

The interaction time can again be expressed via the effective interaction distance, which is depict in figure 4.9. An initial 40+ charged Xe ion with a velocity of v=7.2×10^5 m/s reaches an exit charge state of about q_{exit}=21+ after transmission through graphene. Critical electron capture distances can now also be calculated from the model described in [20] according to equation 2.1 and assuming a work function of 4.5 eV for graphene. Therefore a maximum interaction distance $R_C = R_{C1} + R_{C2}$ is determined, consisting of the critical distance for first

electron capture R_{C1} = 2.87 nm for Xe^{40+} above the surface and R_{C2} = 2.09 nm for Xe^{21+} possible charge exchange after transmission through the target.
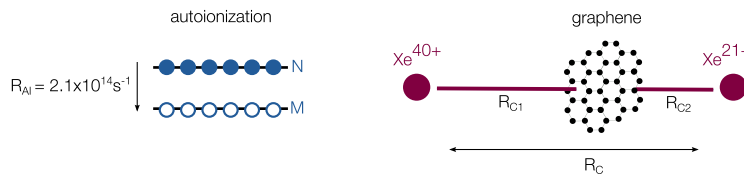
Figure 4.9: Sketch of the filling of a M-shell vacancy with the fastest autoionization rate for $\Delta n = 1$ (left). Distances for first electron capture R_{C1} above and for possible charge exchange after transmission R_{C2} are depicted (right).

With a total interaction time for electron transport processes of $\tau = \frac{R_C}{v} \sim 7$ fs, the maximum number of emitted electrons via autoionization is found to be $N_{vac}(\tau) = 10.7 e^-$. Together with the estimated upper limit for KE contribution to the total yield, the remaining $57 e^-$ (80%) very likely result from HA deexcitation via ICD [44].
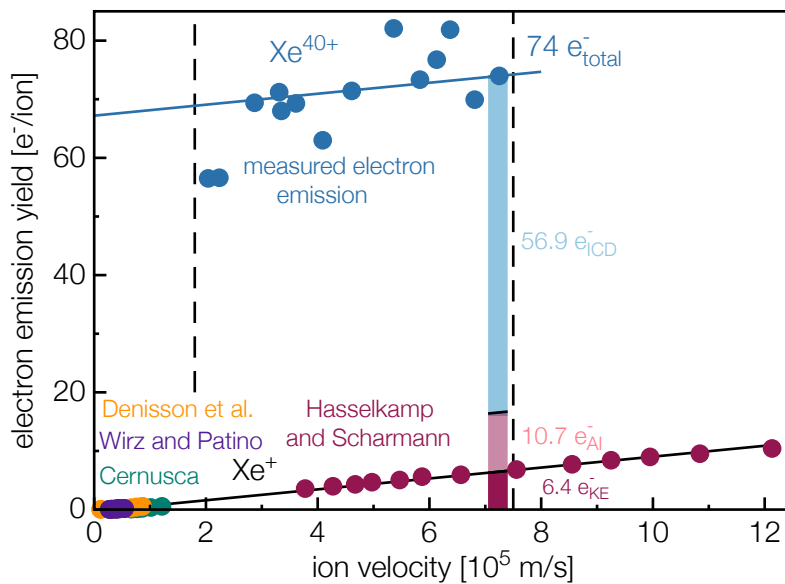
Figure 4.10: Velocity dependent electron emission yield measured for Xe^{40+} interaction with SLG. Data for Xe^+ impact on carbon foils, carbon velvet and HOPG are added from [134], [135] and [136, 137], respectively. Figure adapted from [44].

4.4.2 Electron's Energy Distribution

Besides the large number of electrons, ICD suggests also low energies for such electrons. Therefore, a pair of retarding grids was used to analyze the electron's energy distribution. The first grid was grounded while the second grid was used to ramp voltages starting at 0 V and reaching voltages for which no further electron was registered at the PIPS detector. The results for electron emission from graphene induced by Xe^{40+} ions are compared in figure 4.11 for 80 keV and 180 keV initial kinetic energy. The measured signal was fitted with an errorfunction according to

$$f(E) = a \cdot \text{erf}(b \cdot e^{-cE}) \tag{4.5}$$

and the negative derivative of this fit was used to determine the electron's energy distribution, plotted in figure 4.11b.
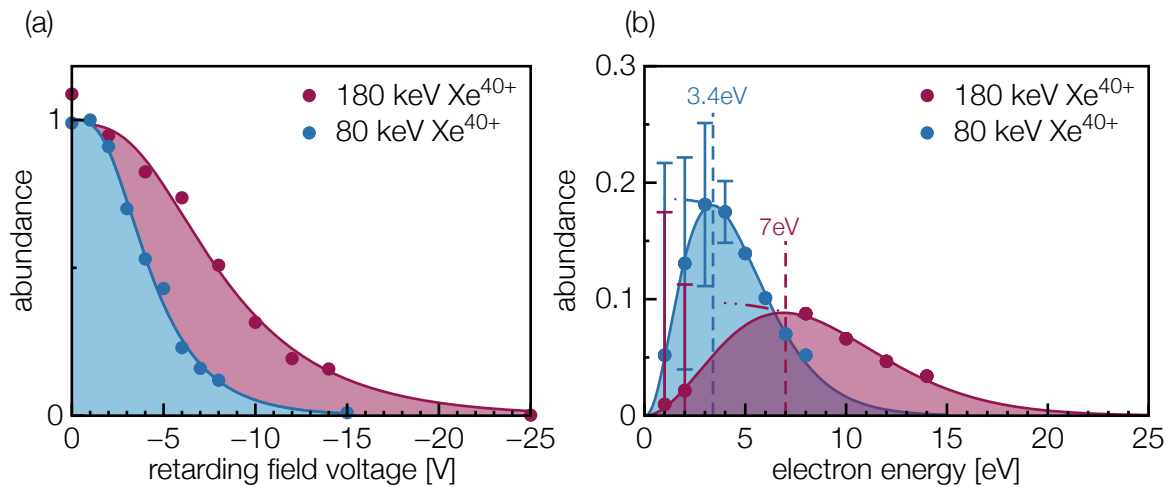
Figure 4.11: (a) Recorded signal for electron emission following from 80 keV (blue) and 180 keV (red) Xe^{40+} ion interaction. (b) Derived electron energy distribution for data in (a). Figure partially taken and adapted from [44].

Using a one-layer material only, allows to analyze the electron's energy directly after emission since no further energy loss or multiplication within the material is expected as this would be the case for a 3D solid. We find that the majority of electrons have energies well below 20 eV with a mean value of 3.4 eV and 7 eV for 80 keV and 180 keV Xe^{40+}, respectively. Note that the uncertainties towards low energies become relatively large (blue and red error bars) since

without a µ-metal shielding of the experimental chamber we have to expect influences in the electron's trajectories through external magnetic fields. However, this would lead to a shift of the whole distribution towards even lower energies. Low-energy electron emission again supports HCI deexcitation via ICD.

4.5 Results on Clean Samples

In order to assign the just discussed results to the interaction with a monolayer of graphene only, perfectly clean samples are necessary. Especially when starting working with commercially available SLG targets, residuals such as PMMA from the transfer process had to be expected on top of the 2D layer. Further, hydrocarbons present in the experimental chamber always tend to stick onto the surface. Therefore samples where heated up above 400 C° as well as treated with the installed laser. A detailed review on removal of contaminations is given in [90] and the main results will be put into context with the results on graphene presented so far. In figure 4.12 the comparison of a heavily contaminated SLG sample before and after the cleaning procedure is shown. For present contaminations a low exit charge state (a) and a high energy loss reflected in the measured TOF of transmitted ions (b) is observed. When heating the sample up, a slight change in the observed spectra occurs already at temperatures between 50 C° and 180 C°. We assume within this temperature range the desorbtion of surface contaminations such as hydrocarbons and water molecules. A bigger effect in the exit charge state and the measured TOF is observed between 250 C° and 360 C° when either the removal or a clustering into thicker islands of PMMA and other residuals occurs. The temperatures necessary for polymer removal from a graphene surface are in agreement with [103].
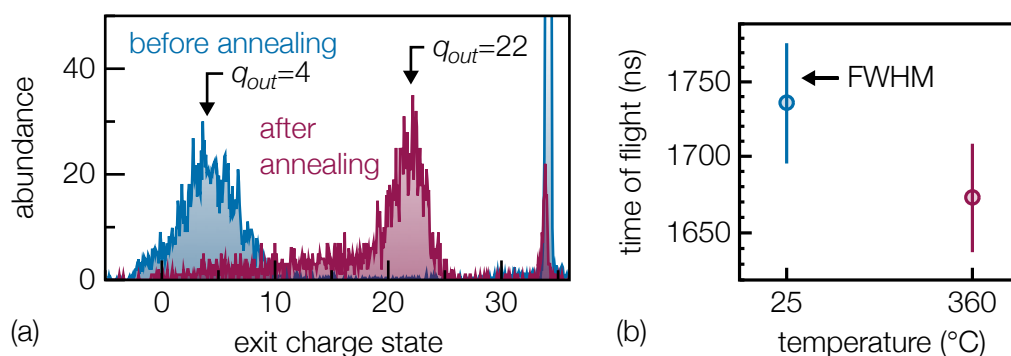
Figure 4.12: (a) Exit charge states of initially Xe^{34+} ions after transmission through a contaminated (before) and clean (after) graphene sample. (b) Measured TOF for ions in (a) before and after cleaning procedure. Figure take from [90].

Since the presence of contaminations turned out to have a strong effect on the exit charge states, especially for SLG samples with polymer assisted TEM grid transfer, charge exchange was remeasured after including Upgrade II in Vienna as well as at the HZDR with an electrostatic analyzer [45]. Results are shown for different incident Xenon charge states and fitted again according to equation 4.2 in figure 4.13. From the fit, a neutralization time constant can be extracted and is compared to results from Gruber et al. [40] where polymer-free SLG samples were used and heavier contaminated samples already presented in figure 4.2. While for the latter an almost constant neutralization time constant was derived, already data in [40] showed a linear increase with increasing charge state and an even steeper slope appears for the properly cleaned samples. However, the neutralization time for contamination free SLG still remains below 10 fs.
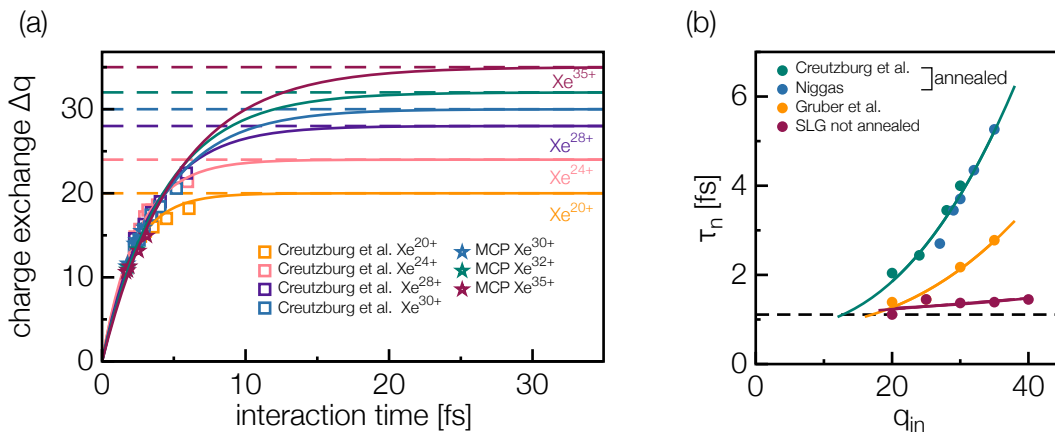
Figure 4.13: (a) Charge exchange of Xe^{q+} with annealed SLG measured at the HZDR [45] by means of an electrostatic analyzer and in Vienna with the MCP detector [90]. (b) Extracted neutralization time constant for annealed samples in (a), slightly contaminated [40] and heavier contaminated SLG. Dashed line represents the minimum neutralization time required for a contaminated sample while the straight lines are added to guide the eye approaching this value.

Further, contaminations on the surface can contribute to the measured total electron emission yield. Therefore, electron emission from SLG was recorded after sample annealing and TOF filtering. Example spectra for 87 keV Xe^{40+}, Xe^{35+} and Xe^{30+} are shown in figure 4.14a. The mean of the Gaussian shaped and backscattering corrected distributions are plotted in figure 4.14b and compared to data points for contaminated samples. Even tough the detection resolution for the TOF filtering method gets worse (larger error bars), surprisingly the measured electron emission yield increased for annealed samples. In case of Xe^{40+}, for instance, additionally 34 electrons leave the target sample. A possible explanation for this observation might

be the higher exit charge state compared to a projectile charge state after through transmission a heavy contaminated target. As a consequence, the time for electron exchange after exiting the monolayer would be increased as the distance of first electron capture also scales with the charge state (equation 2.1). Therefore, additional electron might be emitted due to ongoing AI processes after target transmission. A second reason for the observed increase in the measured electron emission yield for annealed SLG samples might be the absence of contaminations possibly preventing emitted electrons from leaving the surface. A conceivable possible situation might also be local charge-ups in the contamination layers, also hindering electrons to be ejected into vacuum.
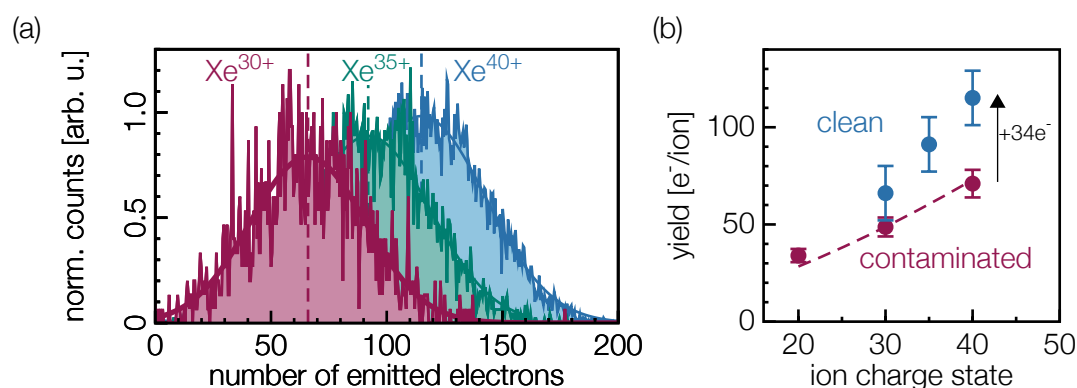
Figure 4.14: (a) TOF filtered number of emitted electrons for 87 keV Xe^{q+} transmission through cleaned graphene. (b) Extracted yield from (a) (blue) and compared to results presented before in figure 4.7.

4.6   Discussion

The asymmetric combination of a heavy Xe projectile and low mass embedded C target atoms makes the system to an ideal candidate for probing HCI deexcitation via ICD as it limits possible other deexcitation channels [41]. Even with annealed samples for which we can ensure a thickness of a monolayer only and therefore an ultimately short interaction time, we observe neutralization within femtoseconds. To enable this via resonant transfer of electrons into high Rydberg states followed by an autoionization cascade, still Auger transition rates in the order of $10^{16} - 10^{17} s^{-1}$ would be necessary. Even when it comes to the filling of inner-shell holes for which the lifetime strongly decreases, maximum rates of $10^{14} - 10^{15} s^{-1}$ are reported [52]. The direct filling of intermediate and core holes via Auger neutralization requires an overlap in the wave functions of target electrons and core orbitals which is rather small for highly charged

Xe ions having a few hundreds to keV deep inner-shell states. Further, other processes are excluded and discussed in detail in [41] making ICD to the only possible deexcitation channel.

Due to the simultaneous decay of many electrons from highly exited Rydberg states into intermediate core states, energies in the keV range are stored in the system. The additional gained energy is transferred via virtual photons to the graphene's electronic system and leads either to electron emission into vacuum or exited states in the graphene. We measure up to 100 ejected electrons from a monolayer semimetal having low energies, which strongly supports the assumption of HCI decay via ICD. ICD not neccessarily populates inner-shell vacancies which still allows Auger neutralization and radiative decay to follow as the last steps in the HA deexcitation.

However, the sudden charge removal within the graphene sheet strongly polarizes the target which provokes Coulomb repulsion. Usually, within such a thin membrane Coulombic explosion follows and as a consequence nm-sized holes are created [7]. However, when TEM images of freestanding graphene sheets (see figure 4.15b) are consulted after HCI irradiation no ion-induced damage can be observed. Therefore we draw the conclusion that the removed charge is resupplied promptly enough due to the high carrier mobility within the semimetal [40, 141].

(a)

1 nm

10 nm

(b)

10 nm
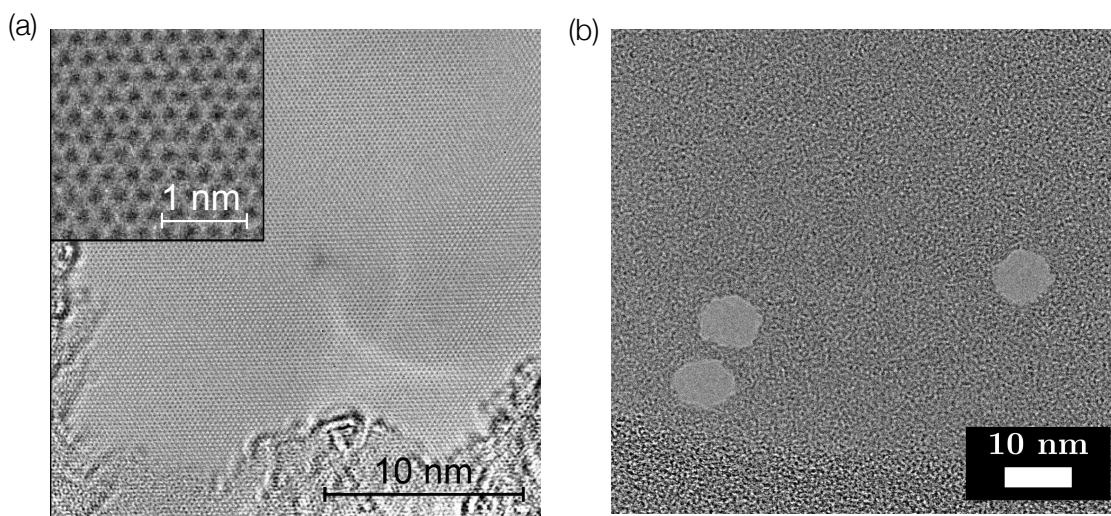
Figure 4.15: (a) TEM image taken from [40] showing SLG after 180 keV Xe^{40+} irradiation without any topographic defects. (b) CNM TEM image taken from [8] after 179 keV Xe^{40+} bombardment showing nanometer sized pores in the membrane.

When we compare the exit charge state with the incident charge state and take PE into account, we can estimate the fraction of energy deposited into the target. The total energy balance reads as follows:

$$E_{tot} = E_{pot}(q_{in}) + E_{kin}(q_{in}) = E_{pot}(q_{exit}) + E_{kin}(q_{exit}) + E_{dep} \tag{4.6}$$

with a kinetic energy of the outgoing ion, depending on the kinetic energy loss ΔE_{kin} in the target, sputtered carbon atoms and possible KE contribution:

$$E_{kin}(q_{exit}) = E_{kin}(q_{in}) - \Delta E_{kin} - n_{sput} \cdot E_{sput} - \gamma_{KE} \cdot E_e \tag{4.7}$$

The deposited energy mainly depends on the potential energy introduced into the system and the energy lost via electron emission and x-ray radiation:

$$E_{dep} = E_{pot}(q_{in}) - E_{pot}(q_{exit}) - \gamma_{PE} \cdot E_e - E_{rad} \tag{4.8}$$

As an example, again results for 87 keV Xe^{40+} presented above are used to estimate the various contributions. For the annealed SLG sample we measure up to 115e$^-$ per ion impact having low-energies ($\sim 3.4\,eV$) and an exit charge state of $q_{exit} = 25$. The kinetic energy loss ΔE_{kin} can be extracted from more precise energy loss measurements in graphene with an electrostatic analyzer and is found to be $\Delta E_{kin} \sim 2\,keV$ [39]. KE contributions from graphene are estimated to be less than 10%. Elastic collisions may cause sputtered C atoms through direct knock-on with a maximum energy transfer of $0.311 \cdot E_{kin}(Xe)$ [107]. On average less than one C atom per Xe ion is sputtered from graphene [142].

Over all, for 87 keV Xe^{40+} we find 30437 eV ($E_{pot}(Xe^{40+})$–$E_{pot}(Xe^{25+})$) potential energy deposited into the system, while at least 391 eV are released via electron emission. If we assume x-ray emission as a minor contribution, the remaining $\sim 30\,keV$, which is about 78% of the initial potential energy, are deposited into the system via thermalization. This is well in agreement with earlier studies on energy deposition of multiply charged ions into solids [143], for which a fraction of 80% ± 10% was found to be deposited into the system and only 10% ± 5% to be emitted into vacuum via x-ray emission, low-energy electrons, plasmons, Auger electrons, secondary atoms and ions. Even earlier studies already concluded that only 10% of the available potential energy in fact leaves the system again [128].

However, all this studies focused on energy deposition into a bulk for which energy can at least dissipate within a few layers. It is rather surprising that we find up to 80% of initial energy remaining in a 2D system too without damaging the membrane.

5

Bi- and TriLayer Graphene

Via stacking of individual graphene layers on top of each other (A-B-A stacking) multilayer graphene in the end results in having crystalline graphite. When choosing only two or three layers, extraordinary properties of the 2D layer can be preserved or even improved as for example a tunable overlap between conduction and valance band exists for trilayer graphene (TLG) in contrast to bi- or monolayers. Electron and hole mobility at low temperatures are still found to be higher in bulk graphite, however a clear dependence on the layer number has not been reported yet [144]. Further, bilayer graphene (BLG), for instance, shares outstanding properties such as its high electrical and thermal conductivity at room temperature and the possibility to tune carrier densities by doping and gating with its monolayer counterpart. Among a number of other properties they have in common, BLG graphene presents the thinnest possibility for intercalation making it a favorable candidate for applications. In general, bi-, tri- and multilayer graphene are consider for many future devices which require increased electrical or thermal conductivity, strength or specific optical features [145]. However, when observing the extreme resistance of a monolayer graphene against a high localized field created by an approaching HCl, it became apparent to test the response of multilayer graphene too. In fact, commercially available bi- and trilayer samples were used to derive layer dependence of charge-exchange and ion-induced electron emission while keeping the semi-metal character of graphene.

5.1   Charge Exchange

As commercially available multilayer graphene targets always contain transfer residuals and contaminations, heat treatment and laser cleaning was inevitable for all samples presented in the following. Further, bi- and trilayer graphene samples are supported by a QF support without additional gold coverage enabling ions to pass the QF at sufficient high ion energies. Therefore, TOF-filtering of the received MCP position spectra was used to exclude falsifying of the extracted exit charge state distribution. Again, as already shown for graphene, the exit charge state of an ion with an initial kinetic energy and charge state transmitted through two or three layers of graphene results in a Gaussian shaped distribution. Extracting the mean of the Gauss fit delivers the mean exit charge state and therefore the on average number of captured electron by the projectile within the layers.
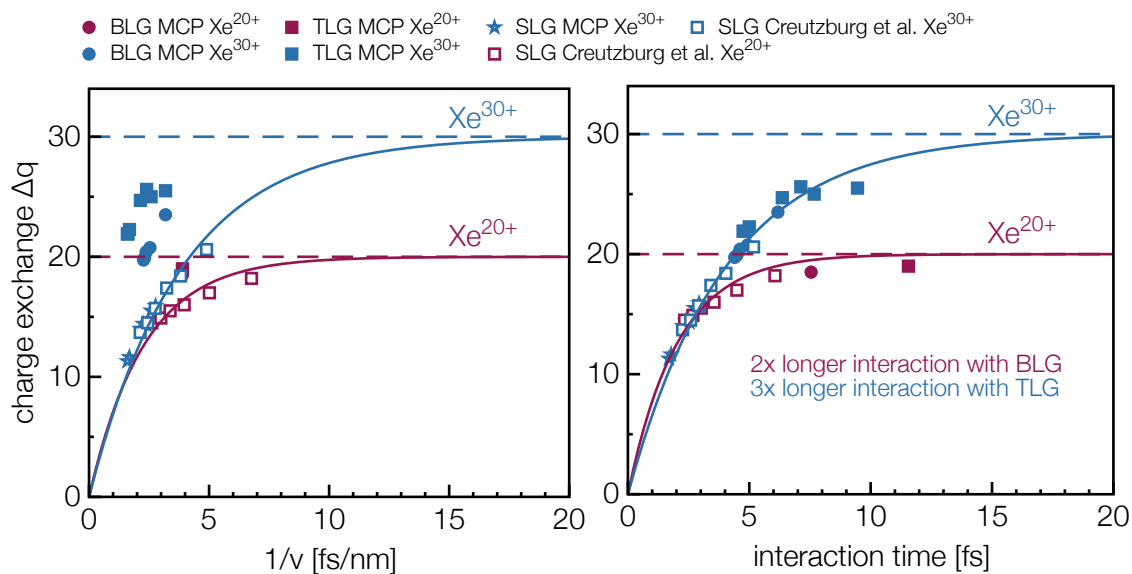
Figure 5.1: Charge exchange of Xe^{20+} and Xe^{30+} ions in mono-, bi-and trilayer graphene in dependence of the inverse ion velocity (left). Taking an increased interaction time for multiple layers due the target thickness into account results in a common charge exchange mechanism (right).

In contrast to only one layer of graphene, a broading in the scattering angle (+1° for 166 keV Xe^{34+}) after transmission through clean BLG graphene sample could be observed. This is assigned to the possibility of multi-scattering, suppressed in a monolayer but present once the number of layers is increased. For TLG, apparently, no further increase in the scattering angle compared to BLG is observed as this can be extracted from figure 3.18 in the master thesis of A. Niggas [90]. The evaluated exit charge states after the transmission through BLG and TLG

are compared in figure 5.1 to charge exchange in a monolayer. Electron capture and further stabilization seems to be more efficient in two layers and still increases for three layer samples when plotting the data versus the inverse ion velocity (left plot in figure 5.1) as performed in the last chapter. However, in regard of a an enhanced thickness of bi- and trilayer graphene in contrast to a monolayer, one has to take a certain increase in the interaction time with increasing number of layers into account. Therefore on the right in figure 5.1 the number of captured and stabilized electrons is plotted versus the interaction time τ according to equation 4.1, again with a charge state dependent effective thickness d_{eff} derived from TD-DFT calculations [40]. When τ is multiplied by a factor of two and three for BLG and TLG, respectively, the data points (full symbols) shift towards longer interaction times arriving at the same fitting curves applied for SLG for a specific incident charge state according to equation 4.2. This points towards a common neutralization mechanism for HAs, before termed as ICD, independent of the layer numbers for graphene. Thus, the amount of charge captured and stabilized is only determined by the ion's interaction time τ, i.e. the effective thickness of a target.

5.2   Electron Emission

Measuring the ion-induced electron emission from graphene samples for which no additional gold layer on the support was present, allows to directly compare emission yields from a monolayer graphene to a $\sim 20\,\text{nm}$ thick amorphous carbon film within one measurement. Only the projectile velocities have to be sufficient high for passing the carbon support. However, all transmitted ions neutralize within 20 nanometers which allows filtering of recorded electron emission by exit charge states. Results, presented in figure 5.2a, reveal an increased emission yield from carbon when only a single layer is present more electrons are emitted following from the interaction with graphene compared to its QF support. An increase with increasing charge state is reported for various initial ion kinetic energies. In case of SLG it might be possible for electrons to escape from both sides of the thin membrane and being registered at the PIPS detector. The QF allows for multiplication of electrons within the material, but the escape of such secondary electron is suppressed due to the target thickness. To investigate this assumption in more detail electron emission statistics were also analyzed for ion impact on BLG and TLG in order to build up a carbon solid layer by layer.

Figure 5.2b and c reveal a comparable high electron emission yield for bi- and trilayer graphene, respectively. Further, electron emission yields from QF recorded within one measurement are added. Within the error bars, there is no obvious difference in the number of electrons emitted from a BLG, TLG or an amorphous 20 nm thick carbon film to be extracted. As the energy loss of
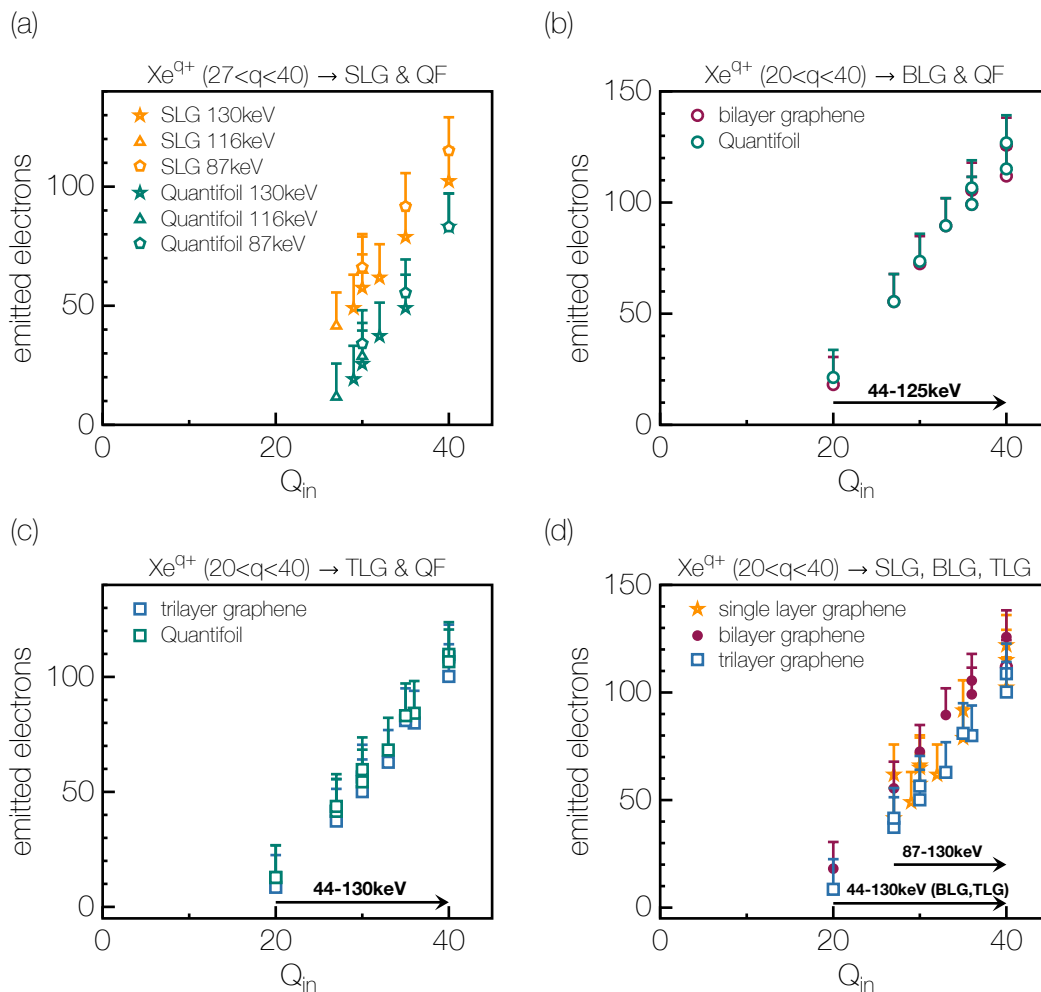
Figure 5.2: Electron emission yield dependence on the incident charge state from QF target support compared to electron emission following from (a) SLG, (b) BLG and (c) TLG. Within the experimental error bars, ion-induced electron emission yield from graphene is independent from the number of layers (d).

ions in two and three layers of graphene is approaching the energy loss in QF support film, also their recorded TOF peaks shift towards higher time of flights making the TOF-filtering process more difficult. The comparison of TOF peaks recorded for the interaction with only a single layer in contrast to three layers of graphene is shown in figure 5.3. While the TOFs, used as a filter to extract the ion-induced electron emission, are clearly separable for SLG and QF (with possibly SLG on top), they move closer together for TLG samples. Therefore, electrons emitted from QF and shown in figure 5.2b and c might in fact also follow to some extend from ion impact on BLG and TLG as their TOF peaks partly overlap with the QF TOF peaks. Thus, also the measured

electron emission yields for BLG, TLG and QF are in agreement. When comparing SLG, BLG and TLG directly, as this is shown in figure 5.2d, we conclude that electron emission yields for all samples are the same within the experimental error bars.
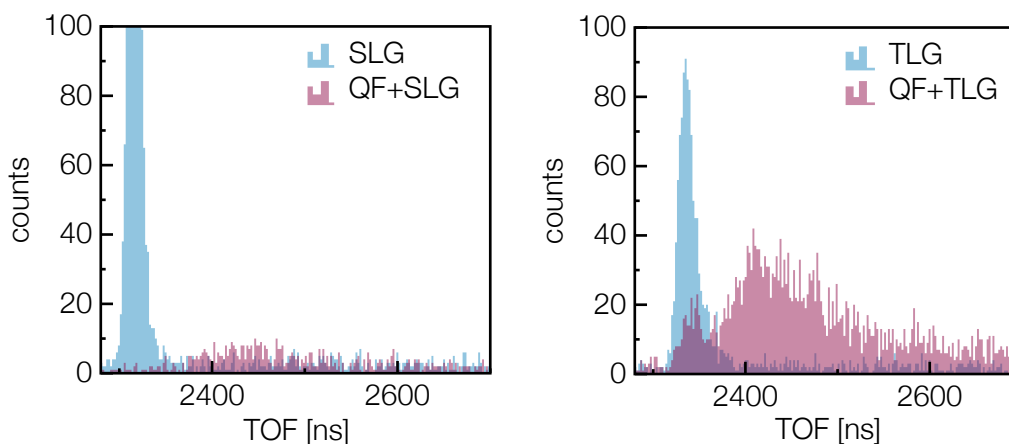
Figure 5.3: Measured TOF for ions transmitted through freestanding SLG and SLG on top of QF support (left). TOFs for ions passing TLG shift towards higher values as the ion's energy loss increases (right).

5.3 Discussion - Everything happens within First Layer

Already the results on charge-exchange in BLG and TLG in the previous section 5.1 reveal a common HA deexcitation behaviour independent of the target layer thickness. It is apparent to assume, that also for two or three layers of graphene, ICD is responsible for the observed ultra-fast neutralization as interatomic distances do not change for BLG and TLG. Thus, the emission of a large number of low-energy electrons into vacuum follows consequently as carrier mobilities are comparable high to those measured in graphene at room temperature. After performed cleaning procedure high resolution TEM images performed at USTEM in collaboration with the Faculty of Technical Chemistry at TU Wien, reveal a clustering of contaminations and PMMA residuals into thick pockets preventing ions from transmission (compare figure 5.4). Clean mono-, bi- and trilayer regions are observed in the microscopic image (A), along with hydrocarbon adsorbates - arising from sample transfer into atmosphere after irradiation - having equivalent thicknesses of about 4-10 monolayers (B) up to 15 (C). Heavy residual contaminations after heat treatment are possibly the result of dirt clustering together and reaching thicknesses of 20-140 equivalent monolayers (D). Later performed energy-dispersive x-ray spectroscopy (EDX) indicates that the majority of the latter comprises of gold. However, as the

QF support is covered with gold, the received Au EDX signal might also originate from scattering of the electron beam on QF-hole edges resulting in an enhanced peak. Therefore, it has to be noted here that the nature of the observed thick pockets is not clear yet but their heavy mass prevents ions from transmission. Further, as already discussed for graphene, no ion-induced pores in the membrane could be observed after irradiation leading to the conclusion that also for BLG and TLG charge is resupplied promptly enough to prevent Coulomb explosion.
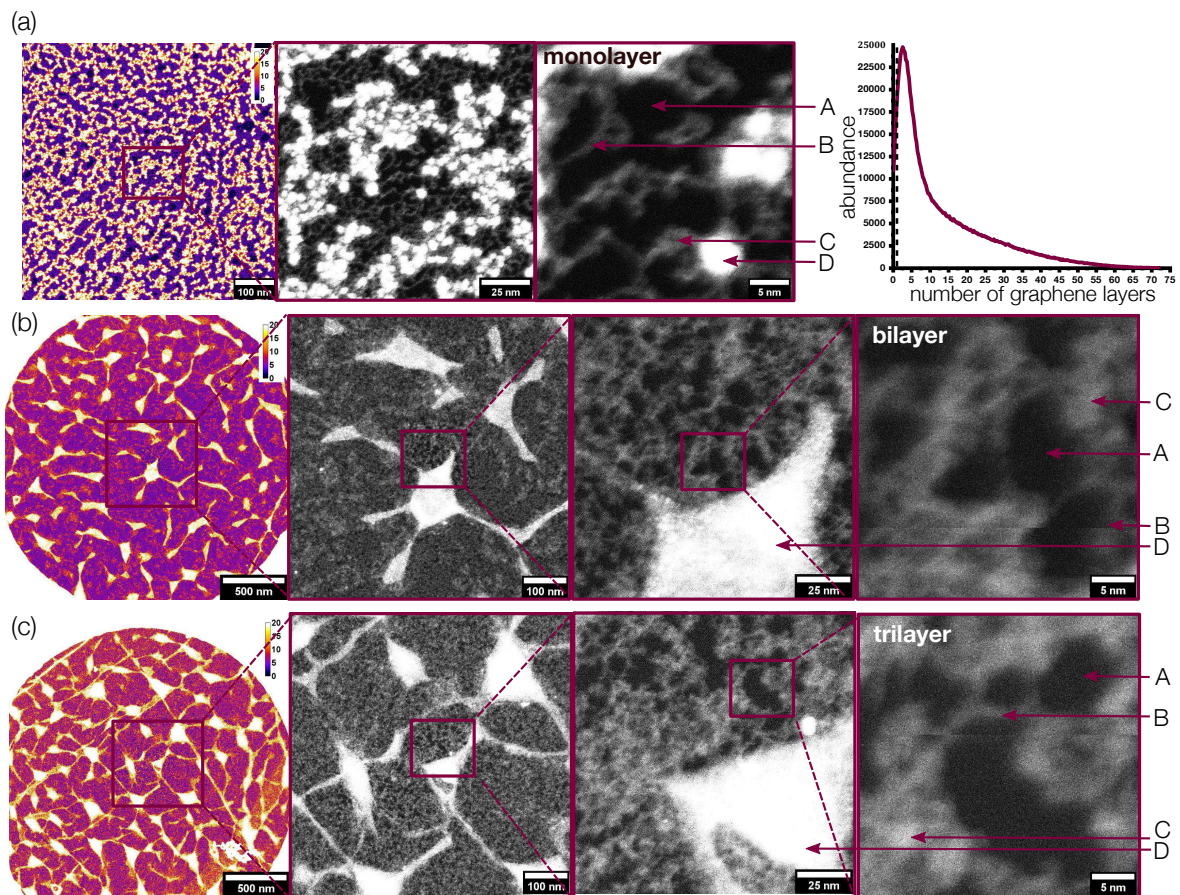
Figure 5.4: High resolution STEM images of (a) SLG, (b) BLG and (c) TLG with marked regions of A - pristine mono-, bi- or trilayer grapene, B- contamination regimes with thicknesses of up to 10 monolayers and C - up to 15. Regions marked with D show thick heavy residuals.

In the past a number of results on ion-induced electron emission from solid surfaces were published [17, 18, 71, 112, 146] which enables to test the assumption that PE mainly originates from the very first layer. It seems apparent to compare data on semi-metal graphene with results from metal surfaces or even HOPG, which is in fact the stacking of individual graphene layers until arriving at a highly oriented graphite solid. In figure 5.5 comparison between the total

electron emission yields from a cleaned and a still contaminated graphene layer is replotted, already presented in the previous chapter. Additionally, total electron emission yields following from Xe^{q+} on a clean HOPG surface [112] are presented as black data points. For high charge states they seem to very well agree with results on clean monolayer samples while reaching a common saturation with contaminated SLG towards lower charge states. Further, electron emission yield from slow Xe^{q+} impact on automatically cleaned Au [17] are added in the plot as red hexagons. Apparently, the data exactly match with contaminated graphene, i.e. multiple layers. Note, that ion velocities included from past studies deviate from current measurements but are, however, comparable close to each other to not lead to any change in the PE yield due to kinetic driven processes.
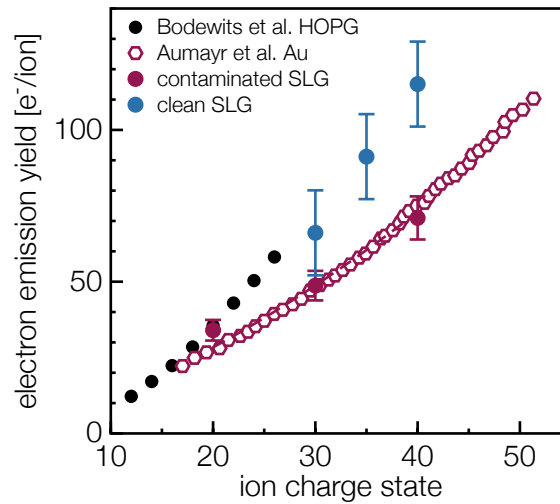
Figure 5.5: Total electron emission yield for 3.6×10^5 m/s Xe^{q+} impact on slightly contaminated (red full circles) and cleaned SLG (blue full circles). Data following from 3.2×10^5 m/s Xe^{q+} Xe^{q+} bombardment of clean HOPG [112] and from 5×10^5 m/s Xe^{q+} of an automatically clean Au surface [17] are added in black and red, respectively.

The deviation of electron emission yields from contaminated and cleaned SLG samples was already discussed in the previous chapter. The presence of contaminations on the sample lead to an increase in the ion's energy loss when transmitted through the target with a further impact on the number of emitted electrons from the surface. The broader peak with higher time-of-flights for ion transmission before performing a cleaning procedure can be seen in figure 5.6, adapted from A. Niggas master thesis [90]. Hydrocarbons on the surface influence the electrons in their emission from the surface and hence a smaller electron emission yield is measured. However, when cleaning the surface properly, the emission yield of a SLG, BLG and also TLG agree with the electron emission yield measured for ion interaction with HOPG. Hence, the ion-

induced PE yield from a certain material is independent of its number of layers. These findings therefor further support the idea of ICD to occur in close proximity to the surface likely to be present in front of a HOPG but any other metal surface for close impact parameters.
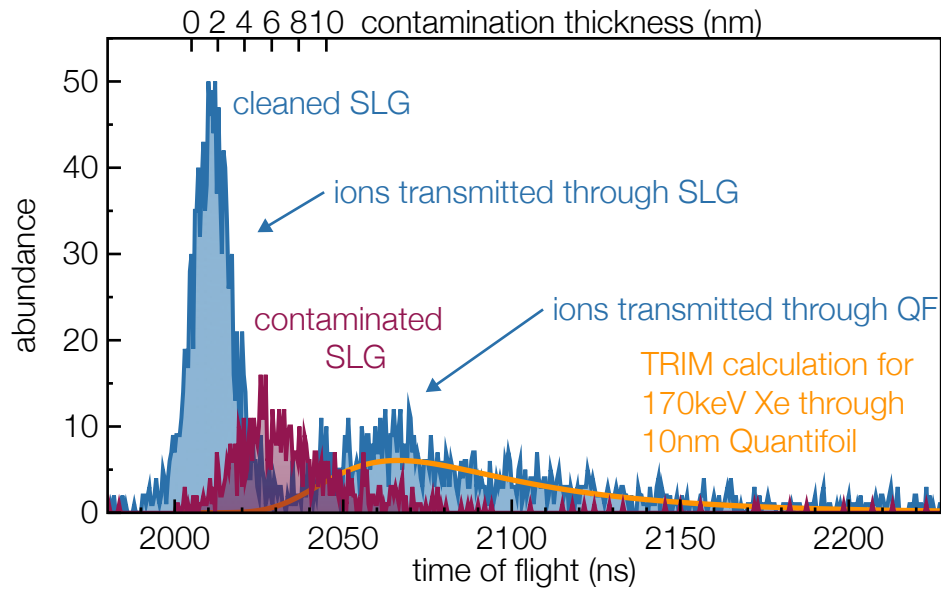
Figure 5.6: Measured TOFs for ions transmitted through contaminated and clean SLG targets and their QF support. Further the energy loss in 10 nm thick QF was simulated with TRIM (TRansport of Tons in Matter) and added to the plot. Figure adapted from [90].

6

Molybdenum Disulfide

After assigning HA deexcitation in front of a metal surface to ICD proceeding within femtoseconds without leaving any observable damage in the membrane, as a next logical step the response of 2D materials with other properties was tested. Transition metal dichalcogenides (TMDs) with their formula MX_2 (M representing the metal and X the chalcogene) form nowadays the basis of modern nano-electronics industry as their electronic properties range from insulating and semiconducting to metallic and semi-metallic. Monolayers show a hexagonal structure consisting of three stacked layers (X-M-X). Their different electronic characteristics follow from transition metal electrons filling nonbonding d bands [30]. In contrast to graphene for example, a single layer of MoS_2 forms a tunable direct band-gap, a property essential for many applications such as next-generation field-effect transistors. Charge exchange of HCIs in MoS_2 is discussed in a recent publication [45] and parts of these results are presented in the following chapter.

6.1   Properties

Two-dimensional MoS_2, a member of the TMD family, offers ideal requirements for devices such as 2D photodetectors [147] and single layer transistors [148]. The reason lies within its nature

as a thin transparent semiconductor and the nowadays possibility for large-scale fabrication of monolayers. Dissimilar stacking of MoS_2 sub-lattices can result in a hexagonal structure (2H) from top view comparable to the one of graphene except for consisting of only one sort of atoms. In fact, 2H-MoS_2 consists of three atomic layers, each Mo atom sandwiched within two S atoms with an out of plane S-S distance of 3.2Å [149]. While bulk 2H-MoS_2 is an indirect band gap semiconductor, the band-gap increases with decreasing number of layer resulting in monolayer MoS_2 with a direct band gap at 1.9 eV. A direct band gap - a property which graphene is lacking - is of special interest for applications in optics and optoelectronics. Further, the size-able band gap allows current switching on/off ratios above 10^8 at room temperature in transistors with carrier mobilities of $\mu \approx 200\,cm^2V^{-1}s^{-1}$, still lower than in graphene but comparable to thin silicon films and nanoribbons [148]. In various applications in which a thin and transparent semiconductor is required, 2D MoS_2 is often treated as a complement to graphene [150].

6.2 Charge Exchange

Samples for studying the charge exchange in a single layer MoS_2 were fabricated by CVD on a substrate and only the monolayer was further transferred onto a QF supported TEM grid by various groups (University of Vienna, Friedrich Schiller University Jena and University of Duisburg-Essen) for comparison. As cleaning procedures turned out to be inevitable for monolayer films, thus also MoS_2 samples were annealed up to 400°C, laser treated and further kept at constant temperature of 180°C during measurements.

In contrast to slow HCl transmission through graphene, charge states of ions passing a monolayer MoS_2 follow a bimodal distribution rather than a Gaussian. Ions capturing a low number of electrons and thus remaining highly charged, are scattered under small angles <0.2° (same angular distribution as the primary ion beam), while a second distribution indicates scattering into broader angles as well as capturing 4-5 times more electrons. An example for 87 keV Xe^{30+} ions passing a single layer of MoS_2 and being recorded at the DLD is shown in figure 6.1. The spectrum is TOF filtered using as allowed condition only TOFs between 2790-2911 ns. By fitting a Gauss into each of the charge state distributions, an upper mean exit charge state of 26+ and a lower mean exit charge state of 11+ can be extracted from this particular spectrum. A similar behavior for charge exchange was already observed for transmission of slow HCIs through 1 nm thick CNMs [151]. In the case of CNMs, the upper charge state distribution was concluded to follow from ion transmission through less dense areas or intrinsic holes while high charge exchange is observed for collisions with small impact parameters in the amorphous carbon target.
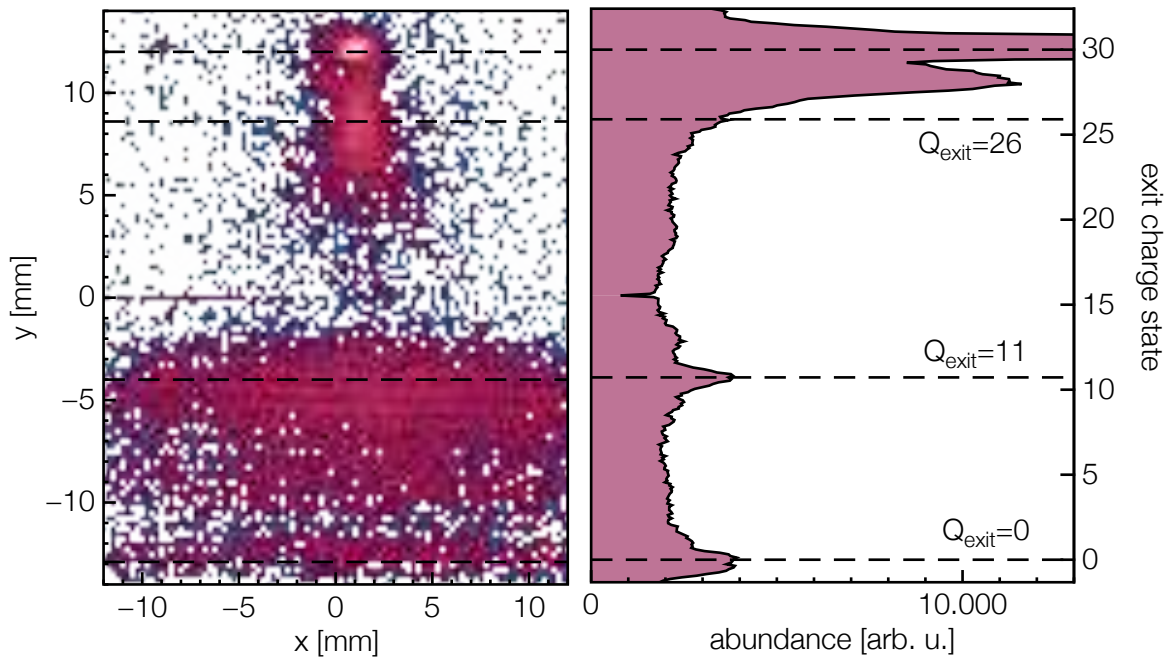
Figure 6.1: Two distinct exit charge state distributions are observed for 87 keV Xe^{30+} transmission through monolayer MoS_2. 2D MCP position spectrum after TOF filtering (left) and translation into exit charge states (right).
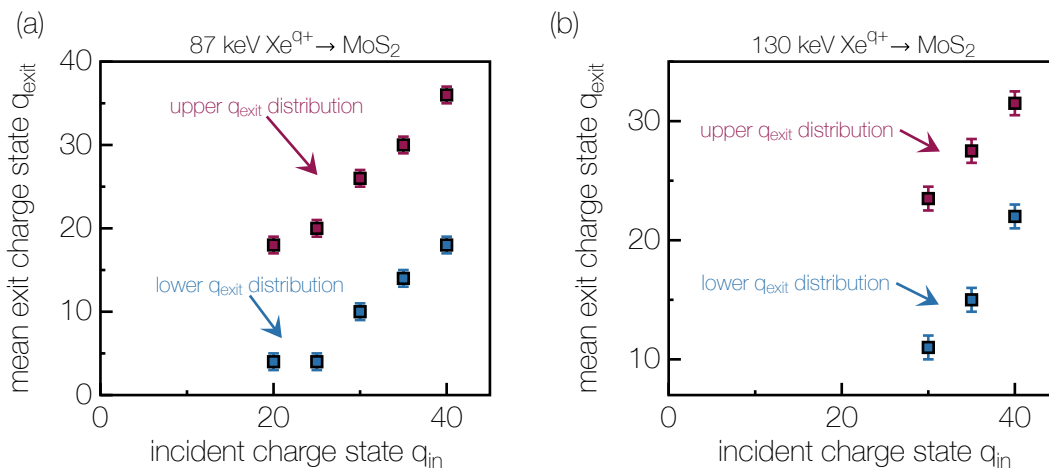
Figure 6.2: Comparison of charge exchange for upper and lower exit charge state distribution in case of (a) 87keV and (b) 130 keV Xe ions transmitted through monolayer MoS_2.

Tthe mean exit charge states for the upper and the lower distribution are compared in figure 6.2 for 87 keV (a) and 130 keV (b) Xe ions and show strong differences. While the exit charge state

increases linearly with the incident ion charge state above a certain threshold of $q_{in} = 20+$, for both initial kinetic energies, the ratio between upper and lower mean exit charge state remains constant.
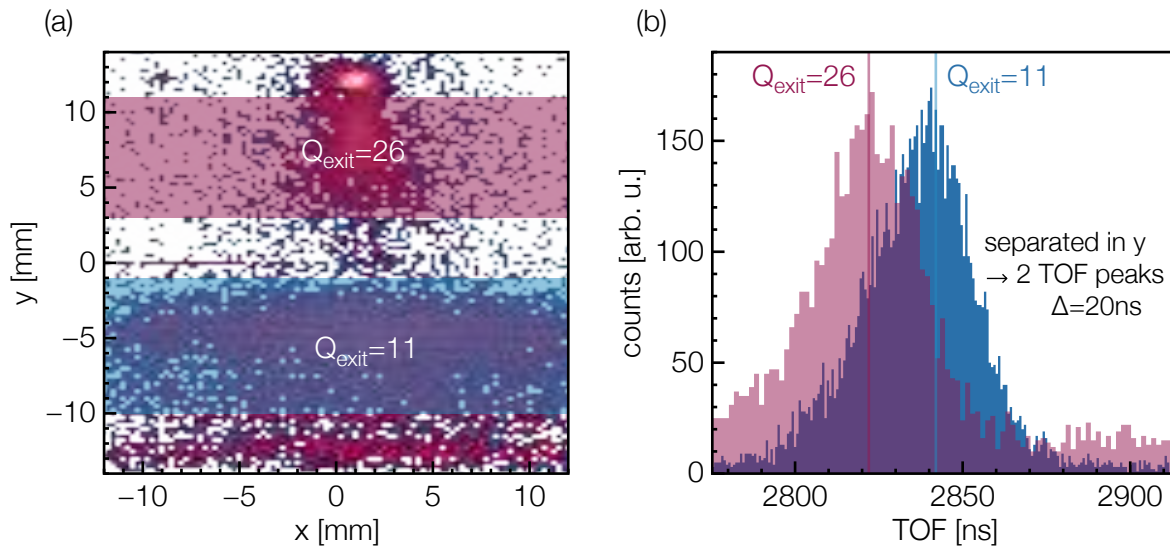
Figure 6.3: (a) Same MCP spectrum as in figure 6.1 with colored ranges marking two distinct exit charge state regimes used as condition for plotting TOF in (b).

Furthermore, a clear difference in the energy loss can be seen when comparing TOFs for ions filtered by their exit charge states. A difference of 20 ns, depict in figure 6.3(b), is observed for ions in high exit charge states compared to ions arriving in the low exit charge state distribution. When using the TOF of the upper distribution as a reference, the TOF for ions undergoing high charge exchange corresponds to an additional energy loss of 1 keV within the MoS_2 mono-layer.

The efficient charge-exchange and the corresponding high kinetic energy loss observed for ions in low exit charge states is remarkably similar to the results observed for ion transmission through graphene. Outgoing charge states in the lower distribution are directly comparable to graphene. In figure 6.4 the mean number of captured and stabilized electrons in a single layer of MoS_2 is plotted versus the inverse ion velocity for Xe^{30+} and Xe^{35+}. Data points extracted from charge exchange measurements in clean pristine SLG, measured in Vienna and at the HZDR [45], and their fits according to equation 4.2 are added for comparison. Again, as this was already observed for multiple layers of graphene, slightly more electrons are stabilized after interaction with a single layer of MoS_2 than with SLG. However, when relating the x-axis to the actual interaction time of the ion with the material, charge exchange matches with the one for
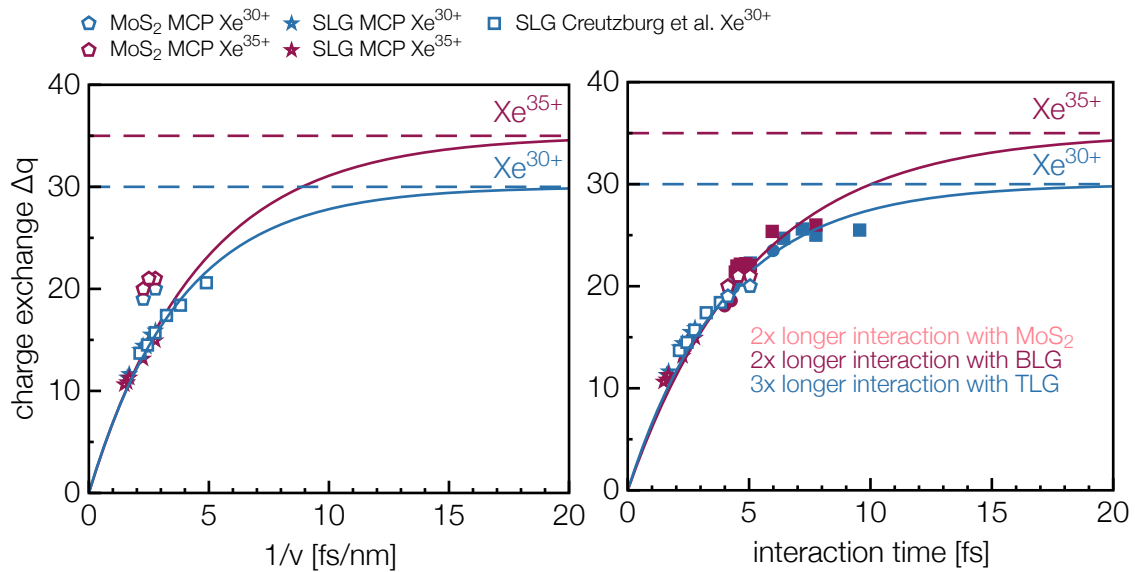
Figure 6.4: (a) Charge exchange of Xe^{30+} and Xe^{35+} ions in monolayer MoS$_2$ and clean SLG [45] in dependence of the inverse ion velocity (left). (b) Increasing the interaction time by a factor of two for transmission though MoS$_2$ both 2D materials show a comman neutralization behavior. For comparison data points for BLG (full circles) and TLG (full squares) are added (right).

ions interacting with SLG as this is depicted in figure 6.4 (right). To join MoS$_2$ data points with fits for SLG data, a twice as long interaction with the MoS$_2$ sheet has to be assumed. This is the same enhancement factor as earlier determined to match charge exchange in BLG with the monolayer results. Taking an interlayer distance of 0.34 nm for graphene into account and an out of plane S-S distance of 0.32 nm in MoS$_2$, the agreement for ion transmission times through BLG and MoS$_2$ seems reasonable as those parameter mainly determine the interaction time.

6.3 Electron Emission

A bimodal exit charge state distribution for HCI transmission through MoS$_2$ indicates differences in energy release for ions exiting the target in high and in low charge states. As ion-induced particle emission represents one possible channel for release of energy deposited into the target, electron number statistics are analyzed for high and low exit charge state distributions independently. TOF- and MCP-position-filtering allows to differentiate between them. Additional, the applied filters enable to extract the yield for the QF support for each measurement. As electron emission is comparable low from a single layer of MoS$_2$ in contrast to graphene, the

yield evaluation is more challenging. However, since QF is also present for SLG measurement, the evaluated electron emission yield can be used as a reference value. The number of emitted electrons for 87 keV (a) and 130 keV (b) Xe^{q+} bombardment are shown in figure 6.5 and compared with earlier discussed SLG measurements. Since both QF yields match reasonably well, the same collection efficiency for both 2D crystals can be assumed. While emitted electron numbers related to the upper and the lower ion exit charge states in MoS_2 agree within the error bars, strong differences are observed in the direct comparison to electron emission from its semi-metallic counterpart SLG.
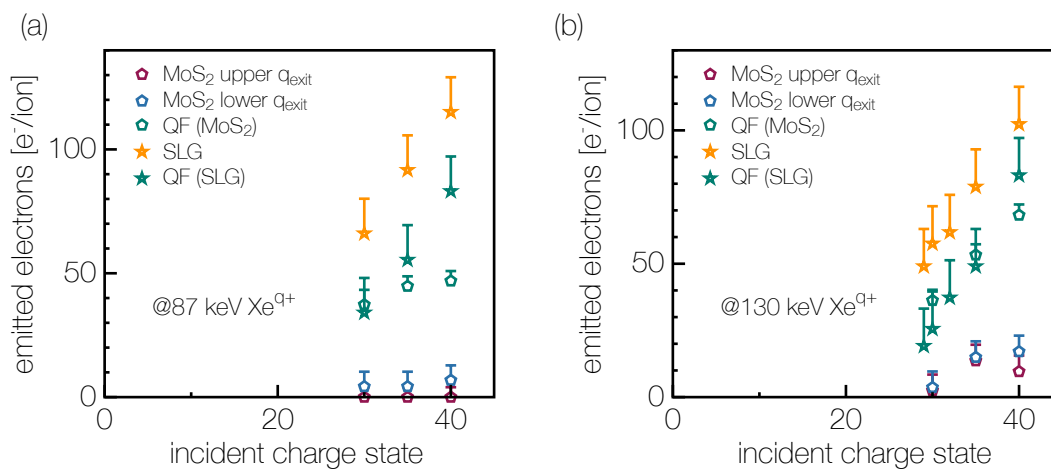
Figure 6.5: Ion-induced electron emission yields for upper and lower exit charge states following from transmision through MoS_2 for (a) 87keV (b) 130 keV Xenon ions. Data are compared to yields measured for the QF support and SLG.

For an incident charge state of 30+ this difference amounts to $61\,e^-$/ion and even increases for initially 40+ charged Xe up to $109\,e^-$/ion for 87 keV. In case of an initial kinetic energy of 130 keV these numbers add up to $44\,e^-$/ion and $85\,e^-$/ion for Xe^{30+} and Xe^{40+}, respectively. Conclusively, a different channel for energy release and dissipation in a MoS_2 layer has to be active for HCI deexcitation in the semiconducting membrane.

6.4   Discussion - Energy Dissipation

When we assign the lower exit charge state distribution to charge exchange via ICD as this was assumed for SLG before, still the origin for ions in high charge states after transmission remains puzzling. As a similar behavior was observed for CNMs in earlier studies [151] a similar

explanation might be put forward by assuming a common cause for the upper charge state distribution.

For CNMs such ions were assigned to result from projectiles passing less dense areas (e.g. small, intrinsic holes) in the material allowing only small fractions of electrons to be captured and even less to be stabilized due to the present large impact parameters. Along the way to the detector AI of the projectile follows and ions consequently arrive again in a high charge state.

When one has a look on the structure of MoS_2 from the top it becomes apparent that, in principle, larger impact parameters compared to graphene are possible for MoS_2 since the hexagon is considerably larger. A comparison in figure 6.6 reveals a C-C bond length of only 0.142 nm in contrast to an in plane S-S atom distance for 2H MoS_2 of 0.241 nm. Therefore ions might pass the hexagon without triggering charge exchange via ICD, as rates scale with interatomic distances $\propto 1/R^6$. Such projectiles capture electrons resonantly into high-n Rydberg states and the consequently formed HA decays mainly via Auger processes on the way to the detector. In figure 6.6(b) such large impact parameter regimes for ion transmission are depicted in blue, while ions passing the yellow marked area deexcite via ICD and arrive in lower exit charge states.

However, looking from a more macroscopic view on the structure of the used MoS_2 samples, ruptures of the monolayer sheet as a result of previous impact events as well as a number of intrinsic defects and nano-pores become visible. These are found especially along grain boundaries, commonly known for CVD grown MoS_2 samples, and occur already within the production process [152]. Ion scattering and charge transfer along such edges might be a second possible explanation for the observed high exit charge state distribution in monolayer MoS_2. Pores and intrinsic defects lead to large impact parameters with low probability of not being sufficient small to trigger ICD. An atomic resolution annular dark field image of a typical intrinsic disulfur vacancy in MoS_2 is presented in figure 6.6(c) [152].

An additional reason to attribute the occurrence of the upper charge state distribution to ions passing pores and intrinsic defects is given by the fact that the amount of ions observed in such high exit charge states increases with the applied ion fluence [45] once sufficient high initial charge states are chosen. It was recently shown that slow HCI irradiation of freestanding monolayer MoS_2 results in ion-induced pores in the membrane with radii in the range of 0.3-3 nm [153]. Perforation of the sample within transmission studies leads to additional nano-pores and therefore more possibilities for ions to scatter in forward direction. Again, such ions arrive in high charge states and therefore account to the observed upper charge state distribution.
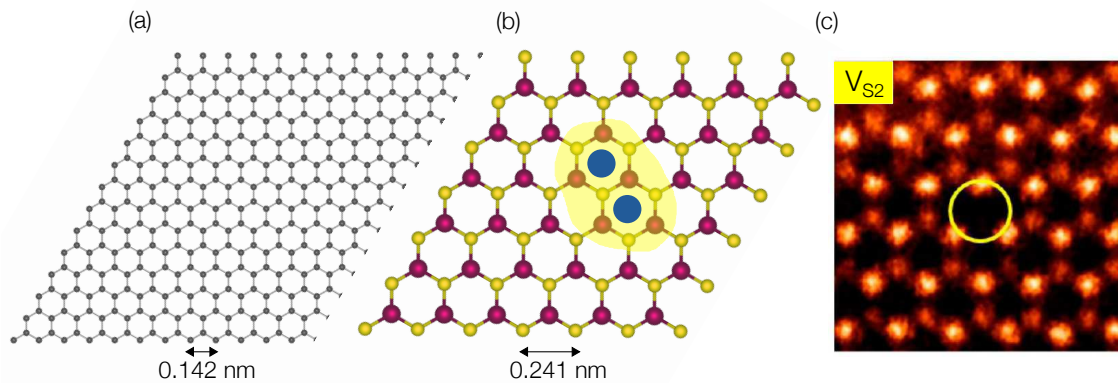
Figure 6.6: Different impact parameters for ion collision with target atoms in SLG (a) and MoS$_2$ (b) for which ion transmission through hexagon might be possible without HA deexcitation via ICD marked within the light yellow area as blue circles. (c) Intrinsic disulfur vacancy in CVD grown MoS$_2$ [152]

In [153] the deposition of the whole initial potential energy (4.6 keV $\leq$ E$_{pot}$ $\leq$ 38.5 keV for q$_{in}$ = 20+ up to q$_{in}$ = 40+) was assumed as no detailed knowledge of the outgoing ion charge state could be provided at that point. The amount of removed atoms per keV was estimated from STEM images and showed an increase from 7 atoms/keV to 20 atoms/keV for q$_{in}$ = 20+ to q$_{in}$ = 40+, respectively. Hence, a charge state dependent energy deposition was concluded. According to equation 4.8 the deposited energy can be estimated from the mean exit charge state for both distinct distributions (figure 6.7(a)) when assuming a negligible amount of emitted electrons as shown in figure 6.7(b). While the deposited potential energy reaches a saturation at about 10 keV for the upper distribution, it strongly increases for the lower distribution. Therefore we conclude that ions exiting in high charge states cannot contribute to the pore formation in MoS$_2$ as their total potential energy release is not high enough. However, for ions arriving in low charge states sufficient energy is deposited into the target to result in perforation of the monolayer. The estimation of removed atoms/keV concluded by Kozubek et al. [153] is well in agreement with these findings.

As already concluded for SLG the release of energy via electron emission is a very minor effect and is even less pronounced for freestanding monolayer MoS$_2$. For 87 keV Xe^{40+} bombardment, 91% (35.1 keV) for the lower and 28% (10.7 keV) for the upper exit charge state distribution of initial 38.5 keV potential energy are deposited into the system. As shown in recent studies, the further dissipation of such large locally deposited amounts of energy leads for the semiconducting MoS$_2$ to pores in the nanometer range while in contrast to graphene the membrane stays intact [153]. Perforation of monolayer MoS$_2$ using 180 keV Xe^{40+} is depicted in figure 6.8.
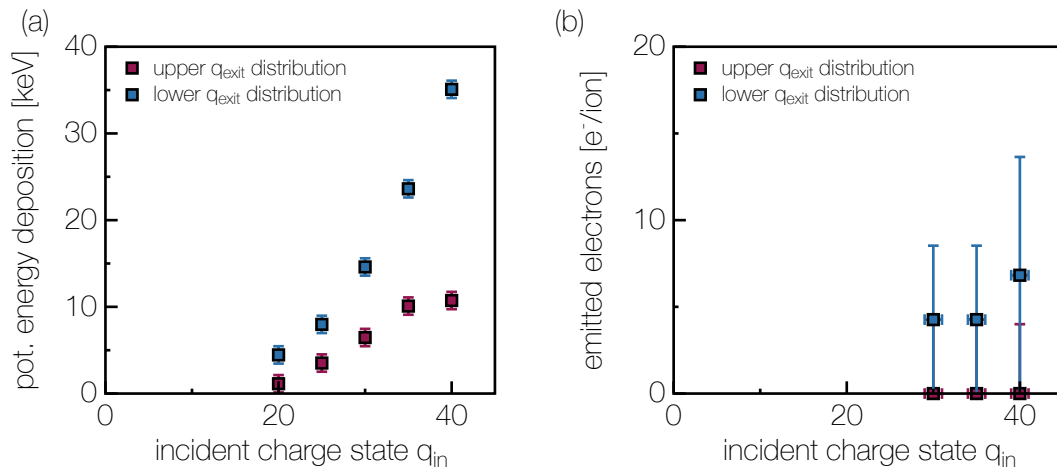
Figure 6.7: (a) Potential energy deposition for upper and lower exit charge state distribution in freestanding MoS_2 after 87 keV Xe^{q+} transmission. (b) Corresponding ion-induced electron emission for (a).

From this we can clearly conclude that the electronic properties of a 2D crystal very well define the ability for nano-structuring of these surface-only materials. In general, phenomena for which dissipation of energy within the plane of the target is required are strongly ruled by its electronic nature. Such processes occur slightly retarded to the actual charge capture as they depend on the electronic response. Since the number of electrons is reduced by at least a factor of 10 for ions penetrating a monolayer MoS_2 in contrast to SLG, also ion-induced electron emission can be seen as such a process occurring retarded from the actual moment of charge removal by the ion. Once the membrane gets polarized and charges are not resupplied promptly enough, electrons in the MoS_2 layer are hindered from escaping the surface.
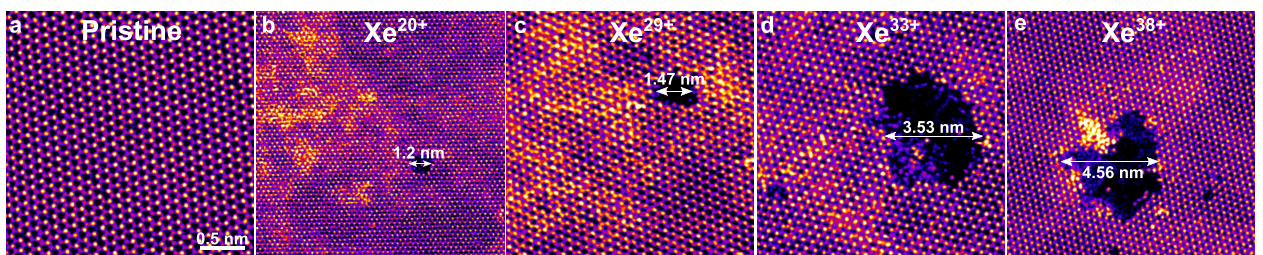
Figure 6.8: STEM images of pristine MoS_2 (a) and after irradiation with 180 keV Xe^{20+} (b), Xe^{29+} (c), Xe^{33+} (d) and Xe^{38+} (e) ions. Images taken from [153].

Further, the bimodal character of ion charge states after transmission through a 2D membrane is founded in the materials's structure. While for CNMs less dense packed areas allow ion transmission without interatomic charge transfer, in case of MoS_2, for example, intrinsic defects and in general larger lattice parameters enable such phenomena. The continuous irradiation with

slow HCIs results in pore formation which lead to additional available collision events with larger impact parameters for transmitting ions. For close impact parameters, however, a common nature of charge exchange, can be assumed once the extension in the effective thickness of the material is taken into account rather independent of the actual electronic band structure of the target material.

7

Van der Waals Heterostructures
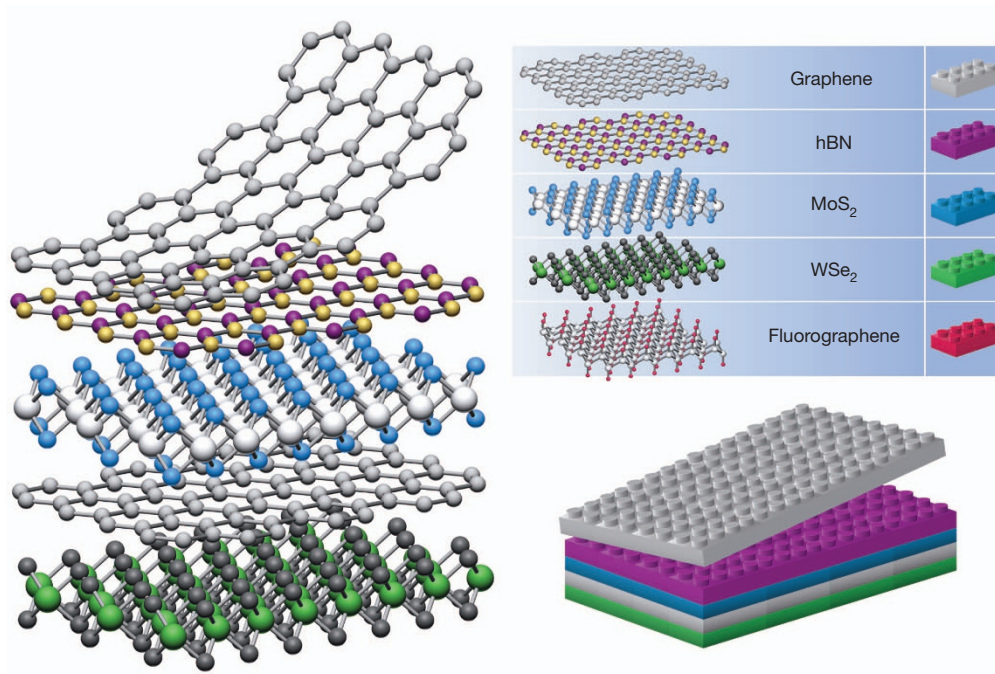
Figure 7.1: Building van-der-Waals heterostructures by stacking monolayer crystals in the desired order like Lego blocks. Taken from [101].

Lowering the thickness of a solid down to one or two dimensions has revealed exceptional properties not present in the 3D version of most materials. The fast growth of studies on 2D crystals due to industrial request for embedding them into a broad range of applications in future, is currently opening a new field of material synthesis and research. Stacking of different 2D materials layer by layer in a chosen sequence enables the fabrication of new artificial materials with each layer acting simultaneously as a bulk and the interface. Weak van-der-Waals-like forces hold the stack together, while strong covalent bonds within the plane guarantee the stability of the 2D crystals. As the family of 2D materials is rapidly growing since the first isolation of graphene, also the building of such van-der-Waals heterostructures by stacking 2D crystals like Lego blocks becomes nowadays a new playground for scientists [101] and promising for various technological applications.

Assembly techniques for large-scale fabrication of such heterostructures range from direct layer by layer mechanical stacking to "the pick-and-lift" method in which one 2D crystal is brought into close contact with another until van-der-Waals forces lift the latter up. Surprisingly, interfaces in such heterostructures can be free of any contaminations up to a $10\,\mu\text{m}$-scale [154]. The reason lies within the large affinity between certain 2D crystals. If it becomes larger than the affinity of one layer to the surrounding contamination, the latter is pushed into μm sized pockets resulting in large clean areas. Further, growth via van-der-Waals epitaxy based on processes such as CVD [155, 156] or molecular beam epitaxy [157] present additional fabrication methods scientists apply to facilitate scalable 2D heterostructures [30].

As the "white-graphene" insulating hexagonal boron nitride (hBN) has proven itself as an ideal substrate for high-quality graphene devices [158], pioneering work was accomplished when encapsulating graphene within thin hBN crystals for the first time. The protection of the graphene layer in this way led to a further improvement in the quality of such possible electronics especially under ambient conditions [159]. An evolutionary step was achieved when creating the first field effect transistor (FET) based on a vertical graphene heterostructure. Few layer thick 2D insulators (hBN) or semiconductors (MoS_2 or tungsten disulfide (WS_2)) creating tunnel barriers while graphene serves as an electrode in these new-generation transistors [160]. Also, the combination of the direct band gap material monolayer MoS_2 and the conductivity of graphene is used for building memory cells based on heterostructures [161]. As all these devices rely on components only a few layers thick, they are highly flexible and therefore suitable for transparent electronics.

Further, specific heterostructures consisting of semiconducting TMDs such as MoS_2 and SLG show high applicability in optoelectronics [162]. Creation of efficient phototransistors are simply based on the high carrier mobility in graphene and the high light absorption in MoS_2 due to

its controllable band gap (sensitive to number of layers) [163]. For photovoltaic devices the light-sensitive TMD is sandwiched between two graphene electrodes [164].

As charge exchange and energy dissipation within monolayer graphene and MoS_2 was investigated independently in the previous chapters, a van-der-Waals heterostructure consisting of these two 2D crystals was chosen with the aim of a conclusive over-all picture of charge exchange and energy deposition within a monolayer. CVD grown MoS_2 was transferred on commercially available SLG supported by a QF on top of a TEM grid [125] at the University of Vienna by H. Inani and M. Tripathi in the group of J. Kotakoski. There, the samples were checked with high-resolution STEM before and after ion irradiation. The following results are currently prepared for publication [165].

7.1 Charge Exchange

As thermal treatment might influence the stability of the hetereostructure no annealing or laser treatment was applied for MoS_2-SLG stacked samples used for ion irradiation. However, after preparation at the University of Vienna, efforts were made to keep the surfaces of the heterostructures as clean as possible by short-time storage in a desiccator before assembling in the experimental chamber under UHV conditions.

Exit charge states of HCIs after transmission through the heterostructure sample in two configurations were analyzed. First, the target was positioned in a way that the ion beam first faces the SLG before entering the MoS_2 layer. As an example, the MCP 2D position spectrum for $166\,keV$ Xe^{38+} ions is shown in figure 7.2(left) and its further conversion into exit charge states (right) according to equation 3.4.

As expected, the spectrum reflects the combined version of exit charge states following from clean SLG (lower exit charge states ($Q_{exit} = 10$)), MoS_2 (lower $Q_{exit} = 10$ and upper charge state distribution $Q_{exit} = 32$) and QF (neutrals). While the upper charge state distribution ($Q_{exit} = 32$) results possibly from areas in which only MoS_2 is present (such regimes were also observed in STEM images), the lower charge state distribution indicates the presence of more than only one layer as the charge capture and stabilization is enhanced.

Further, the y-positions are used as a filter for extracting individual TOF-peaks for ions transmitted through different regimes in the sample, as depicted in figure 7.3. Besides the TOF-peak of ions traversing the QF support (yellow), only one (slightly broadened) TOF-peak is visible as a result of the interaction with the stacked SLG-MoS_2-layers (green). Energy losses in SLG-
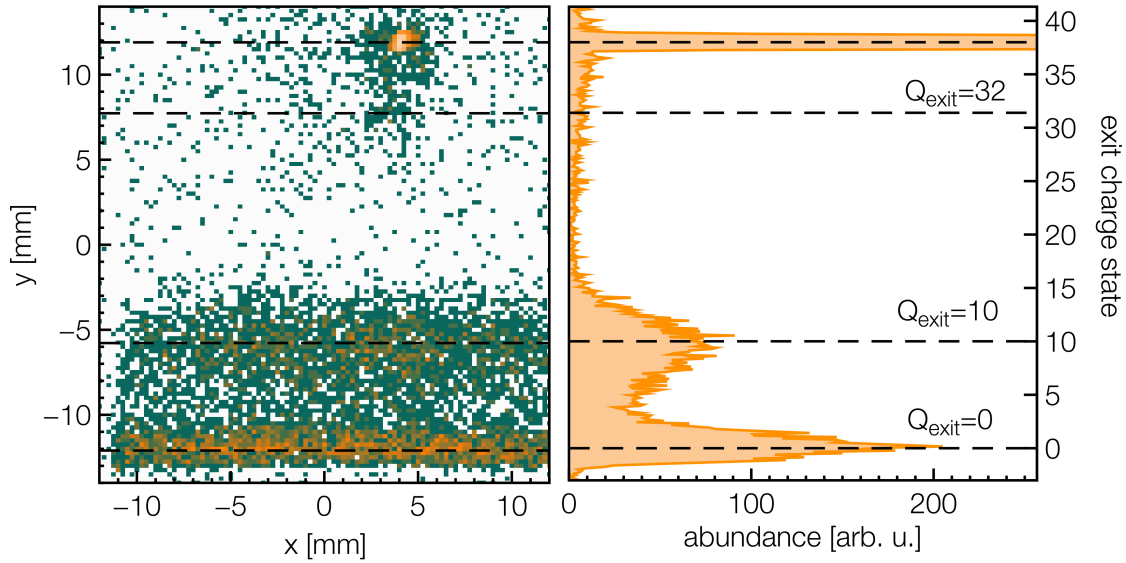
Figure 7.2: 166 keV Xe^{38+} ion transmission through SLG-MoS$_2$-stack: 2D position spectrum recorded at the MCP detector (left) and the following conversion into exit charge states (right).

and MoS$_2$-only regimes are so close to losses in the heterostructure that the TOF resolution, i.e. energy resolution of the detector, is not sufficiently high enough to show individual peaks. Hence, only one peak representing all regimes is visible in the spectrum.

Rotating the sample by 180° and hence forcing ion beam transmission first through MoS$_2$ before passing SLG, delivers the 2D position spectrum shown in figure 7.4(left). Again, the recorded data are converted into exit charge states according to equation 3.4 (right). Even though the statistics is slightly worse than in the previous figure, nearly the same charge exchange is observed for this sample configuration. Neutral atoms exiting QF are visible in the spectrum as well as an exit charge state distribution with a mean charge state at about 10, as demonstrated before. However, the upper charge state distribution almost vanishes but this might be a consequence of the lacking statistic present in this spectrum.

Also, a filtered TOF spectrum corresponding to neutrals and ions in low exit charge states (marked in red and blue, respectively) are analyzed for the reversed MoS$_2$-SLG configuration (figure 7.5). Again, only one TOF-peak is observed as a consequence of ion interaction with the heterostructure 7.5(b).

When directly comparing the TOF spectra for the two different ion transmission scenarios, one observes a shift to higher flight times for ions passing first MoS$_2$ and then SLG, shown in blue

(a)

(b)
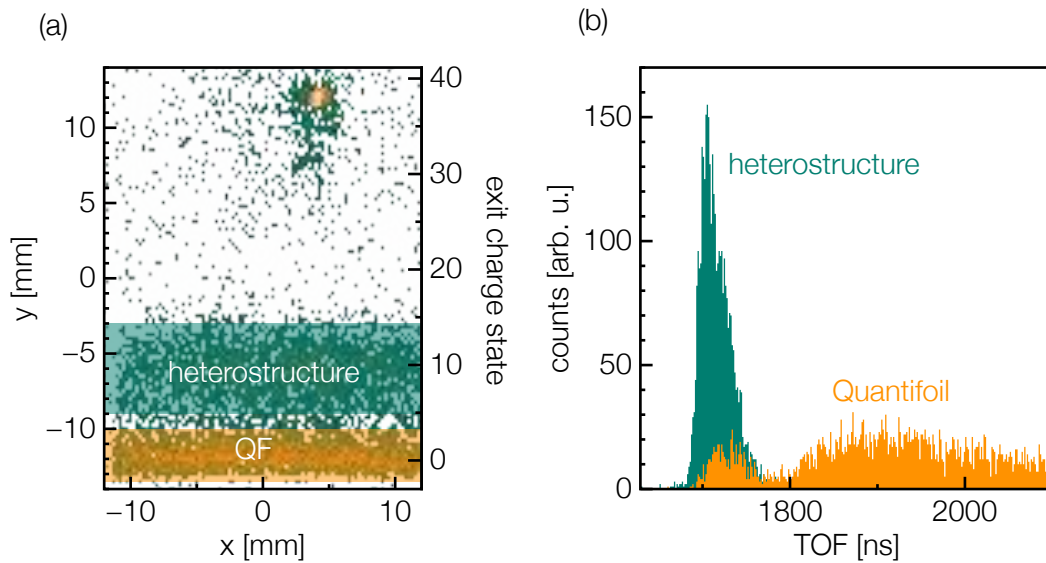
Figure 7.3: 166 keV Xe^{38+} ion transmission through SLG-MoS$_2$-stack: (a) 2D position spectrum recorded at the MCP detector and (b) Position-filtered TOF spectrum according to marked areas in (a).
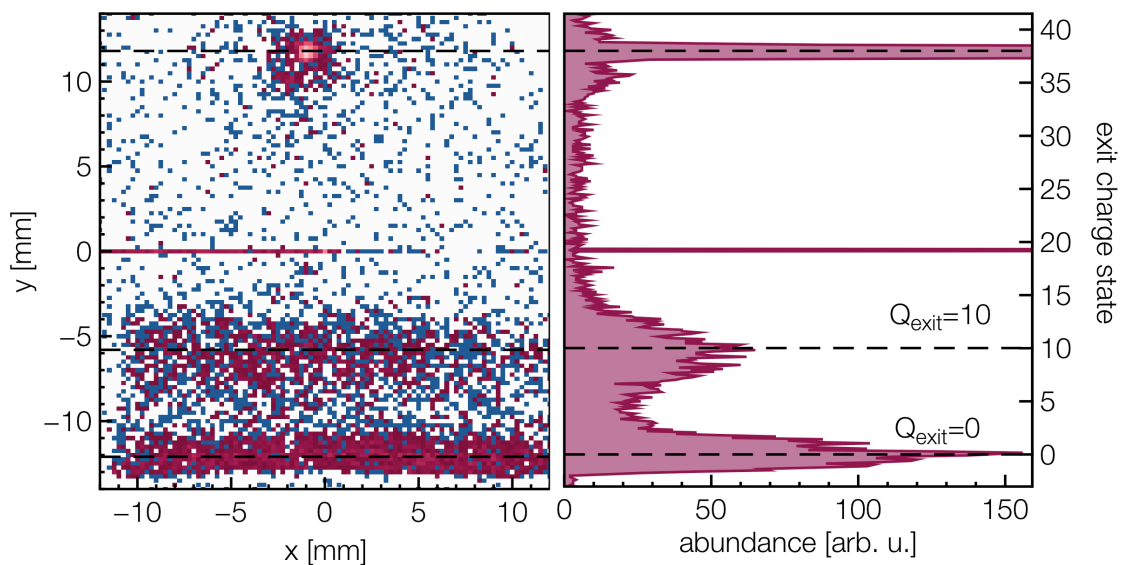
Figure 7.4: 166 keV Xe^{38+} ion transmission through reversed MoS$_2$-SLG-configuration: 2D position spectrum recorded at the MCP detector (left) and the following conversion into exit charge states (right). Note the narrow high intensity peak at a MCP position of y=0 mm results from electronic noise in the detector rather than from ion impact.
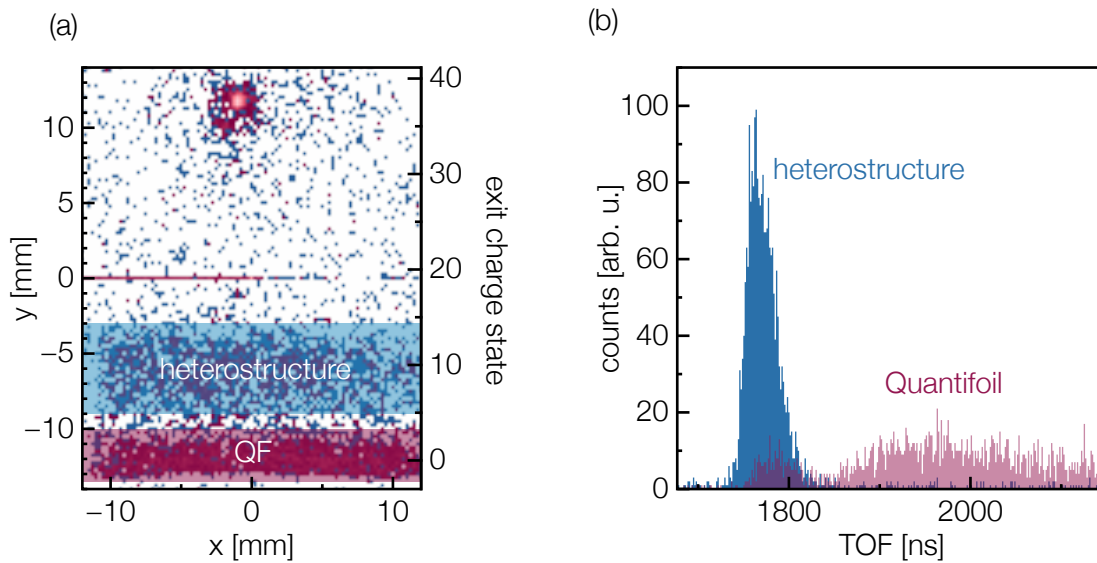
Figure 7.5: 166 keV Xe^{38+} ion transmission through reversed MoS$_2$-SLG-configuration: (a) 2D position spectrum recorded at the MCP detector and (b) Position-filtered TOF spectrum according to marked areas in (a).

in figure 7.6(a). However, as also the QF-TOF-peak shifts by the same value, we attribute this occurrence to the, in fact, longer distance such ions have to travel in the experimental chamber from the target until their impact at the MCP detector. Rotating the target holder by 180° results in an extension of the target-detector distance by 2.84 cm as the sample plane does not match the rotation axis. With a velocity of 4.98×10^5 m/s for 166 keV Xe^{38+} ions, this leads to an extension of 57 ns in their time of flight. When the recorded TOF spectrum for SLG-MoS$_2$ configuration (green) is shifted by this value, the TOF peaks for both sample configurations match in shape and time (figure 7.6(b)).

7.2 Perforation

As slow HCI irradiation above a certain potential energy threshold can lead to the formation of nano-pores, the 2D crystal stack was investigated in a high-resolution STEM at the University of Vienna (H. Inani) after the performed transmission measurements at TU Wien. Recently, it was reported that nano-pores are observed in freestanding MoS$_2$ monolayers when bombarding them with 180 keV Xe ions in high charge states [153]. Charge transport in the direct band gap semiconductor may not be fast enough to compensate the missing negative charges and as a consequence the material may get perforated via Coulomb explosion. Also, processes such as
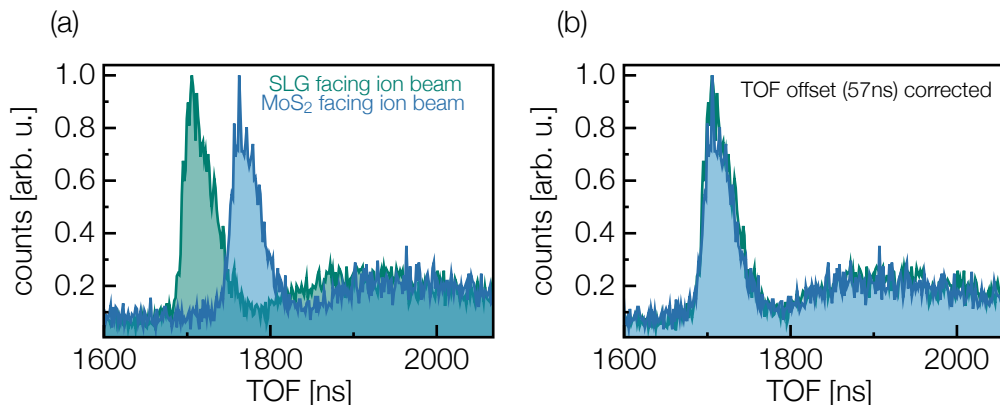
Figure 7.6: Comparison of TOF spectra for $166\,keV$ Xe^{38+} transmission through a SLG-MoS_2 heterostructure recorded for ions facing first the SLG layer (green) and those traversing first through MoS_2 (blue). The inconsistency in the flight times follows from an extension in the travel distance as a result of sample rotation.

desorption induced by electronic transitions (DIET), electron stimulated desorption (ESD) [166] and defect mediated sputtering (DS) [167] as a consequence of slow HCI irradiation can so far not be excluded as the responsible origin for the removed target atoms. Especially for insulators it was shown that perturbations in the electronic structure can survive long enough and the excitation energy is converted into kinetic energies of desorbed target atoms and ions. In contrast, for metal surfaces such strong electronic excitations can rapidly accommodate and the released energy is dissipated within the target leaving the surface undamaged [167]. As SLG can be compared to a metal surface, also no pores were observed after HCI irradiation. In the Coulomb explosion model the high carrier mobility in graphene was assigned as the reason for rapid charge resupply in the semi-metal [40]. Hence, graphene withstands HCI irradiation. Our observations on the stacked arrangement of monolayers of these two materials fit into this simple picture and will be presented in the following.

High-resolution STEM images indicate perforation of the MoS_2-SLG heterostructure (surrounded by contaminations as no cleaning procedure was applied) induced by irradiation with $166\,keV$ Xe^{38+} ions. Further magnification of the image in figure 7.7 reveals that nanometer-sized pores are only observed in the MoS_2 layer of the stack while the graphene layer beneath stays intact, as visible inside the MoS_2 pore.

As this particular sample was used for charge exchange measurements discussed in the previous chapter, the heterostructure was exposed to the ion beam from both sides. Although charge exchange dynamics seems to be independent from the order of the 2D layers, energy
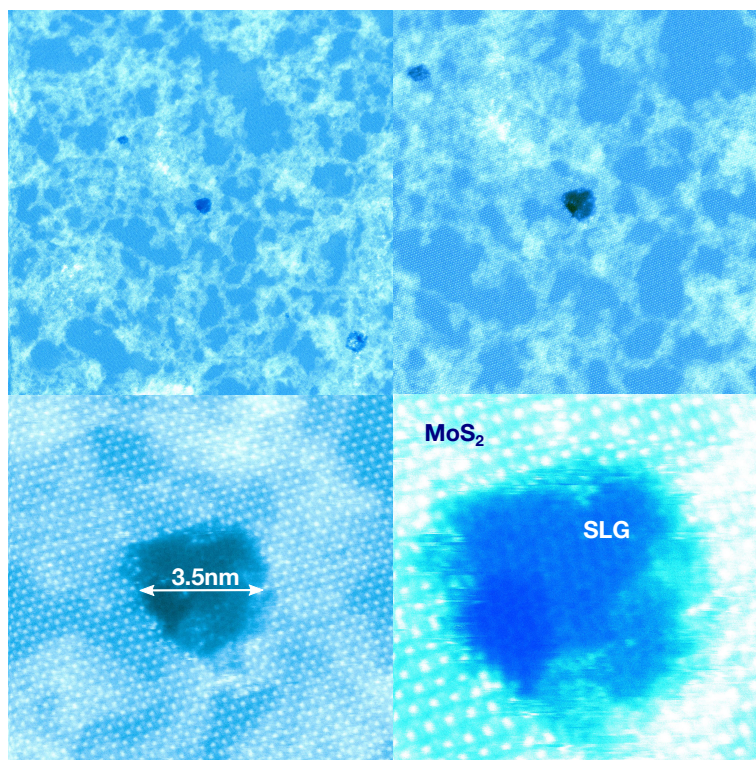
Figure 7.7: Irradiation with $166\,keV$ Xe^{38+} ions, reveals ion-induced pores in the nanometer range in the MoS_2 monolayer, while the graphene underneath the pore stays intact.

deposition might by sensitive to the materials sequence. Corresponding results might also serve as a further indicator for the depth of potential energy release. Hence, additional measurements on two identical samples were performed under the same experimental conditions. For the first stack, MoS_2 was positioned as the first layer to face the ion beam, while for the second sample the layer sequence was reversed.

In figure 7.8, once more, pores having diameters in the nanometer range follow in the MoS_2 layer as a consequence of exposing this side of the sample to the ion beam. A closer look, again, reveals the still intact graphene beneath the pore.

However, when reversing the order of the layers before exposing the sample to the ion beam, large field of view TEM images after ion irradiation show no ion-induced damages neither in the graphene nor in the MoS_2 (figure 7.9). Nanometer sized spots darker in contrast (upper left) turn out to be still intact MoS_2 after sequentially filtering the image for contaminations (upper middle) and SLG (lower left) via a FFT. Diffraction pattern of the electron beam in the TEM further
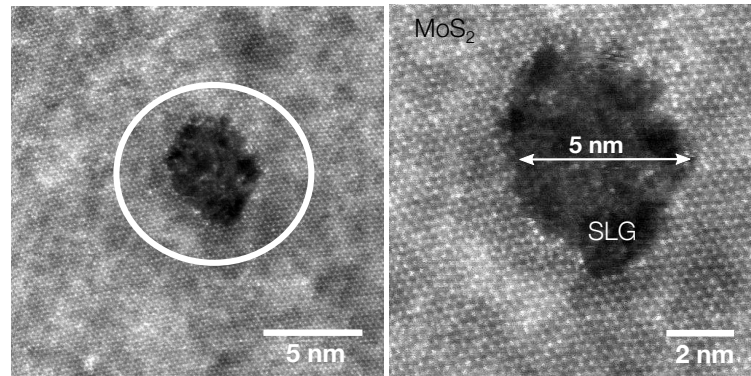
Figure 7.8: MoS$_2$ layer facing the 166 keV Xe^{38+} ion beam. Nanometer-sized pores are observed in the 2D semiconductor, while the SLG beneath stays intact.
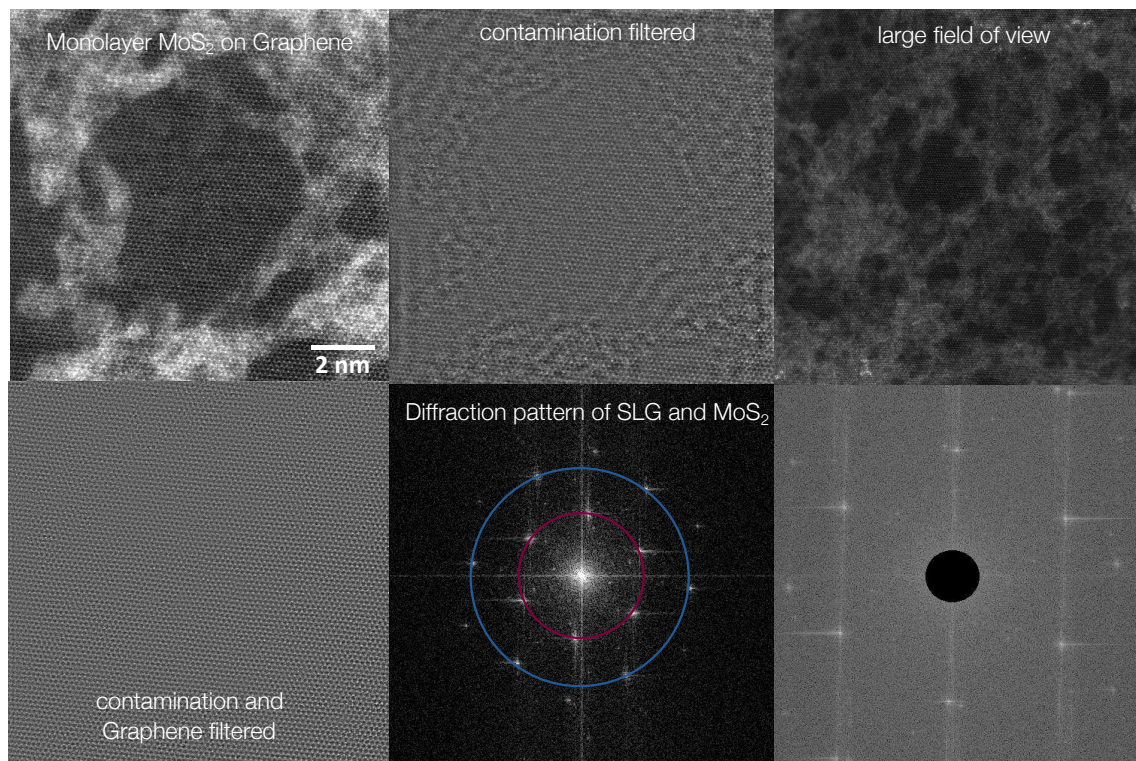
Figure 7.9: SLG protects the MoS$_2$ monolayer from perforation through the ion beam (166 keV Xe^{38+}). Spots darker in contrast (upper left) show still intact MoS$_2$ after fast Fourier transform (FFT)-filtering the image of contaminations (upper middle) and SLG (lower left). Diffraction pattern show also for a large field of view (upper right) the presence of both 2D crystals (blue and red circle show SLG and MoS$_2$ structure, respectively).

indicate the presence of both 2D crystals for the chosen spot (upper left) and a larger field of view (upper right).

7.3   Discussion

As it was concluded before that neutralization dynamics of a HCI passing a thin membrane is material independent but rather a function of layer thickness, the observed charge exchange in a van-der-Waals heterostructure is not surprising. Above the surface electrons are captured into highly excited Rydberg states while the consequent deexcitation proceeds via ICD in the vicinity of the first layer for which the precise sequence of the stacking becomes irrelevant. However, the further stabilization of electrons in the projectile very well depends on the interaction time, i.e. the thickness of the layered stack. As this is the same for a MoS_2-SLG and a SLG-MoS_2 configuration, also the received exit charge states are virtually the same. This further suggests that the majority of potential energy is deposited at the surface and within the first layer of a material via charge exchange processes. The assumption is further supported by the observation of ion-induced pores once the heterostructure is exposed to slow HCIs with the MoS_2 layer facing the ion beam. The layer gets polarized and since charge transport in between the MoS_2 and SLG layers is ineffective (only weak van-der-Waals-like forces prevail), Coulomb repulsion may lead to the perforation of the MoS_2 monolayer within the Coulomb explosion model. Ion-induced electronic excitations may also survive long enough in the band gap material and the excitation energy may be transferred onto target atoms leading to desorbtion or sputtering. However, once the stack is reversed and the ion first impacts at the SLG, the removed charges are promptly resupplied due to the high electron mobility in graphene and prevent Coulomb explosion. Further, the released energy is dissipated rapidly and the semimetal remains without any structural surface modifications. The initially highly charged projectile deposits the majority of its potential energy into the graphene sheet and hence, the following MoS_2 sheet remains undamaged.

A further indication for the high sensitivity to the first and topmost surface layer achievable by the irradiation with slow HCIs, is shown in figure 7.10. Here, initially two layers of MoS_2 on top of SLG were present before ion irradiation. Such regimes exist in the sample as a consequence of the CVD growing process. A trade-off in the growing time between overall coverage and layer thickness homogeneity always has to be made using this method. The potential energy deposition of 166 kev Xe^{38+} leads to pore formation in the first layer of MoS_2 while the second layer (together with the graphene on top) stays undamaged. Hence, the initially HCI deposits the majority of its potential energy already within the first layer and as a consequence the remaining energy is not sufficient enough to create a second pore.

Our study on ion-induced pore formation in van-der-Waals heterostructures can so far be considered only as a proof of principle. Further detailed statistics on the pore diameters depending

Figure 7.10: Regimes of present bilayer MoS_2 on top of SLG as a result of CVD growth. Ion-induced pores by irradiation with $166\,keV$ Xe^{38+} ions only in the first layer of MoS_2. The second layer as well as SLG beneath the pore stay intact.

on the irradiation parameters will follow in the future. Tuneable pore sizes are in fact conceivable by choosing a certain combination of kinetic and potential energy, i.e. via the ion's charge state, as this was already shown for CNMs [7, 36] and freestanding monolayer MoS_2 [153]. Perforation of only one layer in a stack of 2D crystals might be applicable in future for fabrication of devices based on 2D materials. Currently, a major challenge lies in the fabrication of interlayer contacts between the membranes. Nowadays, this is accomplished by reactive plasma etching. The edges are removed until the desired inner layer becomes accessible and is contacted by metal evaporation [30]. Ion-induced pores could form a more reliable alternative to this less precise process. The holes in one membrane can be filled with a substitute, e.g. Au via metal evaporation, and an additional 2D layer could be grown or deposited on top. In this way besides the weak van-der-Waals-like forces inbetween the layers, additional electric contacts would allow charge transfer at specific spots between two 2D materials. Also, the perforation of only the top layer in a van-der-Waals heterostructure might be applicable for 2D masks in nano-lithography. The pore-diameter can be chosen on a nanometer scale and well-defined simply by selecting the required charge state with a Wien filter. After creating the mask by HCI irradiation, the desired material, e.g. via metal evaporation, can be introduced into the experimental chamber. When the deposition process is finished, the perforated 2D mask can be removed, as it was recently accomplished by disassembling a van-der-Waals heterostructure layer-by-layer [168]. Thus, a 2D layer coated with the desired pattern remains. Such a technique may not be limited to the special SLG-MoS_2 heterostructure combination but could also be accomplished for using other TMDs for example. Such a possible method is sketched in figure 7.11. In contrast to lithography using focused ion beams, the big advantage of this method is its high surface sensitivity. While the pattern is introduced in a monolayer, the layers beneath remain undamaged.
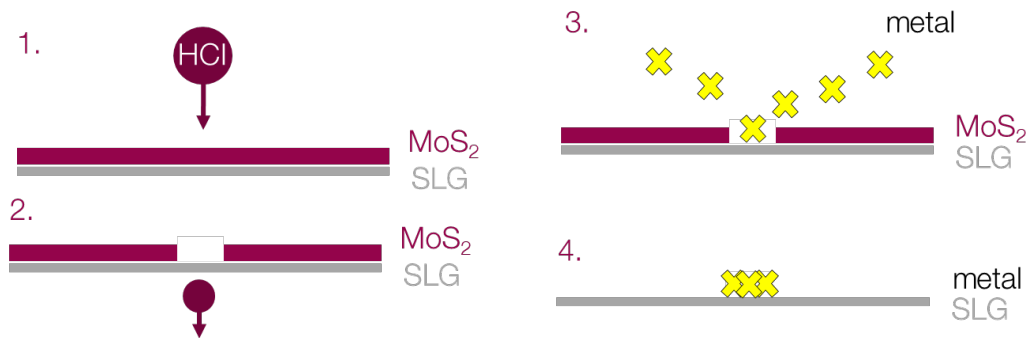
Figure 7.11: Nano-lithography by perforating a 2D layer with HCIs. Once pores are created the desired coating material, e.g. via metal evaporation, can be introduced into the experimental chamber and after successful deposition the 2D mask can be removed again.

8

Summary and Conclusion

The present thesis deals with the fundamental understanding of charge exchange and neutralization dynamics of HCIs in the vicinity of a surface. For these investigations 2D materials were used as these ideal targets offering thicknesses on the atomic scale. Hence, charge transport, energy release and energy deposition can be studied without interference of additional multiplication processes. Additionally, the response of such thin solids to the intrusion of a strong and localized electrical field created by an approaching slow HCI was tested. While a common material independent charge exchange mechanism can be concluded, the ion-induced damage to the material is crucially depending on its electronic properties.

Ion transmission through various freestanding 2D membranes having different electronic properties was performed using slow projectiles in high charge states. The first part of this thesis describes the setup of a multi-coincidence measurement apparatus which allows to record and analyze ions after their transmission and the number of emitted electrons due to the interaction at the same time. Ions can be analyzed in terms of their exit charge state, their scattering angle as well as their energy loss. In coincidence, number and energy distributions of emitted electrons as a consequence of energy release are recorded and can be assigned to projectiles in a certain exit charge state.

The interaction of highly charged Xenon ions with semimetallic graphene leads to surprisingly fast charge exchange as this was reported earlier [40]. Additional removal of contaminations and residuals from the growing process from the samples was achieved by heat and laser treatment within these studies. The ion's neutralization dynamics also for cleaned SLG samples remains to proceed on a femtosecond time scale. ICD can describe the observed rapid deexcitation of a HA via energy transfer through virtual photons to neighboring atoms [41].

Large amounts of potential energy are deposited when observing projectiles which exit in low charge states after their transmission through SLG. In case of a semimetallic 2D-membrane SLG no energy is invested in pore formation as we observe an undamaged monolayer in high-resolution TEM images after ion irradiation. However, the numbers of emitted electrons reaches values of up to e.g. $115e^-$ for a 87 keV Xe^{40+} ion. The majority of such electrons have energies well below 20 eV which is a further indication for ICD as an energy release channel for HAs as this high number of electrons is ejected quasi simultaneously.

Additionally performed slow HCI irradiation of two and three layers of graphene showed, that this high number of emitted electrons does not significantly change with the number of graphene layers. Hence, the majority of potential energy is deposited into a very shallow area around the surface impact point. The number of electrons captured and stabilized by the transmitted projectile increases with the number of graphene layers, but once the enhancement in the interaction time due to the increase in the target thickness is taken into account, the HA deexcitation can still be described via ICD.

Ion transmission studies through freestanding semiconducting MoS_2 show a bimodal exit charge state distribution which can be retraced to structural rather than electronic differences in MoS_2 compared to graphene. The former offers two distinct impact parameter regimes caused by the larger hexagons in the structure. For small impact parameters this leads to energy release via ICD as in SLG, while for large impact parameters the COB dynamics transiently leads to electron capture in highly excited Rydberg states. On the way to the detector a few electrons will be stabilized while the majority will be emitted due to AI processes.

The number of larger pores will however increase under HCI irradiation of the membrane. Strong electronic excitations caused by potential energy deposition of the HCI leads to the partly disintegration of the membrane [153]. Since carrier mobilities in MoS_2 are reduced by a factor of > 50 in contrast to SLG, charge removed due to the HA formation cannot be resupplied fast enough. As a result local charge-ups will lead to the rupture of the membrane. Hence, electrons excited through HA decay via ICD are hindered from leaving the potentially charged surface which results in a reduced number of actually emitted electrons as shown in this study.

Pores in a 2D membrane with tunable diameteres in the nanometer and sub-nanometer range are nowadays highly interesting for applications such as nano-sieves for water desalination [169, 170] or membranes used for DNA sequencing [171, 172]. Since by choosing a certain ion charge state and kinetic energy the pore size can be tuned, HCI irradiation represents an ideal tool for the required modification of such materials. To further investigate the surface-sensitivity of potential energy deposition, a van-der-Waals heterostructure consisting of a single layer of MoS_2 on top of SLG was irradiated with highly charged Xenon ions. Pores in MoS_2 were only observed for samples in which the ion beam first impacts the MoS_2 but not for the reversed stacking order (SLG on top). Hence, the potential energy required for visible perforation was in the latter already released within the topmost (graphene) layer. As a consequence MoS_2 remains undamaged underneath.

From the comparison of semimetallic and semiconducting 2D materials, we can conclude that neutralization dynamics of slow HCIs do only to a minor extend depend on the electronic band structure of the probed material. The deposition of potential energy proceeds very similar in SLG and MoS_2 if a common two-center Auger type HA deexcitation, i.e. ICD, is assumed. This assumption could also hold for a broad variety of other metals, semiconductors and even insulators and should definitely be investigated in the future.

However, the response to ion-induced electronic excitation crucially depends on carrier dynamics within the material and therefore its electronic properties and band structure. Structural changes in the membrane start to set in once the ion is long gone as a response of charge removal. How severe the damages are or whether the material repairs its atomic bonds fast enough very much depends on its electronic band structure.

Bibliography

[1] Mayer J.W., 'Ion implantation in semiconductors', in *1973 International Electron Devices Meeting*, 3–5 (1973)

[2] Perrière J., 'Rutherford backscattering spectrometry', *Vacuum*, **37**, 429 (1987), URL http://www.sciencedirect.com/science/article/pii/0042207X87903277

[3] Baglin J.E.E., 'Ion beam nanoscale fabrication and lithography—A review', *Applied Surface Science*, **258**, 4103 (2012), URL http://www.sciencedirect.com/science/article/pii/S0169433211018320

[4] El-Said A.S., Meissl W., Simon M.C., López-Urrutia J.R.C., Gebeshuber I.C., Lang M., Winter H.P., Ullrich J. and Aumayr F., 'Surface nanostructures induced by slow highly charged ions on CaF2 single crystals', *Nuclear Instruments and Methods in Physics Research Section B: Beam Interactions with Materials and Atoms*, **256**, 346 (2007), URL http://www.sciencedirect.com/science/article/pii/S0168583X0601264X

[5] Pomeroy J.M., Perrella A.C., Grube H. and Gillaspy J.D., 'Gold nanostructures created by highly charged ions', *Phys. Rev. B*, **75**, 241409 (2007), URL https://link.aps.org/doi/10.1103/PhysRevB.75.241409

[6] Ritter R., Kowarik G., Meissl W., El-Said A.S., Maunoury L., Lebius H., Dufour C., Toulemonde M. and Aumayr F., 'Nanostructure formation due to impact of highly charged ions on mica', *Vacuum*, **84**, 1062 (2010), URL http://www.sciencedirect.com/science/article/pii/S0042207X09004783

[7] Ritter R., Wilhelm R.A., Stöger-Pollach M., Heller R., Mücklich A., Werner U., Vieker H., Beyer A., Facsko S., Gölzhäuser A. and Aumayr F., 'Fabrication of nanopores in 1 nm

thick carbon nanomembranes with slow highly charged ions', *Applied Physics Letters*, **102**, 63112 (2013), URL `https://doi.org/10.1063/1.4792511`

[8] Wilhelm R.A., El-said A.S., Krok F., Heller R., Gruber E., Aumayr F. and Facsko S., 'Highly charged ion induced nanostructures at surfaces by strong electronic excitations', *PROGRESS IN SURFACE SCIENCE*, **90**, 377 (2015), URL `http://dx.doi.org/10.1016/j.progsurf.2015.06.001`

[9] Folkerts L. and Morgenstern R., 'Auger Electrons Resulting from Slow H-Like Ions Neutralized near a Tungsten Surface', *Europhysics Letters ({EPL})*, **13**, 377 (1990), URL `https://doi.org/10.1209{%}2F0295-5075{%}2F13{%}2F4{%}2F015`

[10] Meyer F.W., Overbury S.H., Havener C.C., van Emmichoven P.A.Z. and Zehner D.M., 'Evidence for above-surface and subsurface neutralization during interactions of highly charged ions with a metal target', *Phys. Rev. Lett.*, **67**, 723 (1991), URL `https://link.aps.org/doi/10.1103/PhysRevLett.67.723`

[11] Das J. and Morgenstern R., 'Measurement of autoionization rates for electron emission above a metal surface', *Phys. Rev. A*, **47**, R755 (1993), URL `https://link.aps.org/doi/10.1103/PhysRevA.47.R755`

[12] Donets E.D., 'The Electron Beam Method of Production of Highly Charged Ions and Its Applications', *Physica Scripta*, **T3**, 11 (1983), URL `https://doi.org/10.1088{%}2F0031-8949{%}2F1983{%}2Ft3{%}2F003`

[13] Briand J.P., de Billy L., Charles P., Essabaa S., Briand P. and Geller R., 'Production of hollow atoms by the excitation of highly charged ions in interaction with a metallic surface', *Physical Review Letters*, **65**, 159 (1990), URL `https://doi.org/10.1103/PhysRevLett.65.159`

[14] Briand J.P., de Billy L., Charles P., Essabaa S., Briand P., Geller R., Desclaux J.P., Bliman S. and Ristori C., 'Subfemtosecond study of the hypersatellite-satellite cascade in "hollow" atoms', *Phys. Rev. A*, **43**, 565 (1991), URL `https://link.aps.org/doi/10.1103/PhysRevA.43.565`

[15] Delaunay M., Fehringer M., Geller R., Hitz D., Varga P. and Winter H., 'Electron emission from a metal surface bombarded by slow highly charged ions', *Phys. Rev. B*, **35**, 4232 (1987), URL `https://link.aps.org/doi/10.1103/PhysRevB.35.4232`

[16] Lakits G., Aumayr F. and Winter H., 'Statistics of ion‑induced electron emission from a clean metal surface', *Review of Scientific Instruments*, **60**, 3151 (1989), URL `https://doi.org/10.1063/1.1140546`

[17] Aumayr F., Kurz H., Schneider D., Briere M.A., McDonald J.W., Cunningham C.E. and Winter H.P., 'Emission of electrons from a clean gold surface induced by slow, very highly charged ions at the image charge acceleration limit', *Phys. Rev. Lett.*, **71**, 1943 (1993), URL `https://link.aps.org/doi/10.1103/PhysRevLett.71.1943`

[18] Kurz H., Aumayr F., Lemell C., Töglhofer K. and Winter H.P., 'Neutralization of slow multicharged ions at a clean gold surface: Electron-emission statistics', *Physical Review A*, **48**, 2192 (1993), URL `https://link.aps.org/doi/10.1103/PhysRevA.48.2192`

[19] Kurz H., Aumayr F., Winter H.P., Schneider D., Briere M.A. and McDonald J.W., 'Electron emission and image-charge acceleration for the impact of very highly charged ions on clean gold', *Phys. Rev. A*, **49**, 4693 (1994), URL `https://link.aps.org/doi/10.1103/PhysRevA.49.4693`

[20] Burgdörfer J., Lerner P. and Meyer F.W., 'Above-surface neutralization of highly charged ions: The classical over-the-barrier model', *Phys. Rev. A*, **44**, 5674 (1991), URL `https://link.aps.org/doi/10.1103/PhysRevA.44.5674`

[21] Arnau A., Aumayr F., Echenique P.M., Grether M., Heiland W., Limburg J., Morgenstern R., Roncin P., Schippers S., Schuch R., Stolterfoht N., Varga P., Zouros T.J. and Winter H.P., 'Interaction of slow multicharged ions with solid surfaces', *Surface Science Reports*, **27**, 113 (1997), URL `https://doi.org/10.1016/S0167-5729(97)00002-2`

[22] Herrmann R., Cocke C.L., Ullrich J., Hagmann S., Stoeckli M. and Schmidt-Boecking H., 'Charge-state equilibration length of a highly charged ion inside a carbon solid', *Phys. Rev. A*, **50**, 1435 (1994), URL `https://link.aps.org/doi/10.1103/PhysRevA.50.1435`

[23] Hattass M., Schenkel T., Hamza A.V., Barnes A.V., Newman M.W., McDonald J.W., Niedermayr T.R., Machicoane G.A. and Schneider D.H., 'Charge Equilibration Time of Slow, Highly Charged Ions in Solids', *Phys. Rev. Lett.*, **82**, 4795 (1999), URL `https://link.aps.org/doi/10.1103/PhysRevLett.82.4795`

[24] Winecki S., Cocke C.L., Fry D. and Stöckli M.P., 'Neutralization and equilibration of highly charged argon ions at grazing incidence on a graphite surface', *Phys. Rev. A*, **53**, 4228 (1996), URL `https://link.aps.org/doi/10.1103/PhysRevA.53.4228`

[25] Martin S., Brédy R., Bernard J., Désesquelles J. and Chen L., 'Very Fast Hollow-Atom Decay Processes in Xe30+-C60 Collisions', *Phys. Rev. Lett.*, **89**, 183401 (2002), URL `https://link.aps.org/doi/10.1103/PhysRevLett.89.183401`

[26] Novoselov K.S., Geim A.K., Morozov S.V., Jiang D., Zhang Y., Dubonos S.V., Grigorieva I.V. and Firsov A.A., 'Electric Field Effect in Atomically Thin Carbon Films', *Science*, **306**, 666 (2004), URL `https://science.sciencemag.org/content/306/5696/666`

[27] Gass M.H., Bangert U., Bleloch A.L., Wang P., Nair R.R. and Geim A.K., 'Free-standing graphene at atomic resolution', *Nature Nanotechnology*, **3**, 676 (2008), URL `https://doi.org/10.1038/nnano.2008.280`

[28] Oshima C. and Nagashima A., 'Ultra-thin epitaxial films of graphite and hexagonal boron nitride on solid surfaces', *Journal of Physics: Condensed Matter*, **9**, 1 (1997), URL `https://doi.org/10.1088{%}2F0953-8984{%}2F9{%}2F1{%}2F004`

[29] Dresselhaus M.S. and Dresselhaus G., 'Intercalation compounds of graphite', *Advances in Physics*, **51**, 1 (2002), URL `https://doi.org/10.1080/00018730110113644`

[30] Novoselov K.S., Mishchenko A., Carvalho A. and Castro Neto A.H., '2D materials and van der Waals heterostructures', *Science*, **353** (2016), URL `https://science.sciencemag.org/content/353/6298/aac9439`

[31] Geim A.K., 'Graphene: Status and Prospects', *Science*, **324**, 1530 (2009), URL `https://science.sciencemag.org/content/324/5934/1530`

[32] Schuler S., Schall D., Neumaier D., Dobusch L., Bethge O., Schwarz B., Krall M. and Mueller T., 'Controlled Generation of a $p-n$ Junction in a Waveguide Integrated Graphene Photodetector', *Nano Letters*, **16**, 7107 (2016)

[33] Wachter S., Polyushkin D.K., Bethge O. and Mueller T., 'A microprocessor based on a two-dimensional semiconductor', *Nature Communications*, **8**, 14948 (2017), URL `http://www.ncbi.nlm.nih.gov/pmc/articles/PMC5394242/`

[34] Madauß L., Schumacher J., Ghosh M., Ochedowski O., Meyer J., Lebius H., Etat B.B.d., Toimil-molares M.E., Trautmann C., Lammertink R.G.H., Ulbricht M. and Schleberger M., 'Fabrication of nanoporous graphene/polymer composite membranes', *Nanoscale*, **9**, 10487 (2017), URL `http://dx.doi.org/10.1039/c7nr02755a`

[35] Schleberger M. and Kotakoski J., '2D Material Science: Defect Engineering by Particle Irradiation', *Materials*, **11** (2018), URL `https://www.mdpi.com/1996-1944/11/10/1885`

[36] Wilhelm R.A., Gruber E., Ritter R., Heller R., Beyer A., Turchanin A., Klingner N., Hübner R., Stöger-Pollach M., Vieker H., Hlawacek G., Gölzhäuser A., Facsko S. and Aumayr F., 'Threshold and efficiency for perforation of 1 nm thick carbon nanomembranes with slow highly charged ions', *2D Materials*, **2**, 35009 (2015), URL `https://doi.org/10.1088{%}2F2053-1583{%}2F2{%}2F3{%}2F035009`

[37] Lake R.E., Pomeroy J.M., Grube H. and Sosolik C.E., 'Charge State Dependent Energy Deposition by Ion Impact', *Phys. Rev. Lett.*, **107**, 63202 (2011), URL `https://link.aps.org/doi/10.1103/PhysRevLett.107.063202`

[38] Wilhelm R.A., 'Wechselwirkung langsamer hochgeladener Ionen mit Ionenkristalloberflächen und ultradünnen Kohlenstoffmembrane', PhD thesis (2014)

[39] Gruber E., 'Interaction of ions with 2D and 3D materials', PhD thesis (2017)

[40] Gruber E., Wilhelm R.A., Petuya R., Smejkal V., Kozubek R., Hierzenberger A., Bayer B.C., Aldazabal I., Kazansky A.K., Libisch F., Krasheninnikov A.V., Schleberger M., Facsko S., Borisov A.G., Arnau A. and Aumayr F., 'Ultrafast electronic response of graphene to a strong localized electric field', *Nature Communications*, **7**, 13948 (2016)

[41] Wilhelm R.A., Gruber E., Schwestka J., Kozubek R., Madeira T.I., Marques J.P., Kobus J., Krasheninnikov A.V., Schleberger M. and Aumayr F., 'Interatomic Coulombic Decay: The Mechanism for Rapid Deexcitation of Hollow Atoms', *Physical Review Letters*, **119**, 103401 (2017), URL `https://link.aps.org/doi/10.1103/PhysRevLett.119.103401`

[42] Schwestka J., Melinc D., Heller R., Niggas A., Leonhartsberger L., Winter H., Facsko S., Aumayr F. and Wilhelm R.A., 'A versatile ion beam spectrometer for studies of ion interaction with 2D materials', *Review of Scientific Instruments*, **89**, 85101 (2018), URL `https://doi.org/10.1063/1.5037798`

[43] Schwestka J., Wilhelm R.A., Gruber E., Heller R., Kozubek R., Schleberger M., Facsko S. and Aumayr F., 'The role of radiative de-excitation in the neutralization process of highly charged ions interacting with a single layer of graphene', *Nuclear Instruments and Methods in Physics Research Section B: Beam Interactions with Materials*

and Atoms, **422**, 63 (2018), URL `http://www.sciencedirect.com/science/article/pii/S0168583X18301368`

[44] Schwestka J., Niggas A., Creutzburg S., Kozubek R., Heller R., Schleberger M., Wilhelm R.A. and Aumayr F., 'Charge-Exchange-Driven Low-Energy Electron Splash Induced by Heavy Ion Impact on Condensed Matter', *The Journal of Physical Chemistry Letters*, **10**, 4805 (2019), URL `https://doi.org/10.1021/acs.jpclett.9b01774`

[45] Creutzburg S., Schwestka J., Niggas A., Inani H., Tripathi M., George A., Heller R., Kozubek R., Madauß L., Facsko S., Kotakoski J., Schleberger M., Turchanin A., Grande P.L., Aumay F. and Wilhelm R.A., 'Vanishing influence of the band gap on charge exchange of slow highly charged ions in freestanding single layer MoS2', *Physical Review Letters*, **to be publ** (2020)

[46] Aumayr F. and Winter H.P., 'Inelastic interactions of slow ions and atoms with surfaces', *Nuclear Instruments and Methods in Physics Research Section B: Beam Interactions with Materials and Atoms*, **233**, 111 (2005), URL `http://www.sciencedirect.com/science/article/pii/S0168583X05003174`

[47] Ziegler J.F., Biersack J.P. and Ziegler M.D., 'SRIM-The Stopping and Range of Ions in Matter', (2008)

[48] Winter H. and Aumayr F., 'Hollow atoms', *J. Phys. B: At. Mol. Opt. Phys.*, **32**, R39 (1999), URL `https://doi.org/10.1088{%}2F0953-4075{%}2F32{%}2F7{%}2F005`

[49] Hagstrum H.D., 'Theory of Auger Ejection of Electrons from Metals by Ions', *Physical review*, **96**, 336 (1954), URL `https://link.aps.org/doi/10.1103/PhysRev.96.336`

[50] Hasselkamp D., Rothard H., Groeneveld K.O., Kemmler J., Varga P. and Winter H., *Particle Induced Electron Emission II*, Springer, Berlin, Heidelberg, vol. 129 edition (1992)

[51] Bhalla C.P., 'K-shell Auger Rates, Transition Energies, and Fluorescence Yields of Variously Ionized States of Argon', *Physical Review A*, **8**, 2877 (1973), URL `https://doi.org/10.1103/PhysRevA.8.2877`

[52] Vaeck N. and Hansen J.E., 'Auger decay of hollow nitrogen atoms', *Journal of Physics B: Atomic, Molecular and Optical Physics*, **28**, 3523 (1995), URL `https://doi.org/10.1088{%}2F0953-4075{%}2F28{%}2F16{%}2F008`

[53] Jahnke T., 'Interatomic and intermolecular Coulombic decay: the coming of age story', *Journal of Physics B: Atomic, Molecular and Optical Physics*, **48**, 82001 (2015), URL `http://stacks.iop.org/0953-4075/48/i=8/a=082001http://dx.doi.org/10.1088/0953-4075/48/8/082001`

[54] Cederbaum L.S., Zobeley J. and Tarantelli F., 'Giant Intermolecular Decay and Fragmentation of Clusters', *Phys. Rev. Lett.*, **79**, 4778 (1997), URL `https://link.aps.org/doi/10.1103/PhysRevLett.79.4778`

[55] Marburger S., Kugeler O., Hergenhahn U. and Möller T., 'Experimental Evidence for Interatomic Coulombic Decay in Ne Clusters', *Physical Review Letters*, **90**, 203401 (2003), URL `https://link.aps.org/doi/10.1103/PhysRevLett.90.203401`

[56] Öhrwall G., Tchaplyguine M., Lundwall M., Feifel R., Bergersen H., Rander T., Lindblad A., Schulz J., Peredkov S., Barth S., Marburger S., Hergenhahn U., Svensson S. and Björneholm O., 'Femtosecond Interatomic Coulombic Decay in Free Neon Clusters: Large Lifetime Differences between Surface and Bulk', *Physical Review Letters*, **93**, 173401 (2004), URL `https://link.aps.org/doi/10.1103/PhysRevLett.93.173401`

[57] Jahnke T., Czasch A., Schöffler M.S., Schössler S., Knapp A., Käsz M., Titze J., Wimmer C., Kreidi K., Grisenti R.E., Staudte A., Jagutzki O., Hergenhahn U., Schmidt-Böcking H. and Dörner R., 'Experimental Observation of Interatomic Coulombic Decay in Neon Dimers', *Physical Review Letters*, **93**, 163401 (2004), URL `https://link.aps.org/doi/10.1103/PhysRevLett.93.163401`

[58] Aziz E.F., Ottosson N., Faubel M., Hertel I.V. and Winter B., 'Interaction between liquid water and hydroxide revealed by core-hole de-excitation', *Nature*, **455**, 89 (2008), URL `https://doi.org/10.1038/nature07252`

[59] Mucke M., Braune M., Barth S., Förstel M., Lischke T., Ulrich V., Arion T., Becker U., Bradshaw A. and Hergenhahn U., 'A hitherto unrecognized source of low-energy electrons in water', *Nature Physics*, **6**, 143 (2010), URL `https://doi.org/10.1038/nphys1500`

[60] Averbukh V., Müller I.B. and Cederbaum L.S., 'Mechanism of Interatomic Coulombic Decay in Clusters', *Phys. Rev. Lett.*, **93**, 263002 (2004), URL `https://link.aps.org/doi/10.1103/PhysRevLett.93.263002`

[61] Bennett R., Votavová P., Kolorenč P., Miteva T., Sisourat N. and Buhmann S.Y., 'Virtual Photon Approximation for Three-Body Interatomic Coulombic Decay', *Physical Review Letters*, **122**, 153401 (2019), URL `https://link.aps.org/doi/10.1103/PhysRevLett.122.153401`

[62] Santra R., Zobeley J. and Cederbaum L.S., 'Electronic decay of valence holes in clusters and condensed matter', *Phys. Rev. B*, **64**, 245104 (2001), URL `https://link.aps.org/doi/10.1103/PhysRevB.64.245104`

[63] Wilhelm R.A. and Grande P.L., 'Unraveling energy loss processes of low energy heavy ions in 2D materials', *Communications Physics*, **2**, 89 (2019), URL `https://doi.org/10.1038/s42005-019-0188-7`

[64] Averbukh V. and Cederbaum L.S., 'Ab initio calculation of interatomic decay rates by a combination of the Fano ansatz, Green's-function methods, and the Stieltjes imaging technique', *Journal of Chemical Physics*, **123**, 204107 (2005)

[65] Jabbari G., Klaiman S., Chiang Y.C., Trinter F., Jahnke T. and Gokhberg K., 'Ab initio calculation of ICD widths in photoexcited HeNe', *The Journal of Chemical Physics*, **140**, 224305 (2014), URL `https://doi.org/10.1063/1.4881598`

[66] Rist J., Miteva T., Gaire B., Sann H., Trinter F., Keiling M., Gehrken N., Moradmand A., Berry B., Zohrabi M., Kunitski M., Ben-Itzhak I., Belkacem A., Weber T., Landers A.L., Schöffler M., Williams J.B., Kolorenč P., Gokhberg K., Jahnke T. and Dörner R., 'A comprehensive study of Interatomic Coulombic Decay in argon dimers: Extracting R-dependent absolute decay rates from the experiment', *Chemical Physics*, **482**, 185 (2017), URL `http://www.sciencedirect.com/science/article/pii/S030101041630581X`

[67] Sigmund P., 'Mechanisms and theory of physical sputtering by particle impact', *Nuclear Instruments and Methods in Physics Research Section B: Beam Interactions with Materials and Atoms*, **27**, 1 (1987), URL `http://www.sciencedirect.com/science/article/pii/0168583X87900048`

[68] Vana M., Aumayr F., Lemell C. and Winter H.P., 'Ion-induced electron emission from solid surfaces: information content of the electron number statistics', *International Journal of Mass Spectrometry and Ion Processes*, **149-150**, 45 (1995), URL `http://www.sciencedirect.com/science/article/pii/0168117695042319`

[69] Neidhart T., Pichler F., Aumayr F., Winter H.P., Schmid M. and Varga P., 'Secondary ion emission from lithium fluoride under impact of slow multicharged ions', *Nuclear Instruments and Methods in Physics Research Section B: Beam Interactions with Materials and Atoms*, **98**, 465 (1995), URL `http://www.sciencedirect.com/science/article/pii/0168583X95001697`

[70] Lemell C., Stöckl J., Burgdörfer J., Betz G., Winter H.P. and Aumayr F., 'Multicharged Ion Impact on Clean Au(111): Suppression of Kinetic Electron Emission in Glancing Angle Scattering', *Phys. Rev. Lett.*, **81**, 1965 (1998), URL `https://link.aps.org/doi/10.1103/PhysRevLett.81.1965`

[71] Meissl W., Simon M.C., Crespo López-Urrutia J.R., Tawara H., Ullrich J., Winter H. and Aumayr F., 'Highly charged ion-induced potential electron emission from clean Au(1 1 1): Dependence on the projectile angle of incidence', *Nuclear Instruments and Methods in Physics Research, Section B: Beam Interactions with Materials and Atoms*, **256**, 520 (2007), URL `https://doi.org/10.1016/j.nimb.2006.12.102`

[72] Baragiola R.A., Alonso E.V. and Florio A.O., 'Electron emission from clean metal surfaces induced by low-energy light ions', *Phys. Rev. B*, **19**, 121 (1979), URL `https://doi.org/10.1103/PhysRevB.19.121`

[73] Vana M., Kurz H., Winter H.P. and Aumayr F., 'Potential and kinetic electron emission from clean gold induced by multicharged nitrogen ions', *Nuclear Instruments and Methods in Physics Research Section B: Beam Interactions with Materials and Atoms*, **100**, 402 (1995), URL `http://www.sciencedirect.com/science/article/pii/0168583X94008469`

[74] Eder H., Aumayr F. and Winter H., 'Search for projectile charge dependence of kinetic electron emission from clean polycrystalline gold', *Nuclear Instruments and Methods in Physics Research Section B: Beam Interactions with Materials and Atoms*, **154**, 185 (1999), URL `http://www.sciencedirect.com/science/article/pii/S0168583X99000348`

[75] Cernusca S., Fürsatz M., Winter H.P. and Aumayr F., 'Ion-induced kinetic electron emission from HOPG with different surface orientation', *EPL (Europhysics Letters)*, **70**, 768 (2005), URL `http://stacks.iop.org/0295-5075/70/i=6/a=768`

[76] Debroy S., Miriyala V.P.K., Sekhar K.V., Acharyya S.G. and Acharyya A., 'Graphene heals thy cracks', *Computational Materials Science*, **109**, 84 (2015), URL `http://www.sciencedirect.com/science/article/pii/S092702561500350X`

[77] Emmrich D., Beyer A., Nadzeyka A., Bauerdick S., Meyer J.C., Kotakoski J. and Gölzhäuser A., 'Nanopore fabrication and characterization by helium ion microscopy', *Applied Physics Letters*, **108**, 163103 (2016), URL `https://doi.org/10.1063/1.4947277`

[78] Wirtz L., Reinhold C.O., Lemell C. and Burgdörfer J., 'Liouville master equation for multi-electron dynamics: Neutralization of highly charged ions near a LiF surface', *Phys. Rev. A*, **67**, 12903 (2003), URL `https://link.aps.org/doi/10.1103/PhysRevA.67.012903`

[79] Bitensky I.S. and Parilis E.S., 'Shock wave mechanism for cluster emission and organic molecule desorption under heavy ion bombardment', *Nuclear Instruments and Methods in Physics Research Section B: Beam Interactions with Materials and Atoms*, **21**, 26 (1987), URL `http://www.sciencedirect.com/science/article/pii/0168583X87901352`

[80] Schenkel T., Hamza A.V., Barnes A.V., Schneider D.H., Banks J.C. and Doyle B.L., 'Ablation of GaAs by Intense, Ultrafast Electronic Excitation from Highly Charged Ions', *Phys. Rev. Lett.*, **81**, 2590 (1998), URL `https://link.aps.org/doi/10.1103/PhysRevLett.81.2590`

[81] Zschornack G., Kreller M., Ovsyannikov V.P., Grossman F., Kentsch U., Schmidt M., Ullmann F. and Heller R., 'Compact electron beam ion sources/traps: Review and prospects (invited)', *Review of Scientific Instruments*, **79**, 02A703 (2008), URL `https://aip.scitation.org/doi/abs/10.1063/1.2804901`

[82] Schmidt M., Peng H., Zschornack G. and Sykora S., 'A compact electron beam ion source with integrated Wien filter providing mass and charge state separated beams of highly charged ions', *Review of Scientific Instruments*, **80** (2009), URL `https://doi.org/10.1063/1.3125628`

[83] Dahl D.A., 'Simion for the personal computer in reflection', *International Journal of Mass Spectrometry*, **200**, 3 (2000), URL `http://www.sciencedirect.com/science/article/pii/S1387380600003055`

[84] Melinc D., 'Experimental Setup NIELS for Energy Loss Measurement of Slow Highly Charged Ions based on Time-of-Flight', (2017)

[85] Klingner N., Heller R., Hlawacek G., Borany J.V., Notte J., Huang J. and Facsko S., 'Ultramicroscopy Nanometer scale elemental analysis in the helium ion microscope using time of flight spectrometry', *Ultramicroscopy*, **162**, 91 (2016), URL `http://dx.doi.org/10.1016/j.ultramic.2015.12.005`

[86] Quantifoil Micro Tools GmbH, 'Quantifoil', (2019), URL `https://www.quantifoil.com`

[87] Aumayr F., Lakits G. and Winter H., 'On the measurements of statistics for particle-induced electron emission from a clean metal surface', *Applied Surface Science*, **47**, 139 (1991), URL `https://doi.org/10.1016/0169-4332(91)90028-I`

[88] Technologies M., 'Passivated implanted planar silicon (PIPS) detectors for industrial applications and physics research', (2020), URL `https://www.mirion.com`

[89] Kalvas T., Tarvainen O., Ropponen T., Steczkiewicz O., Ärje J. and Clark H., 'IBSIMU: A three-dimensional simulation software for charged particle optics', *Review of Scientific Instruments*, **81**, 02B703 (2010), URL `https://doi.org/10.1063/1.3258608`

[90] Niggas A., 'The role of contaminations in the interaction of highly charged ions with 2D materials', (2019)

[91] RoentDek Handels GmbH, 'RoentDek Handels GmbH', URL `http://www.roentdek.com`

[92] RoentDek Handels GmbH, 'CoboldPC Software', URL `http://www.roentdek.com/`

[93] Schwestka J., 'Coincidence Measurements of Electron Emission from Graphene', PhD thesis (2016)

[94] Stechauner B., 'Detection of slow electrons emitted due to slow highly chraged ion impact on graphene', PhD thesis (2019)

[95] ORTEC, 'ORTEC Models 142A, 142B, and 142C preamplifiers Operating and Service Manual', URL `https://www.ortec-online.com`

[96] Ochedowski O., Marinov K., Scheuschner N., Poloczek A., Bussmann B.K., Maultzsch J. and Schleberger M., 'Effect of contaminations and surface preparation on the work function of single layer MoS(2)', *Beilstein Journal of Nanotechnology*, **5**, 291 (2014), URL `doi:10.3762/bjnano.5.32`

[97] Algara-siller G., Lehtinen O., Turchanin A., Kaiser U., Algara-siller G., Lehtinen O., Turchanin A. and Kaiser U., 'Dry-cleaning of graphene Dry-cleaning of graphene', *Applied Physics Letters*, **104**, 153115 (2014), URL `https://doi.org/10.1063/1.4871997`

[98] Bolotin K.I., Sikes K.J., Jiang Z., Klima M., Fudenberg G., Hone J., Kim P. and Stormer H.L., 'Ultrahigh electron mobility in suspended graphene', *Solid State Communications*, **146**, 351 (2008), URL `http://www.sciencedirect.com/science/article/pii/S0038109808001178`

[99] Li Z., Wang Y., Kozbial A., Shenoy G., Zhou F., McGinley R., Ireland P., Morganstein B., Kunkel A., Surwade S.P., Li L. and Liu H., 'Effect of airborne contaminants on the wettability of supported graphene and graphite', *Nature Materials*, **12**, 925 (2013), URL `https://doi.org/10.1038/nmat3709`

[100] Dan Y., Lu Y., Kybert N.J., Luo Z. and Johnson A.T.C., 'Intrinsic Response of Graphene Vapor Sensors', *Nano Letters*, **9**, 1472 (2009), URL `https://doi.org/10.1021/nl8033637`

[101] Geim A.K. and Grigorieva I.V., 'Van der Waals heterostructures', *Nature*, **499**, 419 (2013), URL `https://doi.org/10.1038/nature12385`

[102] Lupina G., Kitzmann J., Costina I., Lukosius M., Wenger C., Wolff A., Vaziri S., Östling M., Pasternak I., Krajewska A., Strupinski W., Kataria S., Gahoi A., Lemme M.C., Ruhl G., Zoth G., Luxenhofer O. and Mehr W., 'Residual Metallic Contamination of Transferred Chemical Vapor Deposited Graphene', *ACS Nano*, **9**, 4776 (2015), URL `https://doi.org/10.1021/acsnano.5b01261`

[103] Lin Y.C., Lu C.C., Yeh C.H., Jin C., Suenaga K. and Chiu P.W., 'Graphene Annealing: How Clean Can It Be?' *Nano Letters*, **12**, 414 (2012), URL `https://doi.org/10.1021/nl203733r`

[104] Kozubek R., 'Analyse von Defektstrukturen in zweidimensionalen Materialien nach der Interaktion mit hochgeladenen Ionen', PhD thesis (2018)

[105] Kretinin A.V., Cao Y., Tu J.S., Yu G.L., Jalil R., Novoselov K.S., Haigh S.J., Gholinia A., Mishchenko A., Lozada M., Georgiou T., Woods C.R., Withers F., Blake P., Eda G., Wirsig A., Hucho C., Watanabe K., Taniguchi T., Geim A.K. and Gorbachev R.V., 'Electronic properties of graphene encapsulated with different two-dimensional atomic crystals', *Nano Letters*, **14**, 3270 (2014), URL `https://doi.org/10.1021/nl5006542`

[106] GmbH L., 'Lasertack - New Laser Generation', (2019), URL `https://www.lasertack.com/6w-445nm-laserdiodenmodul-nubm44,`

[107] Wilhelm R.A., *Ion-Solid Interaction* (2018)

[108] Wöckinger B., 'Scattering of Highly Charged Ions on Single- , Double- and Triple layer Graphene', (2019)

[109] Winter H.P., Vana M., Lemell C. and Aumayr F., 'Interaction of slow multicharged ions with solid surfaces: current concepts and new information on slow electron emission', *Nuclear Instruments and Methods in Physics Research Section B: Beam Interactions with Materials and Atoms*, **115**, 224 (1996), URL `http://www.sciencedirect.com/science/article/pii/0168583X95015043`

[110] Mertens A., Maass K., Lederer S., Winter H., Eder H., Stöckl J., Winter H.P., Aumayr F., Viefhaus J. and Becker U., 'Studies on electron emission during grazing impact of keV-hydrogen atoms on a LiF(001) surface via translational spectroscopy', *Nuclear Instruments and Methods in Physics Research Section B: Beam Interactions with Materials and Atoms*, **182**, 23 (2001), URL `http://www.sciencedirect.com/science/article/pii/S0168583X01006504`

[111] Bodewits E., Hoekstra R., Kowarik G., Dobes K. and Aumayr F., 'Highly-charged-ion-induced electron emission from C$\{\}_{60}$ thin films', *Phys. Rev. A*, **84**, 42901 (2011), URL `https://link.aps.org/doi/10.1103/PhysRevA.84.042901`

[112] Bodewits E., Hoekstra R., Dobes K. and Aumayr F., 'Electron-emission processes in highly charged Ar and Xe ions impinging on highly ordered pyrolytic graphite at energies just above the kinetic threshold', *Phys. Rev. A*, **90**, 52703 (2014), URL `https://link.aps.org/doi/10.1103/PhysRevA.90.052703`

[113] Hagstrum H.D., 'Auger Ejection of Electrons from Tungsten by Noble Gas Ions', *Phys. Rev.*, **96**, 325 (1954), URL `https://link.aps.org/doi/10.1103/PhysRev.96.325`

[114] Bay H.L., Andersen H.H., Hofer W.O. and Nielsen O., 'Transmission sputtering yields of gold at 6.8 MeV', *Applied physics*, **11**, 289 (1976), URL `https://doi.org/10.1007/BF00897068`

[115] Drescher H., Reimer L. and Seidel H., 'Backscattering and secondary electron emission of 10-100 keV electrons in scanning electron microscopy', *Z. angew. Phys.*, **29** (1970)

[116] Kulenkampff H. and Spyra W., 'Energieverteilung rückdiffundierter Elektronen', *Zeitschrift für Physik*, **137**, 416 (1954), URL `https://doi.org/10.1007/BF01333457`

[117] Castro Neto A.H., Guinea F., Peres N.M.R., Novoselov K.S. and Geim A.K., 'The electronic properties of graphene', *Rev. Mod. Phys.*, **81**, 109 (2009), URL `https://link.aps.org/doi/10.1103/RevModPhys.81.109`

[118] Balandin A.A., Ghosh S., Bao W., Calizo I., Teweldebrhan D., Miao F. and Lau C.N., 'Superior Thermal Conductivity of Single-Layer Graphene', *Nano Letters*, **8**, 902 (2008), URL `https://doi.org/10.1021/nl0731872`

[119] Lee C., Wei X., Kysar J.W. and Hone J., 'Measurement of the Elastic Properties and Intrinsic Strength of Monolayer Graphene', *Science*, **321**, 385 (2008), URL `https://science.sciencemag.org/content/321/5887/385`

[120] Booth T.J., Blake P., Nair R.R., Jiang D., Hill E.W., Bangert U., Bleloch A., Gass M., Novoselov K.S., Katsnelson M.I. and Geim A.K., 'Macroscopic Graphene Membranes and Their Extraordinary Stiffness', *Nano Letters*, **8**, 2442 (2008), URL `https://doi.org/10.1021/nl801412y`

[121] Hernandez Y., Nicolosi V., Lotya M., Blighe F.M., Sun Z., De S., McGovern I.T., Holland B., Byrne M., Gun'Ko Y.K., Boland J.J., Niraj P., Duesberg G., Krishnamurthy S., Goodhue R., Hutchison J., Scardaci V., Ferrari A.C. and Coleman J.N., 'High-yield production of graphene by liquid-phase exfoliation of graphite', *Nature Nanotechnology*, **3**, 563 (2008), URL `https://doi.org/10.1038/nnano.2008.215`

[122] Zhao P., Kumamoto A., Kim S., Chen X., Hou B., Chiashi S., Einarsson E., Ikuhara Y. and Maruyama S., 'Self-Limiting Chemical Vapor Deposition Growth of Monolayer Graphene from Ethanol', *The Journal of Physical Chemistry C*, **117**, 10755 (2013), URL `https://doi.org/10.1021/jp400996s`

[123] Suk J.W., Kitt A., Magnuson C.W., Hao Y., Ahmed S., An J., Swan A.K., Goldberg B.B. and Ruoff R.S., 'Transfer of CVD-Grown Monolayer Graphene onto Arbitrary Substrates', *ACS Nano*, **5**, 6916 (2011), URL `https://doi.org/10.1021/nn201207c`

[124] Li X., Zhu Y., Cai W., Borysiak M., Han B., Chen D., Piner R.D., Colombo L. and Ruoff R.S., 'Transfer of Large-Area Graphene Films for High-Performance Transparent Conductive Electrodes', *Nano Letters*, **9**, 4359 (2009), URL `https://doi.org/10.1021/nl902623y`

[125] Graphenea, 'Graphenea', (2020), URL `https://www.graphenea.com`

[126] Ćosić M., Petrović S. and Nešković N., 'The forward rainbow scattering of low energy protons by a graphene sheet', *Nuclear Instruments and Methods in Physics Research Section B: Beam Interactions with Materials and Atoms*, **422**, 54 (2018), URL `http://www.sciencedirect.com/science/article/pii/S0168583X18301563`

[127] Bohr N., 'The penetration of atomic particles through matter', *Medd. Dan. Vid. Selsk.*, **18**, 1 (1948)

[128] Schenkel T., Barnes A.V., Niedermayr T.R., Hattass M., Newman M.W., Machicoane G.A., McDonald J.W., Hamza A.V. and Schneider D.H., 'Deposition of Potential Energy in Solids by Slow, Highly Charged Ions', *Phys. Rev. Lett.*, **83**, 4273 (1999), URL `https://link.aps.org/doi/10.1103/PhysRevLett.83.4273`

[129] Mirakhmedov M.N., 'Auger and X-ray spectra formed at highly charged ion neutralization near the metal surface', *Nuclear Inst. and Methods in Physics Research B*, **98**, 429 (1995)

[130] Zhao Y., Xiao G., Zhang X., Yang Z., Zhang Y., Zhan W., Chen X. and Li F., 'X-ray emission of hollow atoms formed by highly charged argon and xenon ions below a beryllium surface', *Nuclear Instruments and Methods in Physics Research Section B: Beam Interactions with Materials and Atoms*, **258**, 121 (2007), URL `http://www.sciencedirect.com/science/article/pii/S0168583X06013498`

[131] Jabłoński Ł., Banaś D., Braziewicz J., Czub J., Jagodziński P., Kubala-Kukuś A., Sobota D., Stabrawa I. and Pajek M., 'X-ray emission in interaction of highly charged xenon ions with Be foil', *Journal of Physics: Conference Series*, **810**, 12050 (2017), URL `https://doi.org/10.1088/1742-6596/810/1/012050`

[132] Jabłoński Ł., Banaś D., Jagodziński P., Kubala-Kukuś A., Sobota D., Stabrawa I., Szary K., Pajek and M, 'Observation of Two-Electron One-Photon X-ray transitions in collisions of slow Xe26+ ions with beryllium surface', in *Book of Abstracts, 31st International Conference on Photonic, Electronic and Atomic Collisions (ICPEAC-2019), 23. – 30. 07 2019, Deauville France*, 237 (2019)

[133] Lucchese M.M., Stavale F., Ferreira E.H.M., Vilani C., Moutinho M.V.O., Capaz R.B., Achete C.A. and Jorio A., 'Quantifying ion-induced defects and Raman relaxation length in graphene', *Carbon*, **48**, 1592 (2010), URL `http://www.sciencedirect.com/science/article/pii/S0008622310000138`

[134] Hasselkamp D. and Scharmann A., 'Ion-induced electron emission from carbon', *Physica Status Solidi A, Applied Research*, **79**, K197 (1983), URL `http://inis.iaea.org/search/search.aspx?orig{_}q=RN:15026138`

[135] Patino M.I. and Wirz R.E., 'Electron emission from carbon velvet due to incident xenon ions', *Applied Physics Letters*, **113**, 41603 (2018), URL `https://doi.org/10.1063/1.5037200`

[136] Cernusca S., 'Electron Emission and Nanodefects Due to Slow Ion Impact on Solid Surfaces.' PhD thesis (2003)

[137] Dennison J., Thomson C., Kite J., Zavyalov V. and Corbridge J., 'Materials characterization at Utah State University: Facilities and knowledge-base of electronic properties of materials applicable to spacecraft charging', in *th Spacecraft Charging Technology Conference, Huntsville, AL* (2003)

[138] Desclaux J.P., 'A multiconfiguration relativistic DIRAC-FOCK program', *Computer Physics Communications*, **9**, 31 (1975), URL `http://www.sciencedirect.com/science/article/pii/0010465575900545`

[139] Indelicato P. and Desclaux J.P., 'Multiconfiguration Dirac-Fock calculations of transition energies with QED corrections in three-electron ions', *Phys. Rev. A*, **42**, 5139 (1990), URL `https://link.aps.org/doi/10.1103/PhysRevA.42.5139`

[140] Cowan R.D., *The Theory of Atomic Structure and Spectra*, University of California Press, Berkeley, CA (1981)

[141] Banszerus L., Schmitz M., Engels S., Dauber J., Oellers M., Haupt F., Watanabe K., Taniguchi T., Beschoten B. and Stampfer C., 'Ultrahigh-mobility graphene devices from chemical vapor deposition on reusable copper', *Science Advances*, **1** (2015), URL `https://advances.sciencemag.org/content/1/6/e1500222`

[142] Lehtinen O., Kotakoski J., Krasheninnikov A.V., Tolvanen A., Nordlund K. and Keinonen J., 'Effects of ion bombardment on a two-dimensional target: Atomistic simulations of graphene irradiation', *Phys. Rev. B*, **81**, 153401 (2010), URL `https://link.aps.org/doi/10.1103/PhysRevB.81.153401`

[143] Kost D., Facsko S., Möller W., Hellhammer R. and Stolterfoht N., 'Channels of Potential Energy Dissipation during Multiply Charged Argon-Ion Bombardment of Cop-

per', *Phys. Rev. Lett.*, **98**, 225503 (2007), URL `https://link.aps.org/doi/10.1103/PhysRevLett.98.225503`

[144] Craciun M.F., Russo S., Yamamoto M., Oostinga J.B., Morpurgo A.F. and Tarucha S., 'Trilayer graphene is a semimetal with a gate-tunable band overlap', *Nature Nanotechnology*, **4**, 383 (2009), URL `https://doi.org/10.1038/nnano.2009.89`

[145] McCann E. and Koshino M., 'The electronic properties of bilayer graphene', *Reports on Progress in Physics*, **76**, 56503 (2013), URL `https://doi.org/10.1088{%}2F0034-4885{%}2F76{%}2F5{%}2F056503`

[146] Eder H., Vana M., Aumayr F. and Winter H.P., 'Precise total electron yield measurements for impact of singly or multiply charged ions on clean solid surfaces', *Review of Scientific Instruments*, **68**, 165 (1997), URL `https://doi.org/10.1063/1.1147802`

[147] Furchi M.M., Polyushkin D.K., Pospischil A. and Mueller T., 'Mechanisms of Photoconductivity in Atomically Thin MoS2', *Nano Letters*, **14**, 6165 (2014), URL `http://dx.doi.org/10.1021/nl502339q`

[148] Radisavljevic B., Radenovic A., Brivio J., Giacometti V. and Kis A., 'Single-layer MoS2 transistors', *Nature Nanotechnology*, **6**, 147 (2011), URL `http://dx.doi.org/10.1038/nnano.2010.279http://10.0.4.14/nnano.2010.279https://www.nature.com/articles/nnano.2010.279{#}supplementary-information`

[149] Sun J., Li X., Guo W., Zhao M., Fan X., Dong Y., Xu C., Deng J. and Fu Y., 'Synthesis Methods of Two-Dimensional MoS2: A Brief Review', *Crystals*, **7** (2017), URL `https://www.mdpi.com/2073-4352/7/7/198`

[150] Wang H., Liu F., Fu W., Fang Z., Zhou W. and Liu Z., 'Two-dimensional heterostructures: fabrication{,} characterization{,} and application', *Nanoscale*, **6**, 12250 (2014), URL `http://dx.doi.org/10.1039/C4NR03435J`

[151] Wilhelm R.A., Gruber E., Ritter R., Heller R., Facsko S. and Aumayr F., 'Charge Exchange and Energy Loss of Slow Highly Charged Ions in 1 nm Thick Carbon Nanomembranes', *Physical Review Letters*, **112**, 153201 (2014), URL `10.1103/PhysRevLett.112.153201`

[152] Zhou W., Zou X., Najmaei S., Liu Z., Shi Y., Kong J., Lou J., Ajayan P.M., Yakobson B.I. and Idrobo J.C., 'Intrinsic Structural Defects in Monolayer Molybdenum Disulfide', *Nano Letters*, **13**, 2615 (2013), URL `https://doi.org/10.1021/nl4007479`

[153] Kozubek R., Tripathi M., Ghorbani-Asl M., Kretschmer S., Madauß L., Pollmann E., O'Brien M., McEvoy N., Ludacka U., Susi T., Duesberg G.S., Wilhelm R.A., Krasheninnikov A.V., Kotakoski J. and Schleberger M.Y., 'Perforating Freestanding Molybdenum Disulfide Monolayers with Highly Charged Ions', *The Journal of Physical Chemistry Letters*, **10**, 904 (2019), URL `https://doi.org/10.1021/acs.jpclett.8b03666`

[154] Haigh S.J., Gholinia A., Jalil R., Romani S., Britnell L., Elias D.C., Novoselov K.S., Ponomarenko L.A., Geim A.K. and Gorbachev R., 'Cross-sectional imaging of individual layers and buried interfaces of graphene-based heterostructures and superlattices', *Nature Materials*, **11**, 764 (2012), URL `https://doi.org/10.1038/nmat3386`

[155] Shi Y., Zhou W., Lu A.Y., Fang W., Lee Y.H., Hsu A.L., Kim S.M., Kim K.K., Yang H.Y., Li L.J., Idrobo J.C. and Kong J., 'van der Waals Epitaxy of MoS2 Layers Using Graphene As Growth Templates', *Nano Letters*, **12**, 2784 (2012), URL `https://doi.org/10.1021/nl204562j`

[156] Liu Z., Song L., Zhao S., Huang J., Ma L., Zhang J., Lou J. and Ajayan P.M., 'Direct Growth of Graphene/Hexagonal Boron Nitride Stacked Layers', *Nano Letters*, **11**, 2032 (2011), URL `https://doi.org/10.1021/nl200464j`

[157] Garcia J.M., Wurstbauer U., Levy A., Pfeiffer L.N., Pinczuk A., Plaut A.S., Wang L., Dean C.R., Buizza R., Zande A.M.V.D., Hone J., Watanabe K. and Taniguchi T., 'Graphene growth on h-BN by molecular beam epitaxy', *Solid State Communications*, **152**, 975 (2012), URL `http://www.sciencedirect.com/science/article/pii/S0038109812002013`

[158] Dean C.R., Young A.F., Meric I., Lee C., Wang L., Sorgenfrei S., Watanabe K., Taniguchi T., Kim P., Shepard K.L. and Hone J., 'Boron nitride substrates for high-quality graphene electronics', *Nature Nanotechnology*, **5**, 722 (2010), URL `https://doi.org/10.1038/nnano.2010.172`

[159] Mayorov A.S., Gorbachev R.V., Morozov S.V., Britnell L., Jalil R., Ponomarenko L.A., Blake P., Novoselov K.S., Watanabe K., Taniguchi T. and Geim A.K., 'Micrometer-Scale Ballistic Transport in Encapsulated Graphene at Room Temperature', *Nano Letters*, **11**, 2396 (2011), URL `https://doi.org/10.1021/nl200758b`

[160] Britnell L., Gorbachev R.V., Jalil R., Belle B.D., Schedin F., Mishchenko A., Georgiou T., Katsnelson M.I., Eaves L., Morozov S.V., Peres N.M.R., Leist J., Geim A.K.,

Novoselov K.S. and Ponomarenko L.A., 'Field-Effect Tunneling Transistor Based on Vertical Graphene Heterostructures', *Science*, **335**, 947 (2012), URL `https://science.sciencemag.org/content/335/6071/947`

[161] Bertolazzi S., Krasnozhon D. and Kis A., 'Nonvolatile Memory Cells Based on MoS2/Graphene Heterostructures', *ACS Nano*, **7**, 3246 (2013), URL `https://doi.org/10.1021/nn3059136`

[162] Zhang W., Wang Q., Chen Y., Wang Z. and Wee A.T.S., 'Van der Waals stacked 2D layered materials for optoelectronics', *2D Materials*, **3**, 22001 (2016), URL `https://doi.org/10.1088{%}2F2053-1583{%}2F3{%}2F2{%}2F022001`

[163] Roy K., Padmanabhan M., Goswami S., Sai T.P., Ramalingam G., Raghavan S. and Ghosh A., 'Graphene–MoS2 hybrid structures for multifunctional photoresponsive memory devices', *Nature Nanotechnology*, **8**, 826 (2013), URL `https://doi.org/10.1038/nnano.2013.206`

[164] Britnell L., Ribeiro R.M., Eckmann A., Jalil R., Belle B.D., Mishchenko A., Kim Y.J., Gorbachev R.V., Georgiou T., Morozov S.V., Grigorenko A.N., Geim A.K., Casiraghi C., Neto A.H.C. and Novoselov K.S., 'Strong Light-Matter Interactions in Heterostructures of Atomically Thin Films', *Science*, **340**, 1311 (2013), URL `https://science.sciencemag.org/content/340/6138/1311`

[165] Schwestka J., Inani H., Niggas A., Kotakoski J., Aumayr F. and Wilhelm R.A., 'Perforation of 2D heterostructures with HCl', **in prepara** (2020)

[166] Ageev V.N., 'Desorption induced by electronic transitions', *Progress in Surface Science*, **47**, 55 (1994), URL `http://www.sciencedirect.com/science/article/pii/0079681694900140`

[167] Aumayr F., Varga P. and Winter H.P., 'Potential sputtering: desorption from insulator surfaces by impact of slow multicharged ions', *International Journal of Mass Spectrometry*, **192**, 415 (1999), URL `http://www.sciencedirect.com/science/article/pii/S1387380699000755`

[168] Liu F., Wu W., Bai Y., Chae S.H., Li Q., Wang J., Hone J. and Zhu X.Y., 'Disassembling 2D van der Waals crystals into macroscopic monolayers and reassembling into artificial lattices', *Science*, **367**, 903 (2020), URL `https://science.sciencemag.org/content/367/6480/903`

[169] Koenig S.P., Wang L., Pellegrino J. and Bunch J.S., 'Selective molecular sieving through porous graphene', *Nature Nanotechnology*, **7**, 728 (2012), URL `https://doi.org/10.1038/nnano.2012.162`

[170] Kou J., Yao J., Wu L., Zhou X., Lu H., Wu F. and Fan J., 'Nanoporous two-dimensional MoS2 membranes for fast saline solution purification', *Phys. Chem. Chem. Phys.*, **18**, 22210 (2016), URL `http://dx.doi.org/10.1039/C6CP01967F`

[171] Garaj S., Hubbard W., Reina A., Kong J., Branton D. and Golovchenko J.A., 'Graphene as a subnanometre trans-electrode membrane', *Nature*, **467**, 190 (2010), URL `https://doi.org/10.1038/nature09379`

[172] Feng J., Liu K., Bulushev R.D., Khlybov S., Dumcenco D., Kis A. and Radenovic A., 'Identification of single nucleotides in MoS2 nanopores', *Nature Nanotechnology*, **10**, 1070 (2015), URL `https://doi.org/10.1038/nnano.2015.219`

Acronyms

AD Auger deexcitation

AI autoionization

AN Auger neutralization

BLG bilayer graphene

CNM carbon nanomembrane

CFD constant fraction discriminator

COB classical over-the-barrier

CVD chemical vapour deposition

DIET desorption induced by electronic transitions

DLD delay-line detector

DS defect mediated sputtering

EBIS Electron Beam Ion Source

EBIT Electron Beam Ion Trap

ESD electron stimulated desorption

EDX energy-dispersive x-ray spectroscopy

FFT fast Fourier transform

FET field effect transistor

FWHM full width at half maximum

HA hollow atom

HCI highly charged ion

hBN hexagonal boron nitride

HZDR Helmholtz-Zentrum Dresden-Rossendorf

HOPG highly oriented pyrolytic graphite

HV high voltage

ICD Interatomic Coulombic Decay

KE kinetic electron emission

MCA multichannel analyzer

MCP microchannel plate

MoS$_2$ molybdenum disulfide

NIELS Neutrals and Ion Energy Loss Spectrometer

PE potential electron emission

PIPS passivated implanted planar silicon

PMMA polymethyl methacrylate

QF Quantifoil

QRN quasi-resonant neutralization

RI resonant ionization

RN Resonant neutralization

SCA single channel analyzer

SLG single layer graphene

STEM scanning transmission electron microscopy

TAC time to amplitude converter

TDC time to digital converter

TOF time of flight

TEM transmission electron microscopy

TLG trilayer graphene

TMD Transition metal dichalcogenide

UHV ultra high vacuum

WS$_2$ tungsten disulfide

Acknowledgement

Ehrlich gestanden, ist mit das Verfassen dieses Kapitels meiner Arbeit am allerschwersten gefallen. Mit Sicherheit nicht deshalb, weil ich nicht weiß wem ich für den erfolgreichen Abschluss meiner Dissertation dankbar sein soll, aber in erster Linie daher, weil mit dem Schreiben dieses Kapitels nun auch das Ende einer wundervollen Zeit mit einhergeht. Die Atmosphäre in der AG-Aumayr, die ich für viele Jahre genießen durfte, ist sicherlich einer der Gründe, die den Abschied besonders schwer machen. Daher möchte ich zu allererst unserem Gruppenleiter und meinem Betreuer *Fritz* danken, der mit seiner offenen und warmherzigen Art ein unvergleichliches Arbeitsumfeld schafft.

Fritz, du verdienst dir wahrlich den Titel eines Doktorvaters, kümmerst du dich doch um deine Schützlinge als wären sie deine eigenen Kinder. Diese Zuwendung und Unterstützung wissenschaftlicher aber auch privater Natur hat sich trotz deiner Beförderung zum Institutsleiter und dem damit verbundenen Zuwachs an Aufgaben nicht geändert. Selbst in Momenten, in denen du gerade eigentlich viel zu viel zu tun hattest und die Tür zum Sekretariat verschlossen war, stand im Geheimen deine Bürotür für uns immer offen. Dein Geschick neue Ideen auf wissenschaftliche Fragestellungen auf Anhieb parat zu haben, dein Sinn für Ordnung, deine Leidenschaft zur Forschung und der Spaß an physikalischen Experimenten, den du dir bewahrt hast, machen dich für mich zu einem großen wissenschaftlichen aber auch persönlichen Vorbild. Dein ganz eigenes Talent für Zwischenmenschliches hat uns nicht nur die Leihgabe der EBIS-A, die Grundlage meiner Doktorarbeit, ermöglicht, sondern mir auch zahlreiche eingeladene Vorträge auf Konferenzen verschafft. Auf diese Weise „wissenschaftlich groß zu werden" ist einmalig und dafür möchte ich dir besonders danken!

Aber auch dir, lieber *Richard*, gebührt an dieser Stelle ein aufrichtiges Dankeschön! Als Kollaborator wurdest du mir auf unserer ersten gemeinsamen Tagung in San Sebastian vorgestellt, aber besser kennenlernen durfte ich dich bei meinem ersten Messaufenthalt in Dresden. Mit deinem Umzug nach Wien hast du dich in den letzten Jahren für mich von einem Kollaborator über einen geschätzten Kollegen bis hin zu einem wertvollen Betreuer entwickelt. Deine Liebe

zum Detail und das unglaubliches Wissen an Literatur, das du in deinem Kopf mit dir herum trägst, sind wahrlich beeindruckend. Ich danke dir sehr für all deine Anstrengung aus jedem Paper und jedem meiner Vorträge das beste rauszuholen. Bei dir bleibt keine meiner noch so dummen Fragen unbeantwortet. Es hat wirklich gut getan so einen Bürokollegen wie dich zu haben!

Lieber *Reinhard*, sozusagen als mein Doktorbruder hast du mit mir diesen Abschnitt gemeinsam begonnen und wie einen richtigen Bruder habe ich dich wohl auch in den letzten Jahren behandelt. Danke, dass du so gut all meine Launen ertragen hast und dabei zumindest so getan hast als würdest du mir in meinem Redewahn zuhören. Danke, dass ich all meinen Ärger bei dir abladen durfte und du mir trotzdem jedes Mal aufs neue hilfsbereit zur Seite standest.

Genau so lange wie meinen großen Doktorbruder, *Reinhard*, kenne ich nun auch schon mein kleineren Bruder, *Paul*. Deine fast schon stoische Gelassenheit mit dem Talent im richtigen Moment deine wohldurchdachte Meinung zu äußern sind eine Bereicherung für jeden Probevortrag, jeden Journalclub, jede Gruppenbesprechung und jede Kaffeepause. Gepaart mit der richtigen Portion Humor und deinem immer offenen Ohr hast du dich zu mehr als nur einem Arbeitskollegen entwickelt. Danke für den tollen Urlaub in Portugal!

Georg, auch wenn du viel deiner Zeit in Garching (oder irgendwo im Waldviertel) verbracht hast, kann man durchaus sagen, dass die AG-Aumayr von deiner Anwesenheit profitiert hat. Deine Herangehensweise an so mache Probleme mit deiner verspielten Art erwecken den Anschein, dass eine Dissertation zu bewältigen ein Kinderspiel ist. Deine Work-Life-Balance ist mir ein großes Vorbild. Danke, dass du mit deinem Humor zur so entspannten und lockeren Atmosphäre in der Gruppe beiträgst!

Lieber *Herbert*, du bist erst später in unsere Runde der Dissertanten gestoßen, aber schon bald haben wir bemerkt, dass wir von deinem unschlagbaren Wissen in elektronischen Fragestellungen profitieren werden! Danke, dass du auch für mich beim Löten meiner Schutzschaltung unser E-Labor ersetzt hast!.

Die einzige Studentin, die ich anfangs eigentlich gar nicht betreuen wollte, mich aber trotzdem dazu überreden lies, hat sich als eine der größten Bereicherungen überhaupt für die AG-Aumayr erwiesen. Liebe *Anna*, ich bin sehr stolz deine Hand bei deinen ersten Schritten in die Welt der Wissenschaft gehalten haben zu dürfen. Schon sehr bald hat sich aber heraus gestellt, dass du gar keine Hand mehr benötigst weil dir schon längst Flügel gewachsen sind. Von meiner Studentin hast du dich rasch zu einer sehr geschätzten Kollegin entwickelt und ich danke dir sehr für deine Hilfsbereitschaft in so vielen Dingen, die ich hier gar nicht alle nennen kann. Dein Hang

zum Perfektionismus zeigt sich abseits vom Erstellen so mancher Poster und Paperkorrekturen aber auch in privater Natur. Mit deiner fürsorgliche Art wachst du über die Arbeitsgruppe wie sonst niemand und mit guter Gewissheit fällt es mir dadurch auch leicht die Kaffeekassa an dich abzutreten.

Aber auch noch eine Vielzahl anderer Leute haben zu dem Klima, das in unserer Arbeitsgruppe herrscht, erheblich beigetragen. Ich möchte mich daher noch bei einer Reihe an lieben Menschen bedankten, die mir das Fertigstellen meiner Doktorarbeit möglich gemacht haben: Danke *Gabriel*, für den nötigen Support aus Wiener Neustadt; danke *Martin*, für all die lockeren Kaffeegespräche mit dir; danke *Johanna*, für deine fürsorgliche Art; danke *Waldemar*, für die nötige Crazyness, die du in die Gruppe gebracht hast; danke *Lidija*, für noch mehr Frauenpower in der AG; danke *Daniel*, für deinen oft schon düsteren Humor und danke *Christian*, für deine stets so wohl bedachten Kommentare;

Außerdem möchte ich mich auch bei all meinen Studenten, *David*, *Lukas*, *Maximilian* und *Bernd*, die ich in der Zeit als Dissertantin betreuen und daran wachsen durfte bedanken. Lieber *Benjamin*, lieber *Raphael*, auch wenn ihr jetzt nicht mehr Teil unserer Arbeitsgruppe seid möchte ich mich für die Zeit mit euch bedanke und hoffe, dass ihr für die noch kommenden Diplom- und Bachelorarbeiten euren Weg an unser Institut zurück finden werdet. Auch dir, lieber *Sascha*, möchte ich für eine tolle Zusammenarbeit und vielen wissenschaftlichen Diskussionen danken aber auch für all deinen positiven und bestärkenden Worte.

Lieber *Fabian*, bei dir möchte ich mich vor allem für die nötige Abwechslung bedanken, die in manchen Momenten so notwendig war. Ob beim gemeinsamen Drohnenfliegen durch einen der Hörsäle im Freihaus oder einem Mittagessen, ich hab die inspirierenden Gespräche mit dir, die uns in unsere ganz eigene Welt eintauchen haben lassen, immer sehr genossen.

Das Vollenden dieser Arbeit wäre aber nicht möglich gewesen, wäre da nicht auch ein wesentlicher Beitrag von lieben Menschen außerhalb des universitären Lebens gewesen. Ich bedanke mich bei all meinen Freunden, die stets für den nötigen Ausgleich gesorgt haben, den ich in so manchen schwierigen Phasen doch so dringend benötigt habe. Allem voran aber, gebührt mein größter Dank meiner Familie, auf deren scheinbar nie enden wollende Unterstützung ich zählen kann. Von euch, *Christian und Isabella*, habe ich nicht nur gelernt zielstrebig und fleißig zu sein, sondern habe auch stets ein Vorbild vor Augen, zu dem ich nach wie vor aufschauen kann. Es ist eine Leichtigkeit sich im Leben auszutoben und auszuprobieren, wenn man Eltern wie euch hat, die für die notwendige Sicherheit sorgen. Das ist durchaus keine Selbstverständlichkeit und ich bin euch dafür unendlich dankbar! Ein weiterer Strang in diesem Sicherheitsnetz bildet meine Schwester, *Jennifer*. Es gibt keine Situation, in der ich nicht zuallererst dich um einen

Ratschlag bitten kann. Ich danke dir für den Halt, den du mir gibst, die Aufmerksamkeit, die du mir schenkst und den Spaß, den wir zusammen haben. Da du nun selbst den (manchmal auch mühevollen) Weg einer Dissertation eingeschlagen hast, hoffe ich, dass auch ich ab und zu mal sowohl deine Stütze als auch die nötige Ablenkung vom Laborleben für dich sein kann.

Dear *Honza*, no one else had to go with me through so many ups and downs within my life as a PhD student. I admire your acumen, your calmness, your passion in little things and your rational approach for finding solutions. Your talent to keep your composure in every situation has so often been the greatest support of all. I am so thankful for your trust and the way you let me be myself. You are truely my rock.